

**ANALYSIS OF 1.694 GHz IONOSPHERIC SCINTILLATION AND
ITS IMPACT ON SATELLITE COMMUNICATION SYSTEM**

KHAJITPAN MAKARATAT



**A THESIS SUBMITTED IN PARTIAL FULFILLMENT OF
THE REQUIREMENT FOR THE DEGREE OF
MASTER OF ENGINEERING IN ELECTRICAL ENGINEERING
SCHOOL OF GRADUATE STUDIES
KING MONGKUT'S INSTITUTE OF TECHNOLOGY LADKRABANG
2002**

ISBN 974 – 648 – 963 - 1

เลขหม.....
เลขทะเบียน..... **40423**
วันที่, เดือน, ปี..... **12.5 ก.พ. 2546**

b.....
i.....



COPYRIGHT 2002

SCHOOL OF GRADUATE STUDIES

KING MONGKUT'S INSTITUTE OF TECHNOLOGY LADKRABANG

This material is reserved for educational use only, not allowed for commercial use.

Forbidden to modify the content, and cite the document when use.

หัวข้อวิทยานิพนธ์	การวิเคราะห์การเปลี่ยนแปลงแอมพลิจูดอย่างกะทันหันของสัญญาณความถี่ 1.694 GHz เนื่องจากชั้นไอโอโนสเฟียร์และผลกระทบต่อระบบสื่อสารดาวเทียม
นักศึกษา	นางสาวจิตพรณ มกระรัช
รหัสประจำตัว	42061169
ปริญญา	วิศวกรรมศาสตรมหาบัณฑิต
สาขาวิชา	วิศวกรรมไฟฟ้า
พ.ศ.	2545
อาจารย์ผู้ควบคุมวิทยานิพนธ์	รศ. ณรงค์ เหมกรณ์

บทคัดย่อ

วิทยานิพนธ์นี้นำเสนอการวิเคราะห์ลักษณะการเกิดการเปลี่ยนแปลงแอมพลิจูดอย่างกะทันหันเนื่องจากชั้นบรรยากาศไอโอโนสเฟียร์ของสัญญาณดาวเทียมความถี่ 1.694 GHz ซึ่งรับได้จากดาวเทียม GMS-5 แล้วนำมาวิเคราะห์เปรียบเทียบความรุนแรงของการแกว่งแอมพลิจูดสัญญาณตามเวลาและฤดูกาล และเปรียบเทียบระดับความรุนแรงการแกว่งของสัญญาณเดียวกันนี้ที่วัดได้ที่สถานีเชียงใหม่เพื่อศึกษาลักษณะการเกิดที่ตำแหน่งละติจูดต่างกัน นอกจากนี้การใช้ทฤษฎี FFT และฟังก์ชันอัตโนมัติสัมพันธ์สามารถหาความหนาแน่นกำลังเชิงสเปกตรัมและค่าเวลาร่วมนัยของการแกว่งแอมพลิจูดสัญญาณได้ซึ่งค่าทั้งสองนี้มีความสัมพันธ์กับกลุ่มความไม่สม่ำเสมอของอิเล็กตรอนในชั้นบรรยากาศ และสามารถนำไปหาอัตราการแกว่งแอมพลิจูดสัญญาณเปรียบเทียบกับอัตราการแกว่งที่หาจากวิธีอื่นๆได้ ค่าเวลาร่วมนัยนำไปคำนวณหาระยะทาง decorrelation distance สำหรับปรับปรุงระบบโดยวิธีการรับหลายแห่ง นอกจากนี้การวิเคราะห์ช่วงเวลาและจำนวนการจางหายของสัญญาณเมื่อแอมพลิจูดแกว่งต่ำกว่าระดับการจางหายต่างๆที่กำหนดสามารถนำมาคำนวณหาความน่าเชื่อถือของการสื่อสารขณะนั้นได้ ค่า PDF และ CDF ของการเปลี่ยนแปลงแอมพลิจูดสัญญาณในช่วงเวลาสั้นๆ มีความสอดคล้องกับการกระจายแบบเกาส์และนาคากามิแต่จะไม่สอดคล้องกับการเปลี่ยนแปลงสัญญาณในระยะยาว จึงต้องใช้แบบจำลองของ Moulisley-Vilar และการประมาณค่าเชิงวิเคราะห์ทำการหาลักษณะการกระจายของการแกว่งสัญญาณในระยะยาว แบบจำลองการกระจายนี้สามารถนำไปคำนวณหาผลกระทบของการเปลี่ยนแปลงแอมพลิจูดอย่างกะทันหันที่มีต่อระบบเช่น ความจุช่องสัญญาณและความหนาแน่นเฉลี่ยของอัตราบิตผิดพลาดสำหรับการสื่อสารที่มีการมอดูเลตแบบ M-PSK, CPSK, NCFPSK และ DS-SS ได้

Thesis Title	Analysis of 1.694 GHz ionospheric scintillation and its impact on satellite communication system
Student	Miss Khajitpan Makaratat
Student ID	42061169
Degree	Master of Engineering
Programme	Electrical Engineering
Year	2002
Thesis Advisor	Assoc. Prof. Narong Hemmakorn

ABSTRACT

This thesis presents the ionospheric scintillation characteristics of 1.694 GHz signal from GMS-5 satellite. The diurnal and seasonal variation, and the comparison of scintillation between different latitudinal positions (KMITL and CMU) are also analyzed. Using FFT and autocorrelation function analyses can determine the power spectral density and the decorrelation time or coherent time respectively corresponding to the irregularities characteristics. Moreover, scintillation rate can be determined from these and compared with the scintillation rate obtained by the mean crossing technique. The decorrelation time is used to calculate the ground decorrelation distance for space diversity technique in order to improve the system degradation from scintillation effects. Furthermore, the distribution of fade duration and fade numbers can obtain the message reliability when signal fluctuating exceeded any specific fade levels. The PDF and CDF of the instantaneous amplitude scintillation is close to the Gaussian and Nakagami-m distribution. For long-term scintillation, these distributions do not fit well, but the scintillation models proposed by Mousley-Vilar and the analytical approximation fit well with the experimental distribution. Finally, the impacts of communication due to scintillation effects are determined by using these scintillation models, such as the channel capacity for M-PSK system, the average probability of bit error for CPSK, NCFSK and DS-SS system.

ACKNOWLEDGEMENTS

Many persons contributed their helps to the successful completion of this thesis. Without them, this thesis would never been accomplished. I would like to take this chance to express my appreciation to them.

Firstly, this research work was conducted under the supervision of Associate Professor Narong Hemmakorn, who gives me all kind and helpful suggestion and support.

I am very grateful to Associate Prof. Nipha Leelaruji for all her kindly discussion in many things. Also, I would like to sincerely appreciate to Prof. Dr. Yoshiaki Moriya of Tokai University, Prof. Dr. Matsuichi Yamada of Tokyo University of Technology, Dr. Hisamitsu Minakoshi and Dr. Takashi Maruyama of Communication Research Laboratory. Many kindly discussions and comments from them are very useful for my research. I would like to acknowledge all staffs in the Ionosphere and Radio Propagation Group, CRL for all kindly help during doing research there.

Special thanks are due to my senior and colleagues in Satellite Communication Laboratory, ReCCIT for their discussion, friendship and entertainment. Many thanks to Mr. Prasit Nakornrat, Mr. Thikumporn Boonchuk, Mr. Settakorn Kamuang and Mr. Amnarch Khawne for their consultants in any troubles. Eventually, special thank to Mr. Adit Decharat for his help, discussion and nice consultants.

I also appreciate the school of graduate studies of King Mongkut's Institute of Technology Ladkrabang for providing the scholarship of the thesis preparation support.

Finally, this thesis is dedicated to my parents and younger brother who always support and encourage for everything throughout my life.

Khajitpan Makaratat

TABLE OF CONTENTS

	Page
Thai Abstract.....	I
English Abstract.....	II
Acknowledgements.....	III
Table of Contents.....	IV
List of Tables.....	VII
List of Figures.....	VIII
Chapter 1 Introduction.....	1
1.1 Literature of Ionospheric Scintillation.....	1
1.2 The Significant of the study.....	2
1.3 The Objective and Chapters' Synopsis of the Thesis.....	3
Chapter 2 Satellite Signal Amplitude Scintillation.....	5
2.1 Ionospheric Scintillation.....	5
2.1.1 Ionospheric Irregularities.....	6
2.1.2 The Irregularities' Characteristics.....	9
2.1.3 Geometrical Consideration of the Ionospheric Scintillation.....	12
2.2 Related Factors of Ionospheric Scintillation Occurrence.....	13
2.2.1 Geomagnetic Latitude Dependence.....	14
2.2.2 Solar Activity and Sunspot Numbers Dependence.....	14
2.2.3 Diurnal and Seasonal Dependence.....	15
2.2.4 Signal Frequency and Elevation Angle Dependence.....	15
2.3 Scintillation Index.....	15
2.3.1 SI Index.....	15
2.3.2 S ₄ Index.....	16
2.3.3 Standard Deviation.....	17
2.4 Conclusion.....	17
Chapter 3 Experimental System and Morphological Results.....	18
3.1 Configuration of the Experimental System.....	18
3.2 Morphological Results.....	20

This material is reserved for educational use only, not allowed for commercial use.

Forbidden to modify the content, and cite the document when use.

TABLE OF CONTENTS (to)

	Page
3.2.1 Scintillation Intensity Analysis.....	21
3.2.2 Diurnal and Seasonal Variation.....	22
3.2.3 Scintillation Characteristics in case of Different Latitudinal Position.....	31
3.3 Conclusion.....	36
Chapter 4 Instantaneous Analysis of Frequency-Time Scintillation Structures.....	37
4.1 Power Spectrum Analysis of Scintillation Signal.....	39
4.1.1 Temporal Scintillation Analysis.....	39
4.1.2 Spectral Behavior of Scintillation.....	42
4.2 Autocorrelation Analysis of Scintillation Signal.....	50
4.3 Scintillating Frequency-Time Structure for Communications.....	56
4.3.1 Analysis of Scintillation Rate by Power Spectral Density and Autocorrelation Function.....	56
4.3.2 Ground decorrelation Distance for Space Diversity Antenna.....	60
4.4 Conclusion.....	62
Chapter 5 Amplitude Distribution and Fade Analysis of Scintillation Signal.....	63
5.1 Probability Distribution Relevant to Amplitude Fluctuation.....	63
5.2 Fade Statistic Analysis of Scintillation Signal.....	68
5.2.1 Fade Duration Distribution.....	68
5.2.2 Message Reliability of Scintillation Channel.....	75
5.3 Conclusion.....	78
Chapter 6 Channel Modeling of Scintillation and its Impact on Communication System.....	79
6.1 Scintillation Channel Modeling.....	81
6.1.1 Moulslley-Vilar Distribution.....	81
6.1.2 Analytical Approximation.....	84
6.2 Channel Capacity in Scintillation Channel.....	87

This material is reserved for educational use only, not allowed for commercial use.

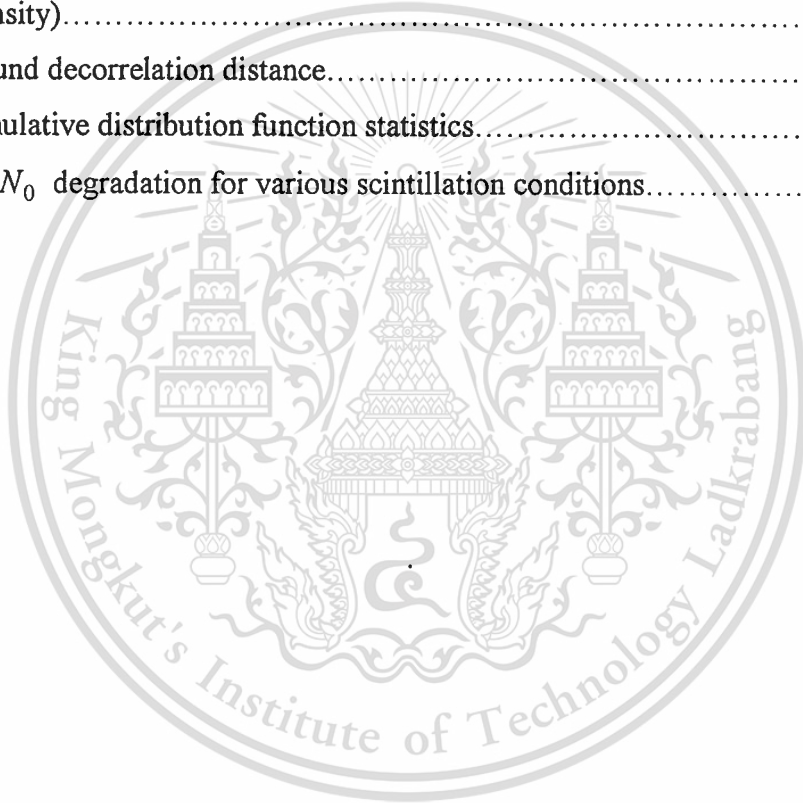
Forbidden to modify the content, and cite the document when use.

TABLE OF CONTENTS (to)

	Page
6.3 Estimation of Bit Error Probability during Scintillation.....	91
6.4 Conclusion.....	98
Chapter 7 Conclusion.....	100
7.1 Summary of the Preceding Chapters.....	100
7.2 Remark for the Future Research.....	102
Bibliography.....	103
Appendices.....	106
Appendix A Electrodynamics Characteristics and the Plasma Movement...	107
Appendix B Fresnel Zone Radius Determination.....	110
Appendix C Calculation of Slant Path below the Irregularities Height.....	112
Appendix D Binary Decision Threshold.....	113
Appendix E Probability of Bit Error for Coherently Detected Phase Shift Keying.....	116
Appendix F Probability of Bit Error for Noncoherently Detected Frequency Shift Keying.....	120
Author Biography.....	124

LIST OF TABLES

Table	Page
3.1 Satellite receiving system parameters.....	19
3.2 Maximum levels of amplitude scintillation.....	30
4.1 Parameters of scintillation power spectral density.....	40
4.2 The parameters obtained from power spectrum and autocorrelation analysis of the events (arrange in order of scintillation intensity).....	57
4.3 Calculation of scintillation fade rate (arranged in order of scintillation intensity).....	60
4.4 Ground decorrelation distance.....	61
5.1 Cumulative distribution function statistics.....	66
6.1 E_b/N_0 degradation for various scintillation conditions.....	96



LIST OF FIGURES

Fig.	Page
1.1 GMS-5 satellite images observed on March 30, 2000	
(a) clear air condition.....	2
(b) scintillation condition.....	2
2.1 Three dimensional of the irregularities structure.....	6
2.2 Simplified representation of the ionospheric irregularities.....	7
2.3 Vector representation of amplitude and phase scintillation.....	12
2.4 Geometry of the ionospheric irregularities that effect radiowave signal.....	13
2.5 Scintillation intensity during solar maximum and minimum years.....	14
3.1 Block diagram of ionospheric scintillation observation system.....	19
3.2 Ionospheric irregularities effects satellite signal.....	20
3.3 Comparison of S_4 index calculated with different period.....	21
3.4 Cumulative distribution of S_4 for three time periods.....	22
3.5 Diurnal and seasonal variation of scintillation occurrences (Feb.2000-Jan.2001)	
(a) Three dimensional result.....	24
(b) Contour result projected from 3D result.....	24
3.6 Diurnal and seasonal variation of scintillation occurrences (Feb.2001-Jan.2002)	
(a) Three dimensional result.....	25
(b) Contour result projected from 3D result.....	25
3.7 Comparison of seasonal variation of scintillation and average TEC in 2000.....	26
3.8 Average intensity of all scintillation events in Feb. 2000-Jan.2001	
(a) Average amplitude fluctuation.....	27
(b) Average S_4 index.....	27
3.9 Average intensity of all scintillation events in Feb.2001-Jan.2002	
(a) Average amplitude fluctuation.....	28
(b) Average S_4 index.....	28
3.10 Classification of amplitude level scintillation in each months.....	29
3.11 Monthly comparison of scintillation occurrences and sunspot numbers.....	30
3.12 Average total electron content measured at both stations in 2000.....	31
3.13 Diurnal and seasonal variation of scintillation (Feb.2000-Jan.2001)	
(a) KMITL, Bangkok station.....	32

This material is reserved for educational use only, not allowed for commercial use.

Forbidden to modify the content, and cite the document when use.

LIST OF FIGURES (to)

Fig.	Page
(b) CMU, Chiang Mai station.....	32
3.14 S_4 index distribution (Feb.2000-Jan.2001)	
(a) KMITL, Bangkok station.....	33
(b) CMU, Chiang Mai station.....	33
3.15 Classification of amplitude level scintillation (Feb.2000-Jan.2001)	
(a) KMITL, Bangkok station.....	34
(b) CMU, Chiang Mai station.....	34
4.1 Power spectral density of scintillation signals.....	40
4.2 Variation of scintillation's spectral slope versus local time (Feb.2000-Jan.2002).....	43
4.3 Variation of scintillation's spectral index versus local time during 2000.....	44
4.4 Variation of scintillation's spectral index versus local time during 2001.....	45
4.5 Relation between spectral index and S_4 index (Feb. 2000-Jan.2002).....	46
4.6 Variation of Fresnel frequency and noise floor frequency versus local time (Feb.2000-Jan.2001).....	48
4.7 Variation of Fresnel frequency and noise floor frequency versus local time (Feb.2001-Jan.2002).....	49
4.8 Autocorrelation of scintillation signals.....	51
4.9 Determination of correlation interval using time lag.....	51
4.10 Normalized decorrelation time versus local time of particular scintillation events in 2000.....	53
4.11 Normalized decorrelation time versus local time of particular scintillation events in 2001.....	54
4.12 Relation between decorrelation time and S_4 index (Feb.2000-Jan.2002).....	55
5.1 Comparison between experimental data, Nakagami-m and Gaussian probability density function of KMITL and CMU scintillation.....	65
5.2 Comparison between experimental data, Nakagami-m and Gaussian cumulative distribution function of KMITL and CMU scintillation.....	66
5.3 Cumulative distribution of amplitude fluctuation at KMITL station	
(a) Strong scintillation.....	67

This material is reserved for educational use only, not allowed for commercial use.

Forbidden to modify the content, and cite the document when use.

LIST OF FIGURES (to)

Fig.	Page
(b) Weak scintillation.....	67
5.4 Fade duration distribution at different fade levels for all scintillation events occurred in Feb.2000-Jan.2001.....	69-70
5.5 Fade duration distribution at different fade levels for all scintillation events occurred in Feb.2001-Jan.2002.....	70-71
5.6 Cumulative numbers of signal fading exceeded the specific fade levels (Feb.2000-Jan.2002).....	73
5.7 Total fade duration time of signal fading exceeded the specific fade levels (Feb.2000-Jan.2002).....	74
5.8 Effect of the scintillation on the perfect messages reception for various message lengths and fade margin levels (Feb.2000-Jan.2001).....	75-76
5.9 Effect of the scintillation on the perfect messages reception for various message lengths and fade margin levels (Feb.2001-Jan.2002).....	77-78
6.1 Probability density function of log-scintillation variance $\rho(\ln \sigma_{\chi}^2)$	82
6.2 Long-term probability density function $\rho(\chi)$ of scintillation amplitude	
(a) $\sigma_{\sigma} = 0.718$, $\sigma_m = 0.618$	84
(b) $\sigma_{\sigma} = 0.697$, $\sigma_m = 0.683$	84
(c) $\sigma_{\sigma} = 0.922$, $\sigma_m = 0.134$	84
(d) $\sigma_{\sigma} = 1.26$, $\sigma_m = 0.219$	84
6.3 Comparison of all long-term probability density function models	
(a) $\sigma_{\sigma} = 0.718$, $\sigma_m = 0.618$	86
(b) $\sigma_{\sigma} = 0.697$, $\sigma_m = 0.683$	86
(c) $\sigma_{\sigma} = 0.922$, $\sigma_m = 0.134$	86
(d) $\sigma_{\sigma} = 1.26$, $\sigma_m = 0.219$	86
6.4 Cumulative distribution function of channel capacity of scintillation channel compared with free space case (linear scale).....	90

This material is reserved for educational use only, not allowed for commercial use.

Forbidden to modify the content, and cite the document when use.

LIST OF FIGURES (to)

Fig.	Page
6.5 Cumulative distribution function of channel capacity of scintillation channel compared with the minimum capacity for M-PSK system (logarithm scale)....	90
6.6 Average BER for nonvariable scintillation intensity $\sigma_\sigma = 0, \ln \sigma_m^2 = \ln \sigma_\chi^2$ for CPSK (solid line) and NCFSK (dash-dot line) modulation techniques.....	95
6.7 Average BER for variable scintillation intensity $\sigma_m = 0.5, \sigma_\sigma = 0.25, 0.5$ $\sigma_\sigma = 0.718, \sigma_m = 0.618$ (curve d, i) and $\sigma_\sigma = 0.697, \sigma_m = 0.683$ (curve e,j)...	95
6.8 Average BER for nonvariable scintillation intensity ($\sigma_\sigma = 0$) for DS-SS technique with (a) $\sigma_m = 0$, (b) $\sigma_m = 0.4$, (c) $\sigma_m = 0.8$ and (d) $\sigma_m = 1.2$	97
6.9 Average BER for variable scintillation intensity for DS-SS technique with $\sigma_m = 0.5$ and (a) $\sigma_\sigma = 0$, (b) $\sigma_\sigma = 0.5$, (c) $\sigma_\sigma = 0.75$ and (d) $\sigma_\sigma = 1$	97
6.10 Average BER for different numbers of active users ($\sigma_\sigma = 0.697$ and $\sigma_m = 0.683$).....	98
A.1 The pattern of electric currents movement.....	108
A.2 Ionized particles flow forming the equatorial anomaly in daytime.....	108
B.1 Geometry for consideration of Fresnel zone.....	110
C.1 Schematic presentation of Earth-space paths between 2 stations (GMS-5 to KMITL and GMS-5 to CMU).....	112
D.1 Binary correlator receiver (a) Using a single correlator (b) Using two correlators.....	114
D.2 Conditional probability density functions: $p(z s_1), p(z s_2)$	114
E.1 Two-dimensional signal space.....	116
F.1 Noncoherent detection of FSK using envelope detectors.....	121

CHAPTER 1

INTRODUCTION

1.1 Literature of Ionospheric Scintillation

In more than two decades, satellite communication technology has grown rapidly from being revolutionary to commonplace, from an idea to worldwide services. At present, the provision of land mobile satellite service becomes apparent especially for radio frequency 1-3 GHz implemented with the regional geostationary (Regional GEO) or the big low-earth-orbiting (Big LEO) satellites. For many years, many communication satellites have been maintained in Regional GEO so that the earth station's antenna could point to a fixed location; hence the signal degradation might be caused by ionospheric scintillation via that fixed propagation path. Also for LEO system, because of the closet proximity of satellites orbits to the earth at the level about 900 km., the signal may also increase the risks of amplitude and phase scintillation or terrain and buildings shadowing (Mangir, n.d. :395).

The earth space radio path is rather complex in structure, and it includes the boundary layer, the irregularities structure and cloud. A radio signal traversing this path is affected by this medium in a random way and results in random variation. This variation in turn modifies the amplitude and phase of the signal, well known as scintillation. This variability has the significant impact on the magnitude of the theoretical degradation on the communication link, especially it becomes important for low margin system. The scintillation can become strong enough to cause significant impairments to the satellite link. It then becomes necessary for the system designer to allow the effect of scintillation when planning the satellite link. Knowledge on the dynamic characteristics of scintillation is also important for the up-link power control and antenna tracking system design. Many scientists and engineers have ever studied on ionospheric scintillation for a long time, mostly in high and medium geomagnetic latitude regions. On the other, ionospheric scintillation research around geomagnetic equatorial zone where the stronger scintillation usually occurs has rarely been studied and also its effect impact on satellite communication system is rarely considered.

1.2 The Significant of the Study

This study is in the scope of the ionospheric scintillation characteristics effected on 1.694 GHz satellite signal. The morphological results can inform the intensity of the scintillation that affects the amplitude signal diurnally and seasonally. The amplitude signal fluctuating above the mean reference level rapidly can lead to the large enhancement that can increase the intermodulation noise in satellite transponder, and also, results in the worsening of carrier-to-interference ratio (C/I) in multicarrier FDMA system. On the other hand, when the signal fluctuates below the mean level exceeding the system threshold level, the signal fading can occur leading to the fade out of communication signals as shown in Fig.1.1. Many signal dropouts of the GMS-5 satellite image as shown in Fig. 1.1(b) caused by scintillation can be observed when comparing with the clear air condition in Fig. 1.1(a). The results of the scintillation occurrences, the diurnal and seasonal variation, the statistical distribution of the large enhancement and signal fading are the important information for obtaining the communication planing via satellite link or system margin design appropriately to the real condition under scintillation effects in each station.

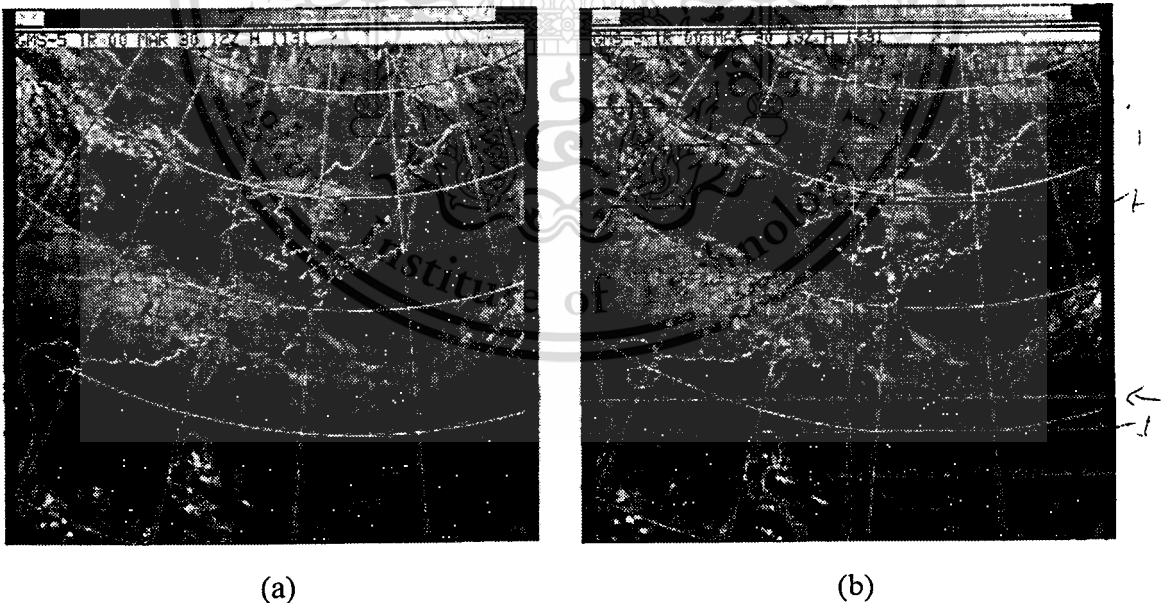


Fig. 1.1 GMS-5 satellite images observed on March 30, 2000 (Maruyama. 2000)

(a) clear air condition (b) scintillation condition

The scintillation data are extremely interesting since, on the one hand, they can be used to examine the various statistical properties of scintillating gigahertz signal, on

the other hand, the physical and dynamical characteristics of the ionospheric irregularities structures that cause the ionospheric scintillation can be revealed. Then the statistical analysis of amplitude scintillation such as power spectrum and autocorrelation analysis are also considered in order to examine the relation between irregularities' bulk and ionospheric scintillation of that propagation path.

1.3 The Objective and Chapters' Synopsis of the Thesis

The objective of this thesis is to study the characteristics of the ionospheric scintillation that effect 1.694 GHz satellite signal, and to analyze its statistical results for system impact approximation. Moreover, the system performance evaluation will be considered to show the system vulnerability under ionospheric scintillation effects, nevertheless the advanced modulation system being employed. Some theoretical analyses are applied in this thesis; for instance, the normal distribution has been found to be the good fitting for amplitude deviation from its mean level, and the cumulative amplitude distribution including of short-term and long-term analysis can describe various levels of signal fading. Furthermore, power spectrum analysis and autocorrelation function can estimate average fade rates and ground correlation distances that using for spaced diversity antenna (Banerjee *et.al.* 1992). The statistical long-term amplitude distribution and rms intensity are approximated using the Moulslley-Vilar model (Moulslley and Vilar. 1982) and the analytical approximation, then the channel capacity and the average probability of bit error can be estimated for some digital modulation conditions.

The method and results are provided in the reminder of this thesis as follows:

Chapter 2 introduces the basic knowledge of ionospheric scintillation such as the irregularities structures, the amplitude fluctuation process due to signal propagates through the irregularities. The predominated factors for scintillation intensity such as the geomagnetic latitude position, solar activity, diurnal and seasonal variation are also presented. Moreover, many forms of scintillation index informing the scintillation intensity are also presented.

Chapter 3 shows the system configuration and the morphological results. The scintillation characteristics such as scintillation intensity, occurrence numbers, amplitude fluctuation, diurnal and seasonal variation are presented. Moreover, the different characteristics of ionospheric scintillation in case of different latitudinal

This material is reserved for educational use only, not allowed for commercial use.

Forbidden to modify the content, and cite the document when use.

positions are also studied by comparing the scintillation at KMITL and CMU station.

Chapter 4 presents the analysis of frequency-time structure of the instantaneous scintillation to which the variation of the irregularities relates. The power spectral density has been used to evaluate the frequency structure; on the other, the autocorrelation function has been used to evaluate the time structure. From the PSD analysis, the spectral slope, spectral index, Fresnel frequency and etc. can be obtained, and used to study the diurnal and seasonal variations. The correlation interval or decorrelation time or coherent time can be obtained from autocorrelation function. This also presents the diurnal and seasonal variation, and the relation with the increases of scintillation index. Furthermore, these structures relate to the useful information for communications such as the scintillation rate and the decorrelation distance values for space diversity antenna planning.

Chapter 5 evaluates the statistical amplitude distribution and fade analysis. The experimental amplitude fluctuation distribution is compared and fitted with the theoretical model such as Gaussian and Nakagami-m distributions for both of PDF and CDF. The fade statistic analysis including of the fade duration distribution, the cumulative numbers and the total fade duration of signal fading exceeded any specific fade levels can lead to the message reliability analysis of scintillation channel.

Chapter 6 evaluates the long-term scintillation modeling using Moulslley-Vilar model and the analytical approximation. These models are compared with the experimental data and Gaussian distribution. The estimation of system performances such as channel capacity and average BER under scintillation condition can be derived by using these amplitude scintillation modeling. The average probability of bit error and the average signal-to-noise ratio are estimated; and present the communication impacts for CPSK, NCFSK and DS-SS modulation techniques.

Chapter 7 summarizes the material that is obtained in the preceding chapters; and proposes the discussion for future work.

Finally, other related topics are also included in the appendices; such as, the electrodynamics characteristics and the plasma movement, and the Fresnel zone radius are introduced in Appendix A and Appendix B respectively. The calculation of the slant path length between two different stations is explained in Appendix C. Finally, the estimation of the probability of bit error for binary detection of CPSK and NCFSK is described in Appendix D, E and F.

This material is reserved for educational use only, not allowed for commercial use.

Forbidden to modify the content, and cite the document when use.

CHAPTER 2

SATELLITE SIGNAL AMPLITUDE SCINTILLATION

With the rapid increase in the operational reliance on satellite communications, the need for predicting communications outages has become apparent. One of the major causes of satellite communications outages is satellite signal fading due to scintillation. Scintillation of the satellite signal is the relatively rapid fluctuation of the signal across its mean level that is either constant or changing much more slowly than the scintillation. There are 2 types of the fluctuation; the amplitude fluctuation which can be observed clearly; on the contrary, the phase fluctuation which is more complicated to define. The intensity of amplitude fluctuation depends on the occurrence time and the characteristic of the atmospheric layer through which the signal propagates. In general, the amplitude scintillation is defined as ionospheric scintillation due to the ionospheric irregularities in F layer and E_s layer; and the other is tropospheric scintillation due to small-scale refractive index variations in the atmosphere. These refractive index variations are the results of the temperature, humidity and pressure irregularities called the atmospheric turbulence (Dabas *et.al.* 1991). This research studies on 1.694 GHz satellite signal with the elevation angle of 42.40°; consequently, the signal is mostly effected by the ionospheric scintillation.

2.1 Ionospheric Scintillation

Ionospheric scintillation results when the irregularities of the electron density in the ionosphere interfere with radio waves that traveling through the ionosphere. These signals are subjected to the variation of both amplitude and phase. The signals are not attenuated by the irregularities but their energy is redistributed instead (Hocutt. 1988). The signal fluctuation varies widely with frequency, geomagnetic, solar activity, time, season and latitude position. The irregularities leading to scintillation are predominantly in the F layer at altitudes ranging from 200 to 1,000 km., especially between 250 and 400 km. for the irregularities at the primary disturbance region at high and equatorial latitude. There are some evidences that E layer irregularities at the 90-100 km. region, particularly, Sporadic E and auroral E, can also cause the scintillation. In generally, there are three main regions where ionospheric scintillation

This material is reserved for educational use only, not allowed for commercial use.

Forbidden to modify the content, and cite the document when use.

predominates. The equatorial region comprises the area within $\pm 20^\circ$ of the geomagnetic equator. Secondary, the high latitude region comprises the area from the high latitude edge of the trapped charged-particles boundary to the polar region. All of other last regions are termed as middle latitude. Another important term, ionospheric turbulence or ionospheric irregularities are defined as the presence of small-scale irregularities structures, centimeters to meters size, or the irregularities embedded in the large-scale tens of kilometers around the ionosphere.

2.1.1 Ionospheric Irregularities

Plasma irregularities of the ionosphere can strongly disturb radio communication and navigation. In normal condition, small-scale irregularities are generated just after sunset in the equatorial regions and may last for several hours. At high latitudes, these irregularities maybe generated during either the daytime or nighttime. These small-scale irregularities occur frequently during the maximum solar cycle period. On the other, the large-scale irregularities cause spread F condition leading to the degradation of HF signal. The structure of the irregularities has a shape likely to a banana or an orange segment. The characteristics of the structure development, motion and decay can be summarized as follows (Aarons. 1982).

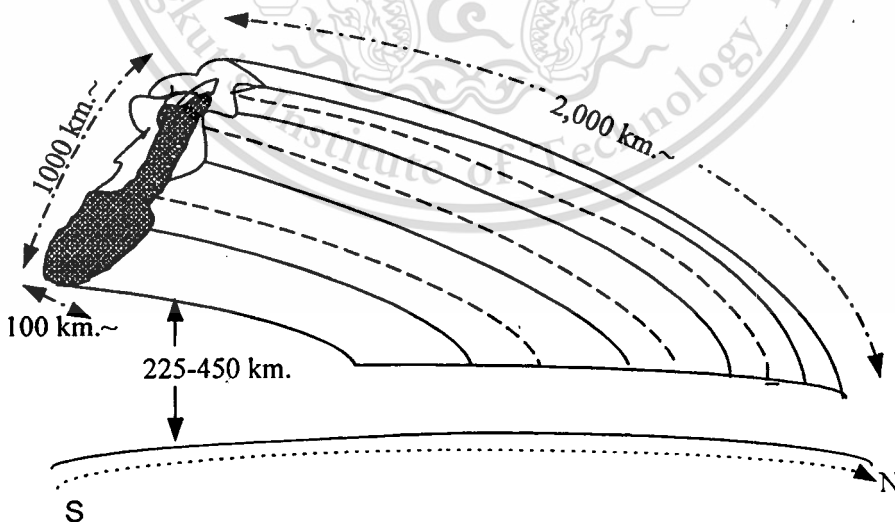


Fig. 2.1 Three dimensional of the irregularities structure

a) A new patch forms after sunset by expanding to westward, then it becomes an abrupt halt after typically expanding to an east-west dimension of 100 to several

hundred kilometers. The minimum size about 100 km. can be appeared. The north-south dimensions are about 2,000 km. or larger.

b) The patch is composed of the field-aligned elongated rod or sheet irregularities. The vertical thickness of the patch is 50 to several hundred kilometers. The maximum intensity of the irregularities is at the high region from 225-450 km. with irregularities size over 1,000 km.

c) The patch drifts eastward with velocities ranging from 100-200 m/s at postsunset and gradually declines in speed. After local midnight, these irregularities movement will be halt and reverse the direction. Then westward drift gradually increase its velocity.

d) According to the studies of irregularities patches in low and medium solar activity years (Livingston *et.al.* 1980), the patches decay after midnight for one hour period. Some results also showed the weak 3 meters size of the irregularities.

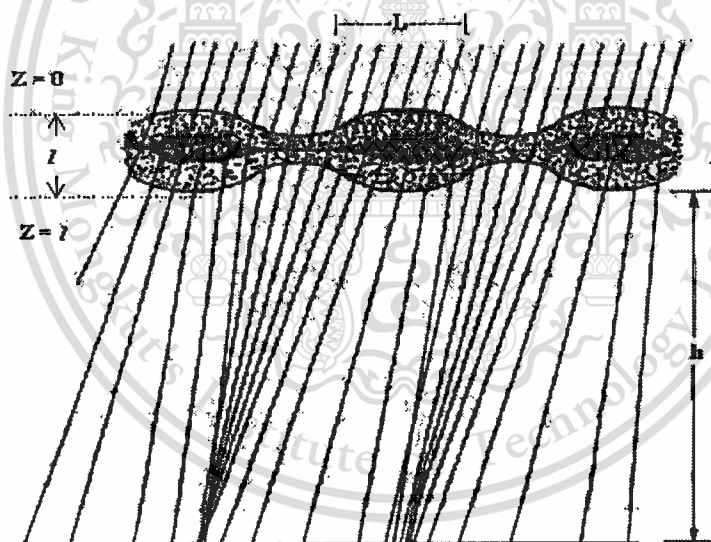


Fig. 2.2 Simplified representation of the ionospheric irregularities

When the irregularities which result in spread F are observed, the signal strength variation is also observed then the ionospheric scintillation phenomenon can be modeled. Let us consider the condition shown in Figure 2.2. A region of random irregularities structures is located from $Z=0$ to $Z=l$. When a time harmonic electromagnetic wave incidents on the irregularities slab at $Z=0$ and received on the ground at $(\vec{\rho}, z)$. It will be assumed that the irregularities slab can be characterized by a dielectric permittivity.

$$\varepsilon = \langle \varepsilon \rangle [1 + \varepsilon_1(\vec{r}, t)] \quad (2.1)$$

where $\langle \varepsilon \rangle$ is the background average dielectric permittivity which for the ionosphere is given by

$$\langle \varepsilon \rangle = (1 - f_{p0}^2 / f^2) \varepsilon_0 \quad (2.2)$$

and $\varepsilon_1(\vec{r}, t)$ is the fluctuation part characterizing the random variations caused by the irregularities and is given by

$$\varepsilon_1(\vec{r}, t) = - \frac{(f_{p0}/f)^2 [\Delta N(\vec{r}, t) / N_0]}{1 - (f_{p0}/f)^2} \quad (2.3)$$

Here, f_{p0} is the plasma frequency corresponding to the background of the electron density N_0 , and f is the frequency of the incident wave.

The total field intensity at the ground is the sum of the unperturbed components and the perturbations in field intensity due to the irregularities. The perturbations are generated by the electrical currents flowing in the irregularities due to the incident field intensity. These currents have the different density when comparing with the surrounding ionosphere. Therefore, the irregularities act roughly as the conical radiating antennas as shown in Fig. 2.2. The incident signals scatter refractively or diffractively depending on the scale size of the irregularities that is perpendicular to the planar waves. Refractive scattering that resulting strong scattering is considered to involve with the large-scale irregularities, larger than the Fresnel size (Appendix B); and diffractive scattering is assumed to involve with the irregularities that is smaller or equal to the Fresnel zone size. When a large number of small-scale irregularities being considered as a diffractive grating, then the movement of the irregularities across the radiowave propagation path will cause various patterns of the diffraction. The drift velocity ν of the screen can be estimated from (Allnutt. 1989).

$$\nu = \sqrt{\lambda z} f_{\min} \quad \text{meter/s} \quad (2.4)$$

This material is reserved for educational use only, not allowed for commercial use.

Forbidden to modify the content, and cite the document when use.

where λ : wavelength of the signal

z : the height of the diffraction screen

f_{\min} : the first Fresnel minimum frequency

It is generally agreed that all cases of scintillation are due to the diffractive scattering.

2.1.2 The Irregularities' Characteristics

The Fresnel scale size is introduced in Appendix B by considering the distance between transmitting and receiving locations, $d = d_T + d_R$. The first Fresnel zone radius, F_1 , at distance d_T from the transmitter and d_R from the receiver is given by (Flock. 1983).

$$F_1 = \sqrt{\frac{\lambda d_T d_R}{d}} \quad (2.5)$$

If the distance to the transmitter d_T is very larger than d_R , d_T approaches to be d . Then the first Fresnel zone radius is

$$F_1 = \sqrt{\lambda d_R} \quad (2.6a)$$

When considering the first Fresnel zone in cross section, the zone is circular with the area of πF_1^2 . Correspondingly to the irregularities in Fig. 2.2, the radius or scale size L is equivalent to F_1 at a height z above the point of the observation. Equation (2.6a) becomes

$$L = \sqrt{\lambda z} \quad (2.6b)$$

then

$$z = L^2/\lambda \quad (2.7)$$

Comparing Equation (2.6a) and (2.6b) can find that L and z take the places of F_1 and d_R respectively.

The ionospheric layer or screen contains identical roughly isotropic or ellipsoidal irregularities of scale size L , as show in Fig. 2.2. From Equation (2.1-2.3), the irregularities of the screen can be characterized by the deviation of the electron density, ΔN , surrounding its layer. The corresponding deviation Δn of the refractive index can be determined by (Flock. 1983 ; Lawrence *et.al.* 1964).

$$\Delta n = -40.3 \frac{\Delta N}{f^2} \quad (2.8)$$

thus the mean square value of Equation (2.8) is given by

$$\overline{(\Delta n)^2} = 1.624 \times 10^3 \frac{\overline{(\Delta N)^2}}{f^4} \quad (2.9)$$

Equation (2.9) can be rewritten in a new form as

$$\frac{\overline{(\Delta n)^2}}{n} = \frac{1}{4\pi^2} r_e^2 \lambda^4 \overline{(\Delta N)^2} \quad (2.10)$$

where r_e is the electron radius (2.82×10^{-15} m.) and n is essentially unity. Δn can be either a positive or negative value. For a single irregularity of effective thickness L , the phase deviation $\Delta\phi$ can be calculated.

$$\Delta\phi = \left(\frac{2\pi}{\lambda}\right)(L\Delta n) \quad (2.11)$$

where $2\pi/\lambda$ is the phase constant.

In a distance D along the propagation path, it is assumed to have D/L irregularities; and all irregularities have the same size. The total mean-square phase deviation of these irregularities is

$$\overline{(\Delta\phi)^2} = \frac{D}{L} \left(\frac{2\pi L}{\lambda}\right)^2 \overline{(\Delta n)^2} \quad (2.12)$$

This material is reserved for educational use only, not allowed for commercial use.

Forbidden to modify the content, and cite the document when use.

Equation (2.12) can be written in term of the electron density variation by

$$\overline{(\Delta\phi)^2} = \frac{D}{L} \left(\frac{2\pi L}{\lambda} \right)^2 \left(\frac{1.624 \times 10^3 \overline{(\Delta N)^2}}{f^4} \right) \quad (2.13)$$

If consider with the layer of thickness D at a zenith angle θ_z and substitute Equation (2.10) for $\overline{(\Delta n)^2}$ part (see Equation (2.9)) into Equation (2.13); then Equation (2.13) can be simplified to (Booker. 1975).

$$\overline{(\Delta\phi)^2} = 4r_e^2 \lambda^2 \overline{(\Delta N)^2} LD \sec \theta_z \quad (2.14)$$

The relation between phase variations and amplitude variations is considered here. Amplitude variations are built up from signals which are modulated only in phase by the ionospheric irregularities. Only phase variations occur immediately below the screen but amplitude variations develop farther below the screen in the order of the Fresnel distance (Equation (2.7)). From Fig. 2.2, if $h > \frac{\pi L^2}{\lambda}$ then amplitude fluctuations are developed (Booker. 1975). The vector representation of the amplitude and phase variations is presented in Fig. 2.3. The relation between both fluctuations can be described by

$$\left(\frac{\Delta A}{A} \right)^2 = \overline{(\Delta\phi)^2} \quad (2.15)$$

ΔA presents a quantity that adds with random phase A to produce amplitude fluctuations.

The amplitude scintillation intensity increases gradually with farther distances below the ionospheric irregularities. But an intensity index (see Section 2.3) remains less than unity for weak scintillation. For strong scintillation, the scintillation index can reach a unity and saturate or limit at that value. On the other hand, phase scintillation does not reach a saturation point; but it increases continuously with the increasing of the intensity. According to Fig. 2.2, the conical beamwidth is about

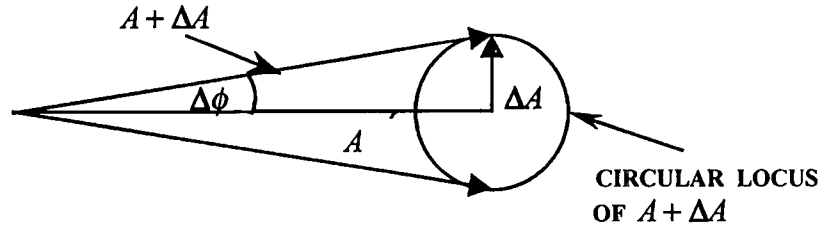


Fig. 2.3 Vector representation of amplitude and phase scintillation

λ/L . The larger the irregularities, the narrower the beamwidth is; and vice versa. At the observation point below the layer with the distance d , much less than the Fresnel distance ($z = L^2/\lambda$), only one beam is intercepted; and only phase variations occur. For farther distances, the cones of radiation overlap and interfere with each other then amplitude scintillation occurs. The diffracting screen or layer produces an angular spectrum of planewaves; and the interference between the planewaves produces the amplitude scintillation.

2.1.3 Geometrical Consideration of the Ionospheric Irregularities

The intensity of the observed scintillation depends on the position of the observing station related with the ionospheric irregularities position. The thickness and the constant electron density deviation (ΔN) of that irregularities region and other geometrical factors are used to evaluate data and predict scintillation effects at that particular location.

Mikkelsen *et.al.* (1978) assumed the geometric variation of S_4 index (Section 2.3) as follows:

$$S_4 \propto \sqrt{(z/\cos\theta_z)f(\psi, \phi)} \quad (2.16)$$

where z : the reduced slant path to the irregularities layer = $\frac{z_1}{z_2}(z_2 - z_1)$ with

z_1 : the slant path to the irregularities layer

z_2 : the slant path to the satellite

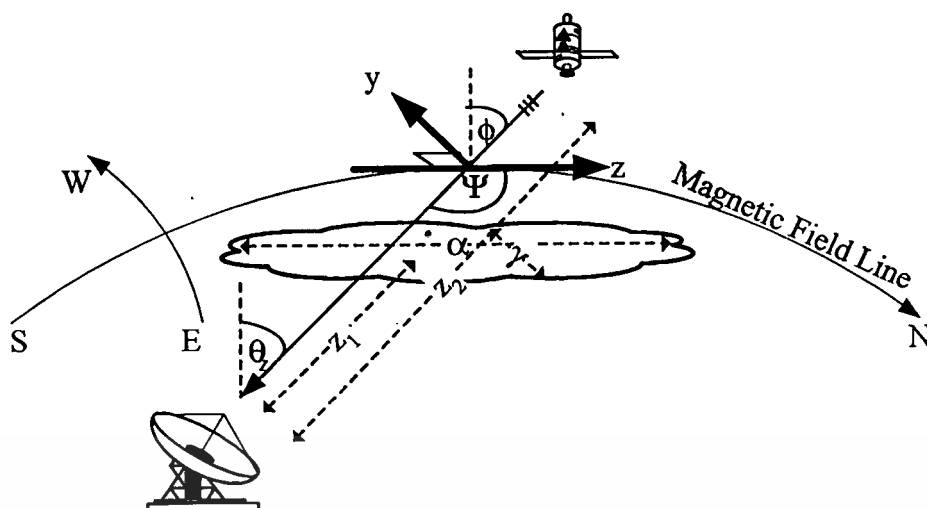


Fig. 2.4 Geometry of the ionospheric irregularities that effect radiowave signal

θ_z : the ionospheric zenith angle between the satellite signal and the irregularities layer

$$f(\psi, \phi) : \frac{\alpha\gamma(\gamma^2 \cos^2 \phi + \sin^2 \phi + \cos^2 \psi (\cos^2 \phi + \gamma^2 \sin^2 \phi) + \alpha^2 \sin^2 \psi)}{(\gamma^2 \cos^2 \psi + \alpha^2 \sin^2 \psi (\gamma^2 \cos^2 \phi + \sin^2 \phi))^{\frac{1}{2}}}$$

where

ψ : propagation angle = angle between the satellite signal and the direction of magnetic field line

ϕ : azimuth of the satellite signal in local ordinate system of z axis along the magnetic field line and y axis in the magnetic east-west direction

α : the ionospheric irregularities elongation along the magnetic field line

γ : the ionospheric irregularities elongation in the east-west direction of the magnetic

2.2 Related Factors of Ionospheric Scintillation Occurrence

The characteristics of ionospheric scintillation relate with many dependent factors. Its correlation factors can be summarized as following and described by Fig. 2.5 (Rec. ITU-R P.531-4. 1997).

This material is reserved for educational use only, not allowed for commercial use.

Forbidden to modify the content, and cite the document when use.

2.2.1 Geomagnetic Latitude Dependence

Geographically, there are two intense zones of gigahertz ionospheric scintillation, one at high latitude regions; and the others occur particularly in anomalous regions within $\pm 20^\circ$ of the geomagnetic equator. The second regions are remarkable for geostationary satellite links. Severe gigahertz scintillation is generally observed in these two regions; whereas scintillation mainly effects VHF signals in the middle latitude regions.

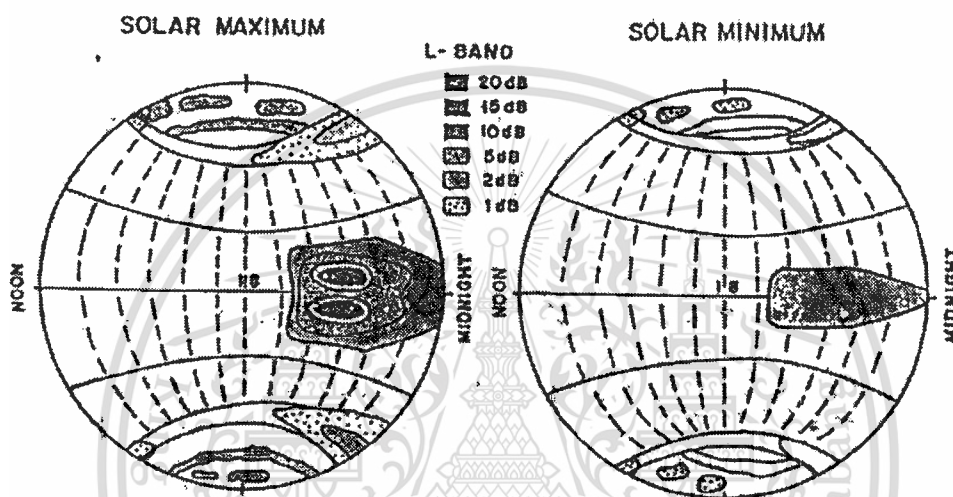


Fig. 2.5 Scintillation intensity during solar maximum and minimum years

2.2.2 Solar Activity and Sunspot Numbers Dependence

The long-term scintillation activity has a positive correlation with the variation of solar activity. According to Fig. 2.5, the characteristics of scintillation intensity are different due to the maximum and minimum solar activity. Annual scintillation activities vary in solar cycle every 11 years. In year 2000 was the 23rd solar cycle. Consequently, if long-term data has been analyzed for many years, the annual scintillation varies in solar cycle could be observed. An individual scintillation event does not have a good correlation with the daily sun-spot numbers. On the contrary, there is strong correlation between annual scintillation occurrences and the annual sun-spot numbers. Furthermore, the amplitude fluctuation of scintillation has a good correlation with the monthly sunspot numbers.

2.2.3 Diurnal and Seasonal Dependence

Seasonal variation of scintillation activity occurs severely at or just after the vernal and autumn equinox periods. Additionally, the daily scintillation's variation occurs approximately after sunset. For all regions, the nighttime scintillation is pronounced as also shown in Fig. 2.5. The diurnal activity differs according to the geomagnetic region, with the equatorial scintillation's intensity peaking at 20:00-21:00 LT (Local Time).

2.2.4 Signal Frequency and Elevation Angle Dependence

When the higher frequency signal propagates through the ionospheric irregularities slab, the signal will fluctuate more rapidly than the lower frequency. For more higher gigahertz frequency, if the elevation angle to satellite is lower, this leads to the long propagation path of travelling signal. In this case, the signal can be effected not only by ionospheric scintillation but also, mainly effected by tropospheric scintillation due to cloud turbulence. Therefore, it is better if the effects of these two types of scintillation are separated independently.

2.3 Scintillation Index

Several measures or indices of scintillation intensity have been used. The most general one, called peak to peak, finds the maximum and minimum peaks during any period. But the scintillation phenomenon has the variation, and is apparent so random in the fine detail on the one hand; but generally predictable in the gross features. Accordingly, the descriptor that can overcome this apparent randomness in the fine detail of the amplitude fluctuations, called scintillation index, can be defined as following.

2.3.1 SI Index

The index SI has been proposed as a convenient approximate measure of the scintillation intensity. SI is often used for first-order analysis of scintillation data.

$$SI = \frac{(P_{\max} - P_{\min})}{(P_{\max} + P_{\min})} \quad (2.17)$$

Where P presents the power signal. In order to avoid the overemphasizing conditions, the third maximum and minimum peak is recommended.

P_{\max} : The third peak down from the highest scintillation peak in one given period

P_{\min} : The third peak up from the smallest scintillation peak in one given period

2.3.2 S_4 Index

Scintillation index S_4 is the most commonly used parameter for indicating the intensity. Briggs and Parkins (1963) proposed series of indices termed as S_1 , S_2 , S_3 and S_4 . S_4 index is the one that relates with time defined as the standard deviation of received power divided by the mean value of the received power; and it can be averaged over any appropriate period.

$$S_4 = \left[\frac{\langle I^2 \rangle - \langle I \rangle^2}{\langle I \rangle^2} \right]^{\frac{1}{2}} \quad (2.18)$$

where I is the intensity of the signal amplitude; and $\langle \Rightarrow \rangle$ signifies the mean of the enclosed parameter. S_4 value of 0.5 is taken as the boundary between weak and strong scintillation. Occasionally, S_4 may exceed a unity or reach the value as high as 1.5. This is due to wave focusing caused by the irregularities. The following empirical relationship in Equation (2.19) is indicated for calculating SI from S_4 index (Rec. ITU-R P.531-4. 1997).

$$SI = 27.498S_4^{1.2697} \quad (2.19)$$

Since there are many useful methods to analyze scintillation intensity, the choice of method depends on the measurement conditions.

2.3.3 Standard Deviation

The amplitude fluctuation of scintillation is a crucial value; and it expresses the magnitude randomly around a mean value. This can be represented by

$$\sigma_x = \left(\frac{x_1^2 + x_2^2 + \dots + x_n^2}{n-1} \right)^{\frac{1}{2}} \quad (2.20)$$

where x_i is the relative value of amplitude fluctuation (the difference between the random value and its mean value \bar{x}). n is the whole number of data.

2.4 Conclusion

This chapter is concerned with the basic theories of the ionospheric scintillation, the characteristics of ionospheric irregularities, the important factors related to the ionospheric scintillation, and the intensity indication of this phenomenon. There are many parameters relate to the difference of the scintillation intensity, such as, especially the different observation station. Therefore the scintillation characterization might be better if the ionospheric scintillation is characterized in cases of the different station, latitudinal or longitudinal position. Furthermore, the ionospheric scintillation characteristics for solar maximum cycle should be considered, especially in this 23rd cycle that is maximum in 2000. Because of the complication and randomness of the irregularities medium, therefore, the satellite signal fluctuation has many particular characteristics that can be observed clearly; or analyzed by the theoretical analysis to determined more complicate characteristics. For examples, the scintillation intensity, the diurnal and seasonal variation, the frequency-time structure of the scintillating signals, the amplitude distribution, the scintillation fading analysis, etc, these will be discussed in the following chapters.

CHAPTER 3

EXPERIMENTAL SYSTEM AND MORPHOLOGICAL RESULTS

This chapter provides an overview of the observation system and some morphological results. The results show some characteristics of ionospheric scintillation of the satellite signals occurring at different locations, Bangkok and Chiang Mai. The data used to analyze and compare between these two locations have been received over one year period of 2000. In addition, there are some results presenting the ionospheric scintillation observation during 2 years period, 2000-2001, for only Bangkok station with more higher sampling data.

3.1 Configuration of the Experimental System

This experiment has been carried out from February 2000 receiving 1.694 GHz carrier wave of the telemetry signal transmitted from GMS-5 satellite (Geostationary Meteorological Satellite-5 or Himawari-5). The position of this satellite is at 140° E. The receiving station is at King Mongkut's Institute of Technology, Ladkrabang (KMITL) in Bangkok (100.8° E, 13.7° N, 2.8° N Geomagnetic latitude); and another observation station at Chiang Mai University (CMU: 99.0° E, 18.8° N, 7.9° N Geomagnetic latitude). The 1.8 meters parabolic antenna has the elevation angle of 42.40° . The data processing subsystem consists of a data collecting computer that samples the analog signals from receiving subsystem every 0.02 seconds (50 Hz), then analog data are converted to digital data. Two years scintillation occurrences at KMITL (Feb. 2000- Jan. 2002) and their statistical studies have been analyzed by using 0.2 seconds re-sampling data from the original one. Moreover, the comparisons of one year (Feb. 2000- Jan. 2001) ionospheric scintillation for different location are also presented here. According to the database access via internet for another station, CMU data, the median values of original sampling data (50 Hz) over 10 seconds intervals are stored there; then this sampling scintillation data are also used for analysis of the scintillation intensity in both stations. In this case, one scintillation occurrence is counted every 3 minutes period of scintillation event with the fluctuating amplitude exceeds $0.5 \text{ dB}_{\text{p.p}}$.

This material is reserved for educational use only, not allowed for commercial use.

Forbidden to modify the content, and cite the document when use.

Table 3.1 Satellite receiving system parameters

Position	100.8°E, 13.7°N (KMITL, BKK) 2.8° N Geomagnetic Latitude
	99.0°E, 18.8°N (CMU, Chiang Mai) 7.9° N Geomagnetic Latitude
Satellite Frequency	1694 MHz
Satellite Position	140 °E
Elevation angle to GMS-5	42.40° (KMITL), 38.84° (CMU)
Azimuth angle	106.2° (KMITL), 110.34° (CMU)
Antenna	1.8 diameter parabolic antenna Linear Polarization Gain: 27 dB
Low Noise Amplifier	Gain: 47.7 dB Noise Figure: 1.33

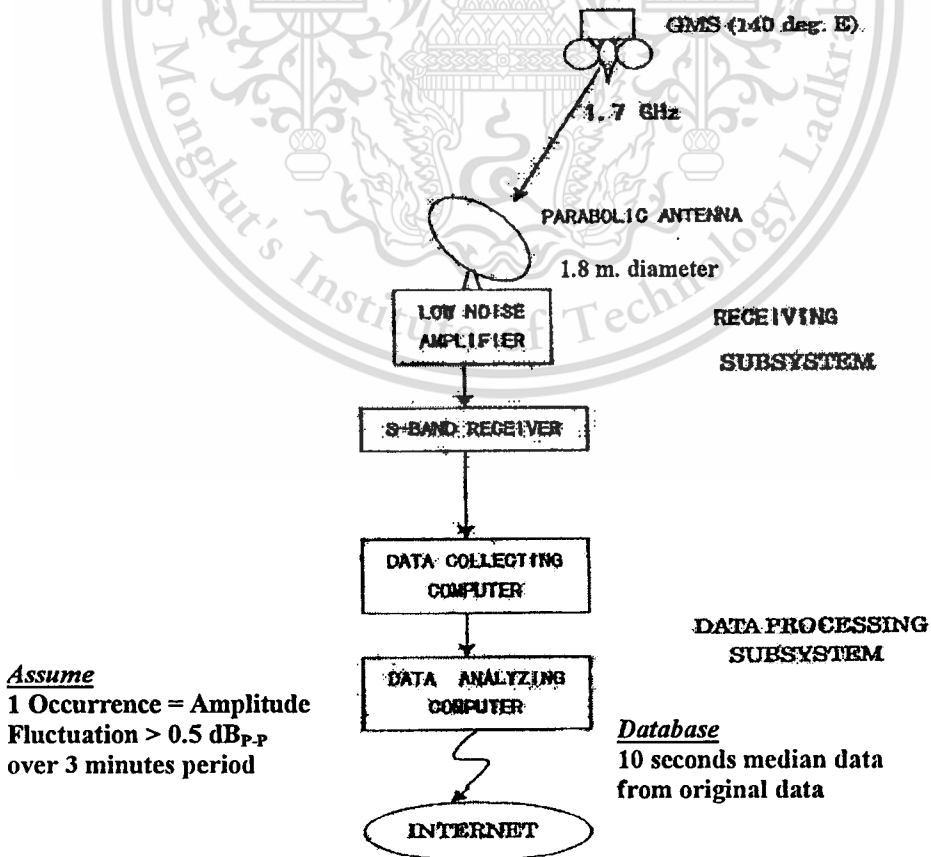


Fig. 3.1 Block diagram of ionospheric scintillation observation system

Table 3.1 summarizes the parameters related to the satellite signal reception for each station; and Fig. 3.1 describes the block diagram of scintillation observation system.

3.2 Morphological Results

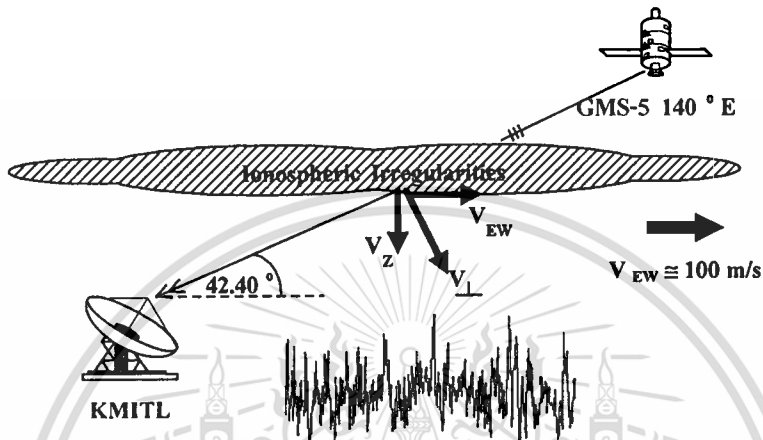


Fig. 3.2 Ionospheric irregularities effects satellite signal

When satellite signal propagates through the ionospheric irregularities, amplitude and phase signals will rapidly change. This leads to the communication outages when signal fading below the system threshold level. Because of the complicated analysis of phase scintillation, only the amplitude variation is considered in this study. For the equatorial region, the ionospheric irregularities moves eastward at postsunset time with the average velocity about 100 m/s. V_{EW} and V_Z are the east-west and vertical irregularities speeds respectively. These velocity components are the initial assumption of the irregularities drift at the 400 km. subionospheric point, and correspond to $V_{EW} : V_Z = 5:1$ (Mollen *et.al.* 1988). V_{\perp} is the drift speed perpendicular to the planar wave of satellite signals, given by

$$V_{\perp} = V_{EW} \sin \theta + V_Z \cos \theta \quad (3.1)$$

where θ is the elevation angle to satellite = 42.40° . Therefore, the perpendicular drift speed over the station can be estimated by Equation (3.2).

$$V_{\perp} = 100 \sin(42.40^\circ) + 20 \cos(42.40^\circ) = 82.12 \text{ m/s} \quad (3.2)$$

This material is reserved for educational use only, not allowed for commercial use.

3.2.1 Scintillation Intensity Analysis

The intensity of scintillation can be identified by various ways as mentioned in Chapter 2. However, only two scintillation intensity identifications, amplitude peak to peak and S_4 index, are considered in this thesis. S_4 index can be calculated over any appropriate period depending on the separation of the scintillation events. Two scintillation events are shown in Fig. 3.3 with the 1 minute calculation of S_4 index presenting below. According to the S_4 index, scintillation event observed at KMITL on 19 September 2000 was higher than scintillation event on 22 September that was the autumn equinox. From the same event in Fig. 3.3 (a) and (b), if calculate S_4 index with 3 and 5 minutes periods, time shifts between fluctuating peaks and S_4 index peaks can be observed as shown in Fig. 3.3 (c) and (d) respectively.

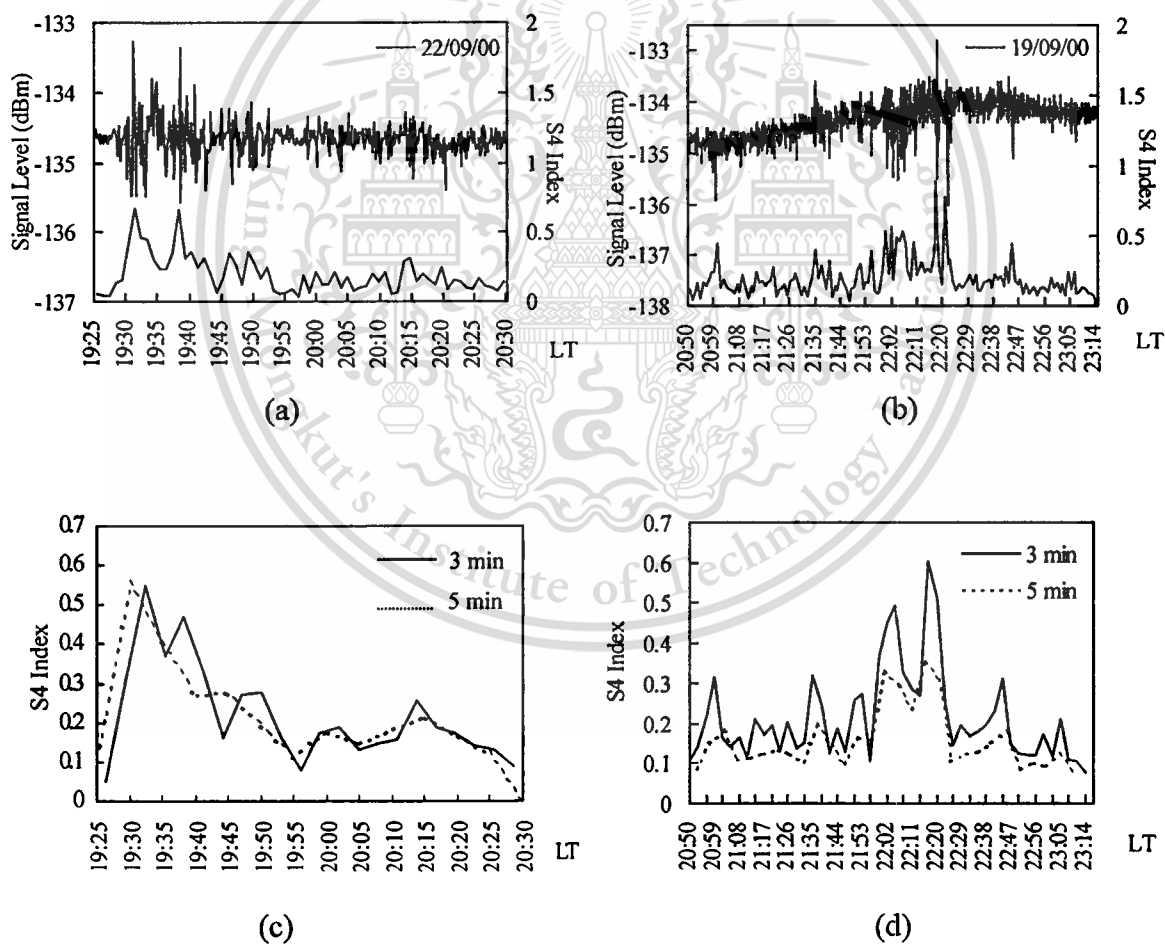


Fig. 3.3 Comparison of S_4 index calculated with different period

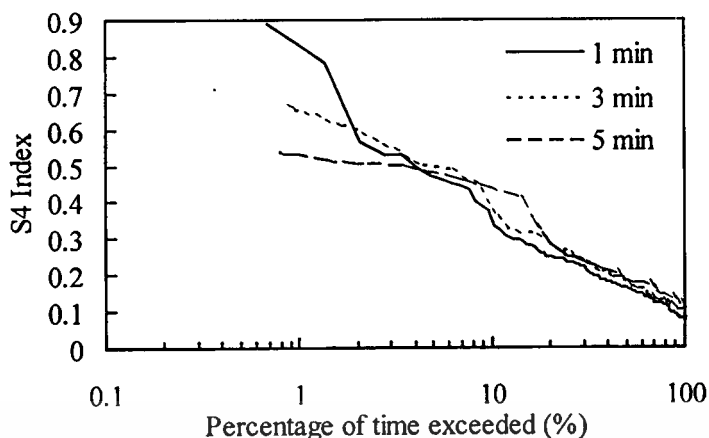


Fig. 3.4 Cumulative distribution of S_4 for three time periods

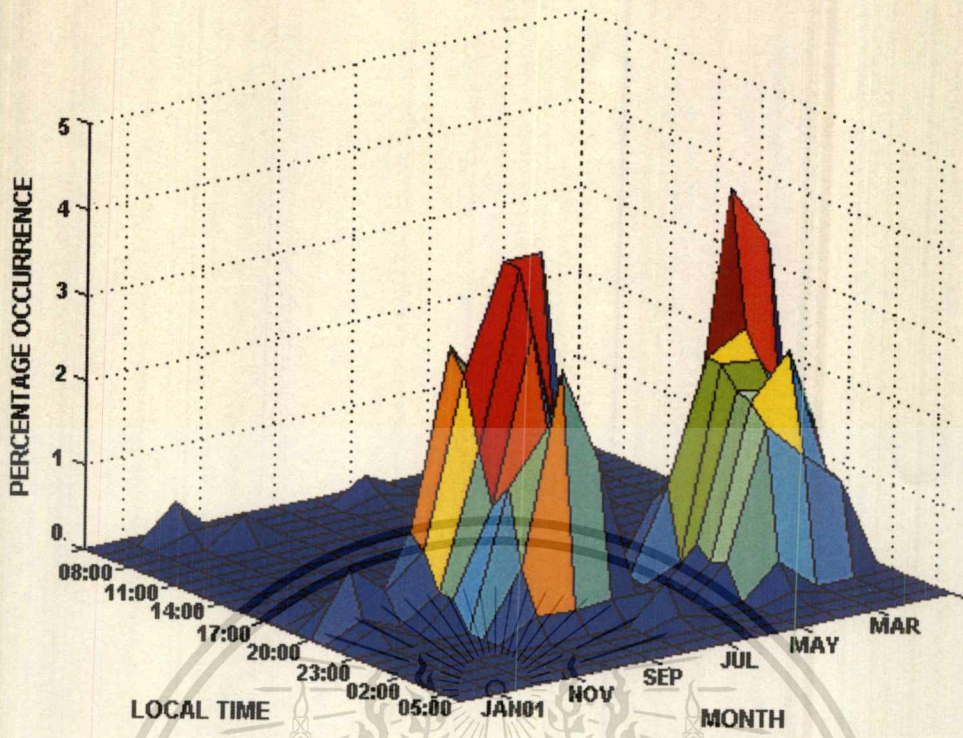
The time shifts between the signal fluctuation and S_4 index increase with the increasing of calculating period. This is not important for the statistical analysis; but this dependence of calculating period of S_4 should be considered when comparing scintillation events between various stations. Fig. 3.4 shows the cumulative distribution of S_4 index calculated over 1, 3 and 5 minutes periods for indicating the intensity of the same scintillation event. S_4 calculation in any period does not much differ with each other for weak scintillation, but the differences can be observed clearly for the strong scintillation. Although 1 minute period calculation can indicate the intensity of scintillation finely, this short period splits the continuous scintillation event separately without the appropriate information of irregularities. Consequently, study of statistical analysis or irregularities effects should be considered longer period such as 3 or 5 minutes instead.

3.2.2 Diurnal and Seasonal Variation

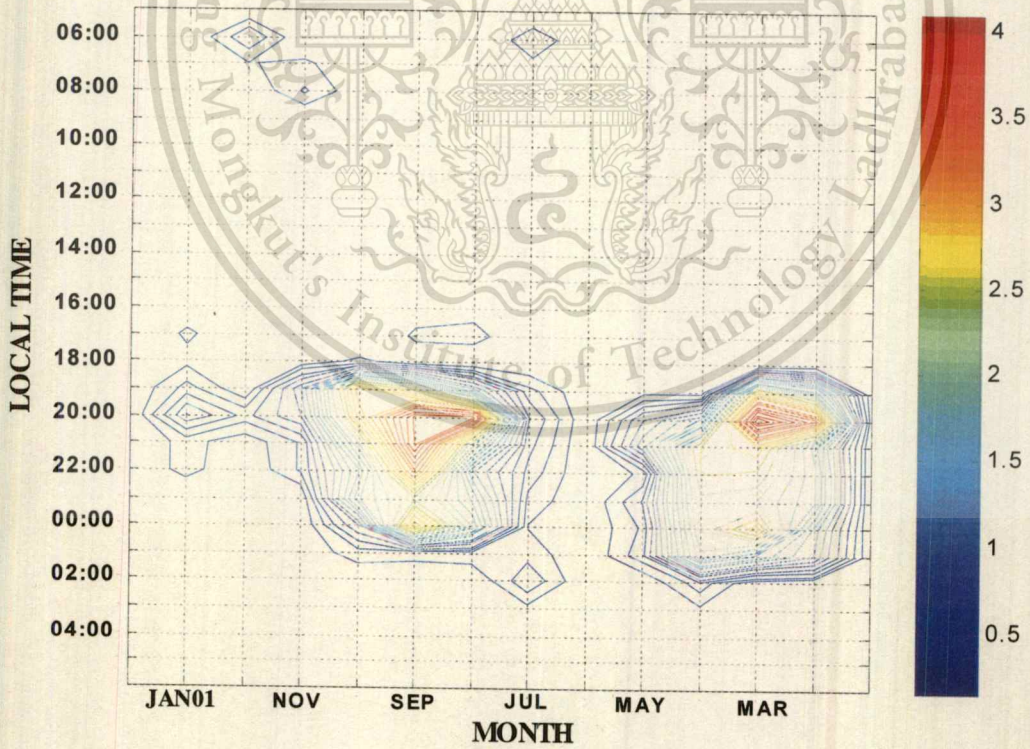
The morphological study of 1.694 GHz scintillation at KMITL has been presented here. Data are analyzed by using 0.2 seconds sampled data to determine the occurrence numbers of scintillation events and S_4 index. Scintillation events that effect 1.694 GHz satellite signal have been observed since February 2000, during the maximum solar cycle year, until January 2002. This scintillation is the nighttime scintillation and mostly occurs after sunset until after midnight. Moreover, daytime scintillation events can be observed sometimes. Fig. 3.5 and Fig. 3.6 present the percentage occurrence of scintillation events of 2000 and 2001 year respectively in diurnal and seasonal variation. Scintillation occurred in 2000 totally 2756 events, and

2516 events in 2001. For diurnal variation results, scintillation generally occurred during 18.00-02.00 LT (Local Time) in 2000, but for 2001 some events extensively occurred until 04.00 before sunrise. The scintillation mostly occurred at 20.00 LT in February-March and August-September in 2000. On the other hand in 2001, scintillation occurring most at 20.00 LT in September can be observed obviously. But during period of autumn equinox, March and April, scintillation mostly occurred at 20.00 LT and 23.00 LT respectively. Some daytime scintillation occurrences in July, November and December 2000, and also, October 2001 and January 2002 can be observed as described in the results. These might be the results when scintillation was caused by irregularities in the electrojet region (See Appendix A) (Bhattacharyya *et.al.* 1992).

When considering seasonal variation, the results can be described that scintillation percentage occurrence gradually increased from January and reached maximum in March or April, after that its occurrence decreased and was minimum in June and July. In June 2000, scintillation occurrence was not analyzed due to the system broke down in this month (both stations: KMITL and CMU), however the scintillation occurrence of this month could be predicted to be minimal than others. The occurrences grew increasingly again and were maximum in September, after that the percentage occurrence decreased gradually and was minimum in December. Seasonal variation of 1.694 GHz scintillation changed correspondingly to the change of average total electron content (TEC) of each month as shown in Fig. 3.7. Scintillation occurrences mostly occurred during both equinoctial periods (vernal and autumnal equinox in March and September) similarly to the variation of TEC. These were based on the movement of electron density. Fig. 3.8 and Fig. 3.9 illustrate the intensity of scintillation that varied diurnally and seasonally. The average amplitude fluctuation and S₄ index levels of all scintillation events related to each local time and months in 2000 and 2001 are presented respectively. The high amplitude fluctuation levels and S₄ index can be clearly observed at 22.00 and 02.00 LT in March 2000, 00.00-01.00 LT in April 2000, and 20.00-00.00 LT in May 2000. For the next equinox period, the high intensity of scintillation can be observed during 21.00 to 23.00 LT in September and October 2000. For year 2001, the high intensity of scintillation events can be observed at 22.00 and 02.00 LT in March and at 22.00-00.00 LT in September. Some high scintillation intensity events can be observed in January 2002 during 01.00 LT. However, these two figures present the average



(a) Three dimensional result

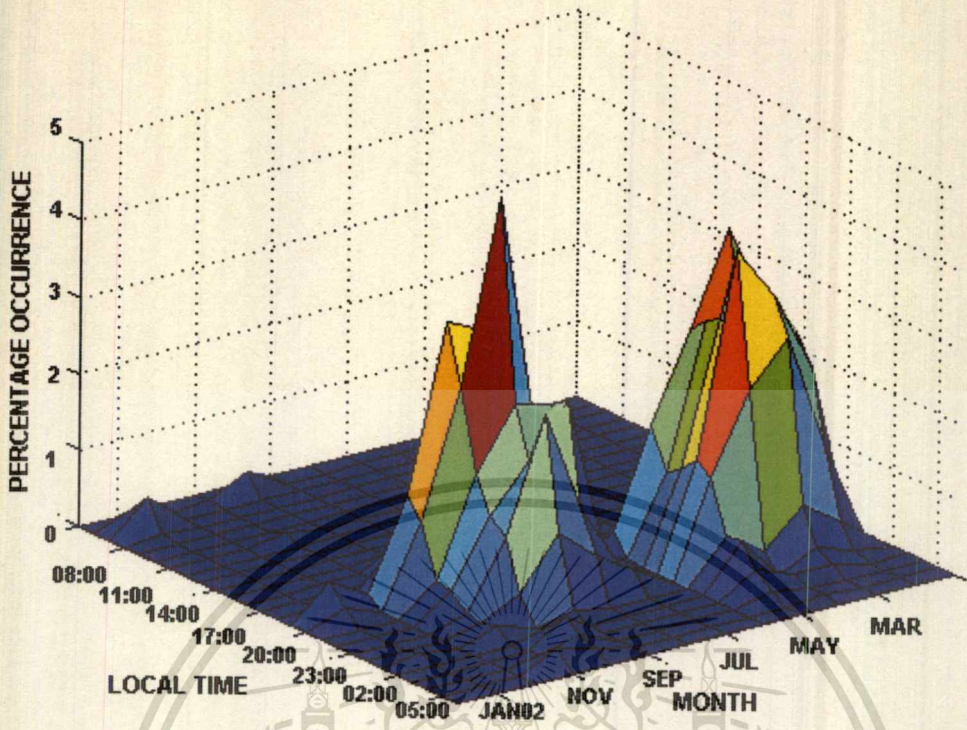


(b) Contour result projected from 3D result

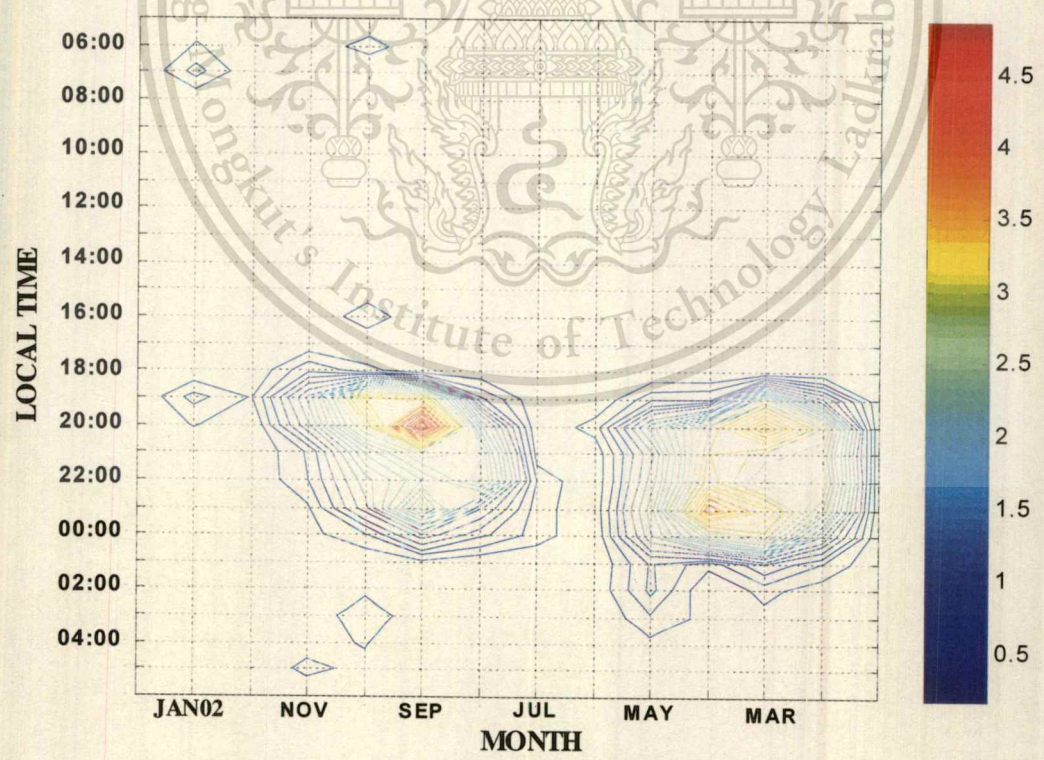
Fig. 3.5 Diurnal and seasonal variation of scintillation occurrences
(Feb. 2000-Jan. 2001)

This material is reserved for educational use only, not allowed for commercial use.

Forbidden to modify the content, and cite the document when use.



(a) Three dimensional result



(b) Contour result projected from 3D result

Fig. 3.6 Diurnal and seasonal variation of scintillation occurrences

(Feb. 2001-Jan. 2002)
 This material is intended for educational use only, not allowed for commercial use.
 Forbidden to modify the content, and cite the document when use.

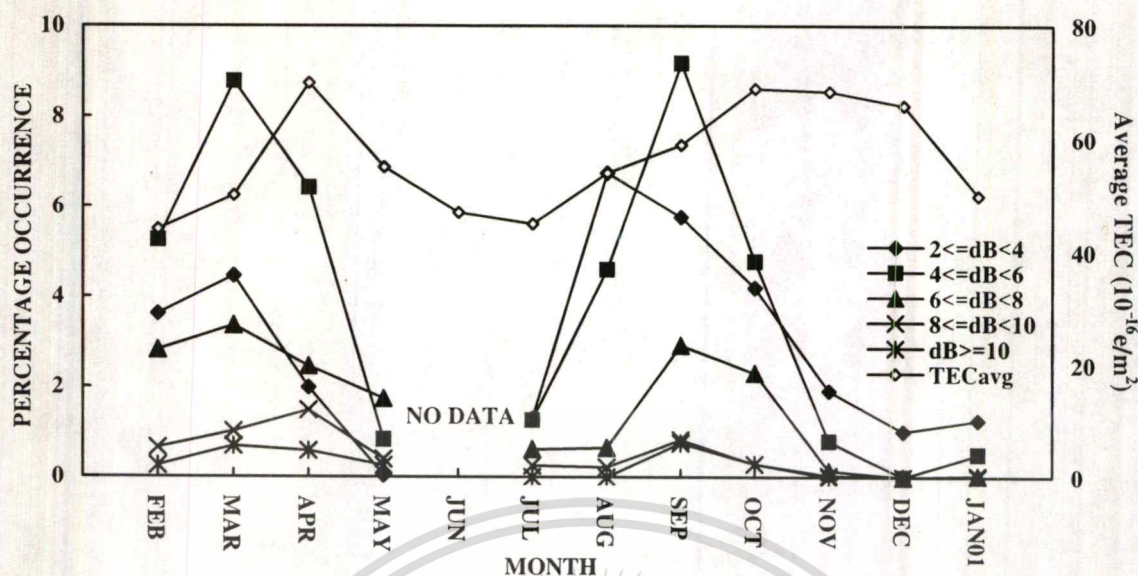
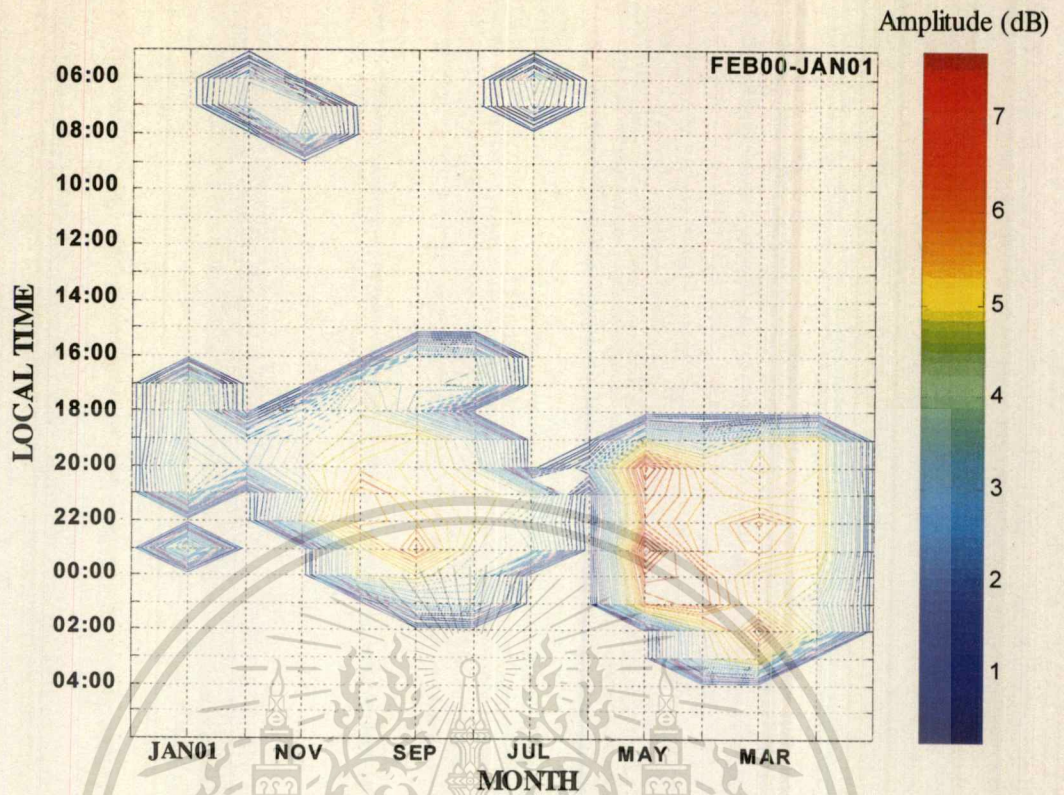


Fig. 3.7 Comparison of seasonal variation of scintillation and average TEC in 2000

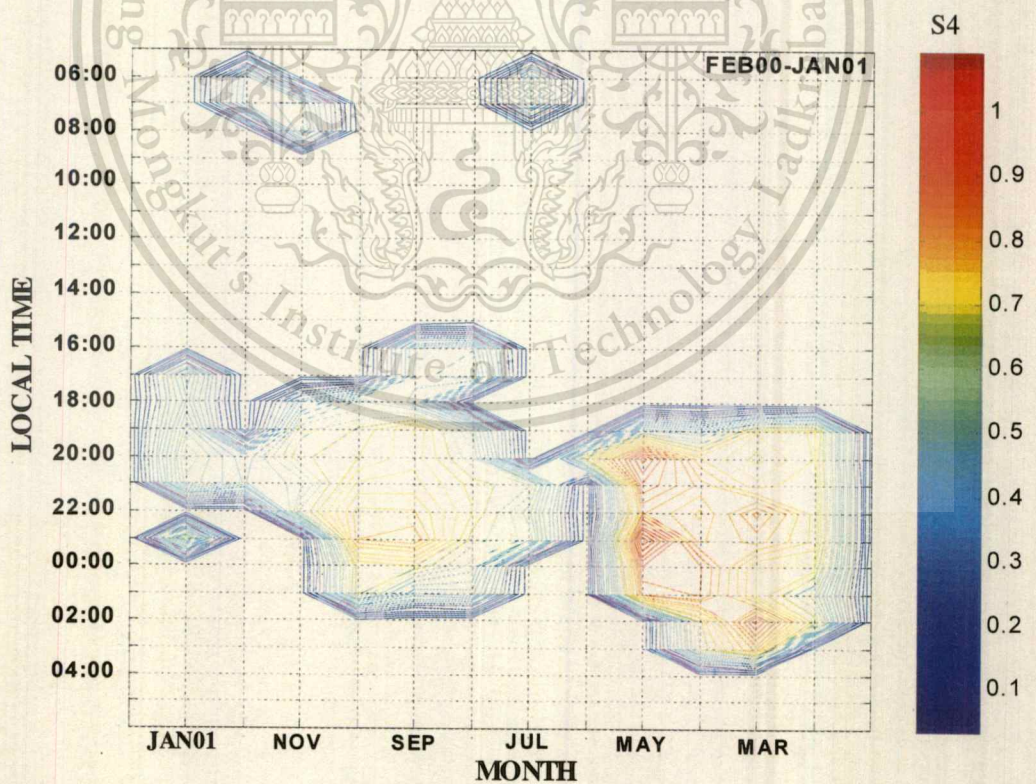
intensity during each local time and months consequently, the classification of scintillation intensity in detail should be considered as shown in Fig. 3.10 (a) and (b). From Fig. 3.8, although the higher scintillation intensity events were also observed in May, but the percentage occurrence of these events were small when considering each amplitude fluctuation levels in Fig. 3.10 (a). Also in January 2002, the percentages of higher scintillation events were very small when comparing with ones in March or September 2001. Table 3.2 describes the maximum amplitude fluctuation values of each months and their times' occurrences. From Fig. 3.8 – 3.9 and Table 3.2, the obtained results have shown that high intensity of scintillation usually occurred during 20.00–23.00 LT and 01.00–02.00 LT; and occurred seasonally in March – April and September – October.

According to Chapter 2, ionospheric scintillation depends on the solar activity and sunspot numbers. The relation between sunspot numbers of this 23rd maximum solar cycle (Year 2000) and scintillation occurrences are shown in Fig. 3.11. There was some relation between sunspot numbers variation and monthly scintillation occurrences. The variation of sunspot numbers in February – April 2000, February – April 2001 and August – October 2001 had the good agreement with the scintillation occurrence characteristics during those periods. The intensity and occurrence numbers of scintillation in 2000 period were higher than ones in 2001, this corresponded to the higher solar activity occurring in 2000. However, for the good results of solar activity and sunspot numbers dependence, scintillation observation should be done for many

This material is reserved for educational use only, not allowed for commercial use.



(a) Average amplitude fluctuation

(b) Average S_4 index**Fig. 3.8** Average intensity of all scintillation events in Feb. 2000-Jan. 2001

This material is reserved for educational use only, not allowed for commercial use.

Forbidden to modify the content, and cite the document when use.

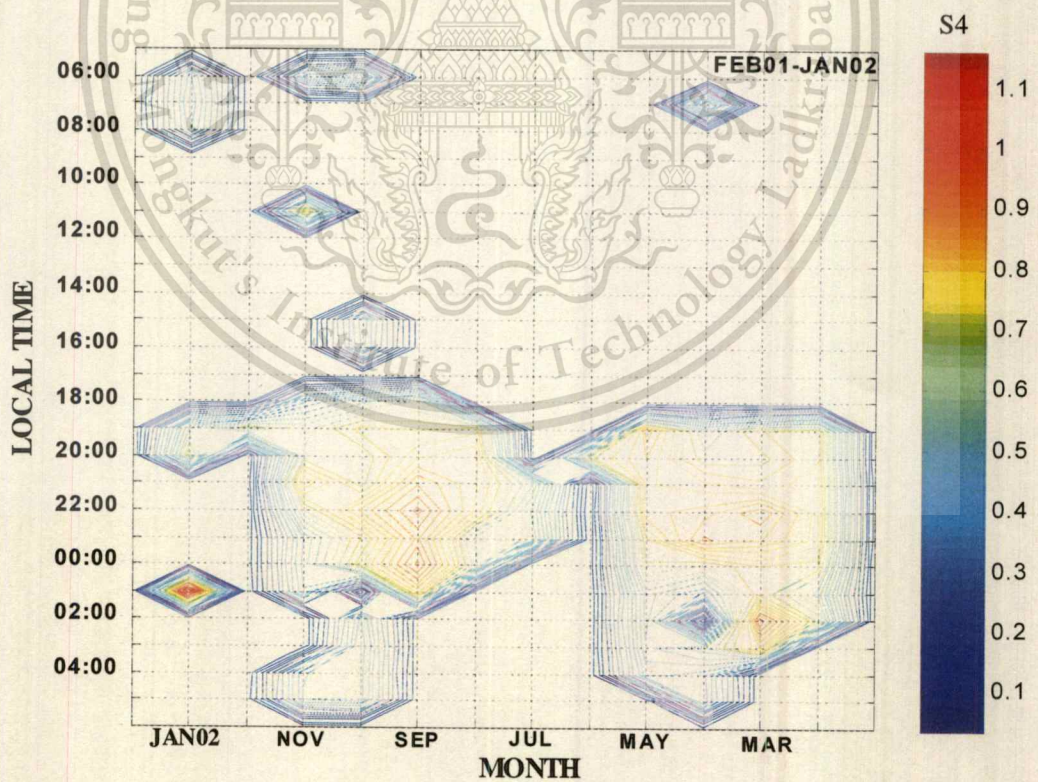
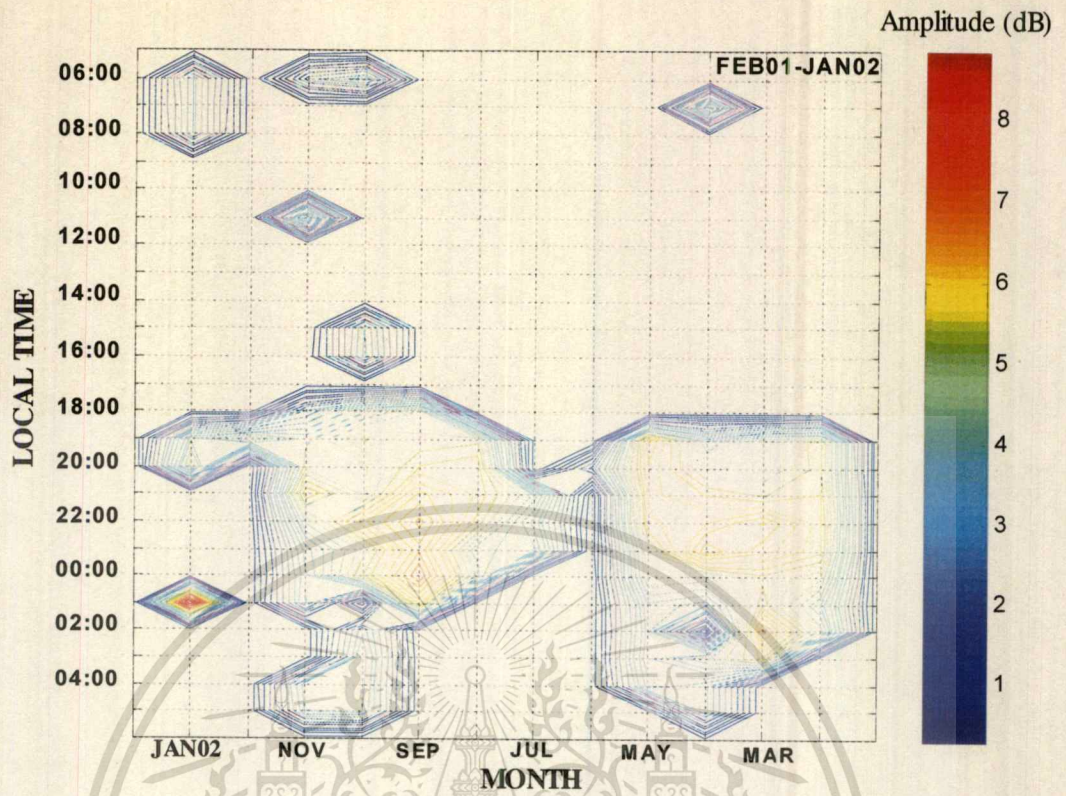
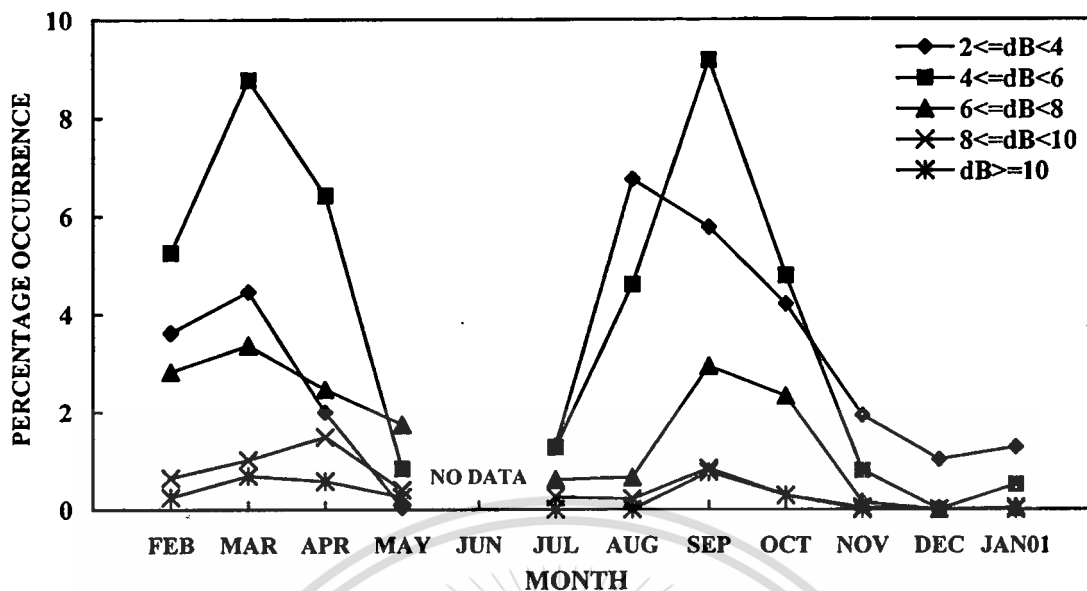


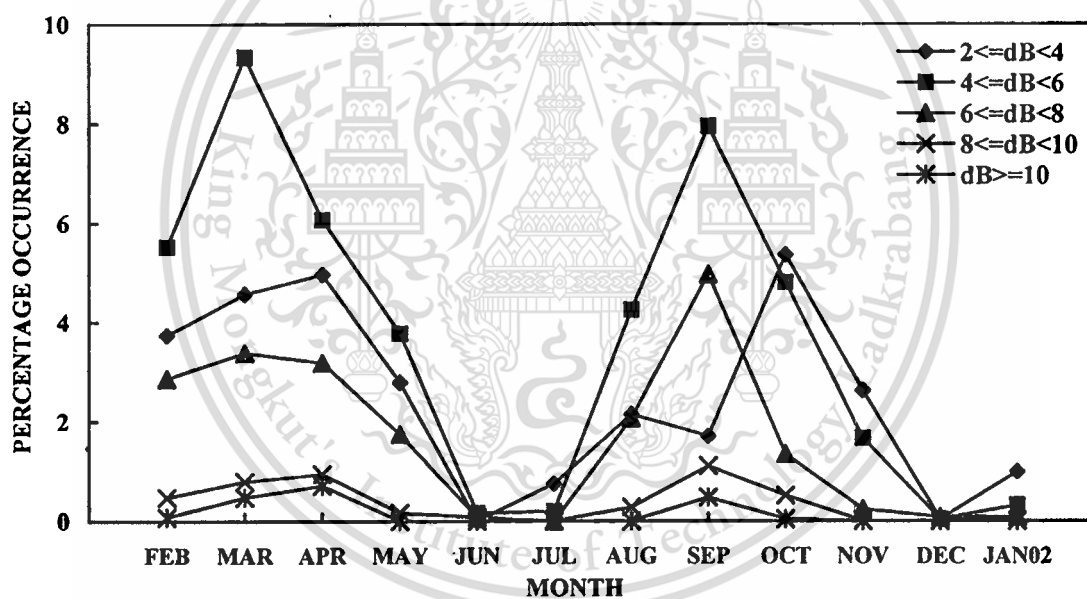
Fig. 3.9 Average intensity of all scintillation events in Feb. 2001-Jan. 2002

This material is reserved for educational use only, not allowed for commercial use.

Forbidden to modify the content, and cite the document when use.



(a)



(b)

Fig. 3.10 Classification of amplitude level scintillation in each months

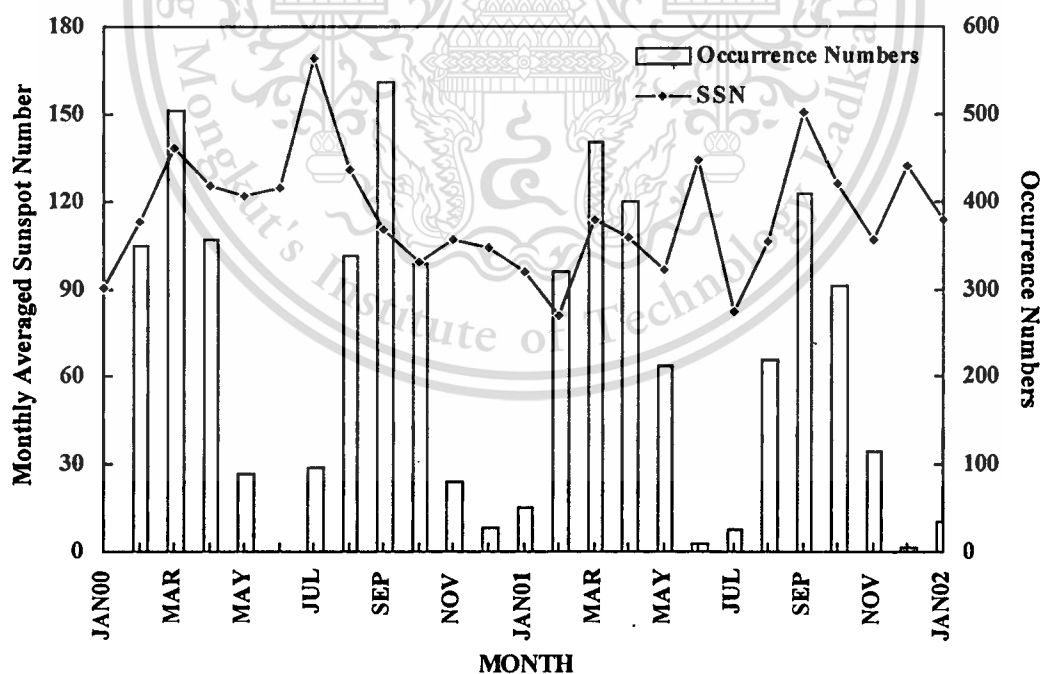
years at least one solar cycle, 11 years, such as (Basu *et.al.* 1988 ; Dabas *et.al.* 1991). Therefore the scintillation intensity and occurrence numbers depending on the solar activity variations can be observed clearly, especially the results in solar maximum and minimum periods. From the previous results, monthly scintillation variations are shown as the results in 4 periods for one-year observation. Two high scintillation intensity periods during February – April and August – October, and two low scintillation intensity periods during May – July and November – January, these can

This material is reserved for educational use only, not allowed for commercial use.

Forbidden to modify the content, and cite the document when use.

Table 3.2 Maximum levels of amplitude scintillation

MONTH	Amplitude Fluctuation (dB _{P-P}) / Local Time	
	FEB00 – JAN01	FEB01 – JAN02
February	13.04 dB / 22:10 LT	13.34 dB / 21:25 LT
March	17.02 dB / 22:45 LT	15.7 dB / 22:55 LT
April	18.03 dB / 01:04 LT	16.37 dB / 23:25 LT
May	11.42 dB / 20:39 LT	8.49 dB / 20:35 LT
June	-	8.32 dB / 20:16 LT
July	5.52 dB / 21:18 LT	4.87 dB / 21:55 LT
August	9.92 dB / 00:10 LT	9.18 dB / 20:40 LT
September	14.77 dB / 21:55 LT	13.84 dB / 00:00 LT
October	17.28 dB / 23:35 LT	14.29 dB / 22:20 LT
November	9.15 dB / 20:00 LT	7.1 dB / 20:25 LT
December	3.08 dB / 21:00 LT	6.64 dB / 19:22 LT
January	8.12 dB / 20:25 LT	9.16 dB / 01:45 LT

**Fig. 3.11** Monthly comparison of scintillation occurrences and sunspot numbers

be concluded particularly for this station. In the following chapter, in order to study the irregularities and statistical analysis of scintillation, these four periods' characteristics have been considered individually.

3.2.3 Scintillation Characteristics in case of Different Latitudinal Position

The difference between the observation stations causes the different characteristics of scintillation depending on the geomagnetic latitude. Allnutt (1989 : 81) described that the gigahertz ionospheric scintillation of any significant amplitude only occurs within approximately $\pm 30^\circ$ of the geomagnetic equator for geostationary communications satellite links. In this study, the morphology of ionospheric scintillation at 1.694 GHz observed at different locations, KMITL and CMU, are described. KMITL is at the location of 2.8° N geomagnetic latitude; and CMU is at the location of 7.9° N geomagnetic latitude. According to the data base access for CMU station, 0.1 Hz median data, from its 50 Hz original data, were used to analyze and compare with KMITL results. This study observed scintillation events for one year, February 2000 to January 2001. Fig. 3.12 shows the comparison of average density of total electron content observed at each station in 2000. After sunset time, the density of electron content occurred the nighttime enhancement due to the westward electrojet (Appendix A). The densities of daytime electron content of both station were nearly same with each other; but in the evening, the enhancement of electron content at CMU was higher, and fluctuated until it decreased. Furthermore, the geomagnetic latitude position of CMU is closer to the equatorial anomaly (See Appendix A) at $\pm 15^\circ$ geomagnetic latitude than KMITL position. Additionally, according to contours of scintillation intensity as shown

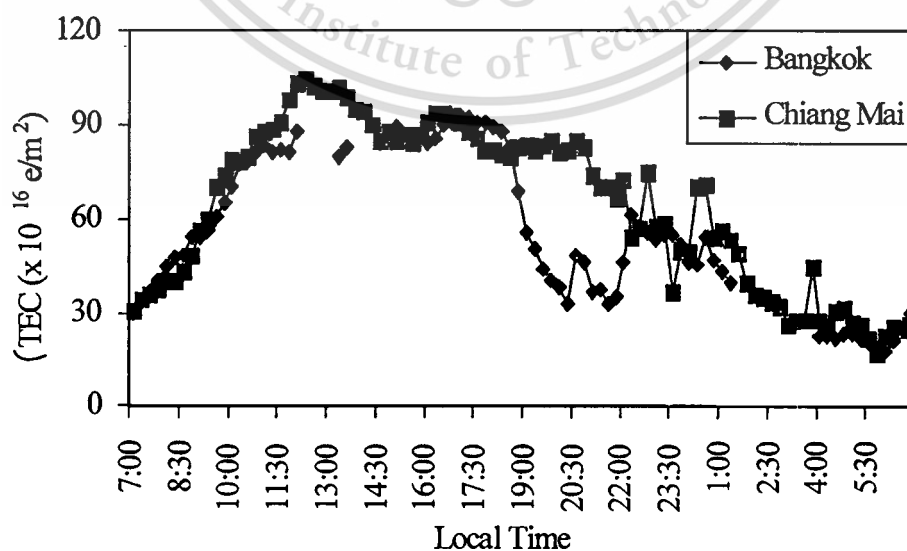
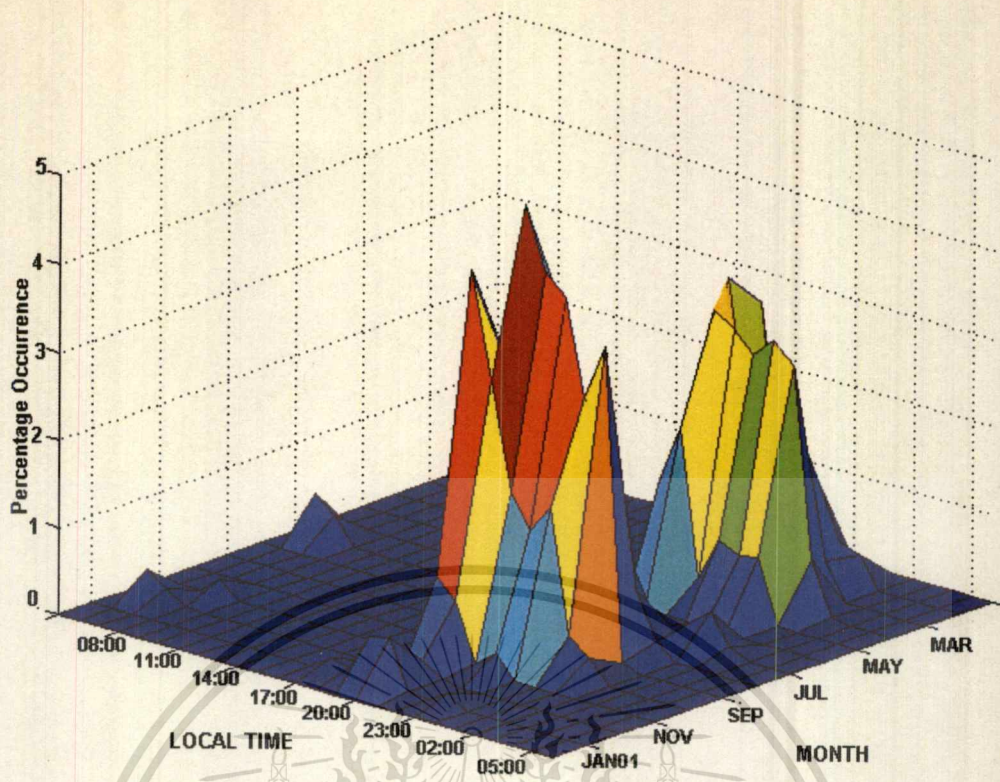


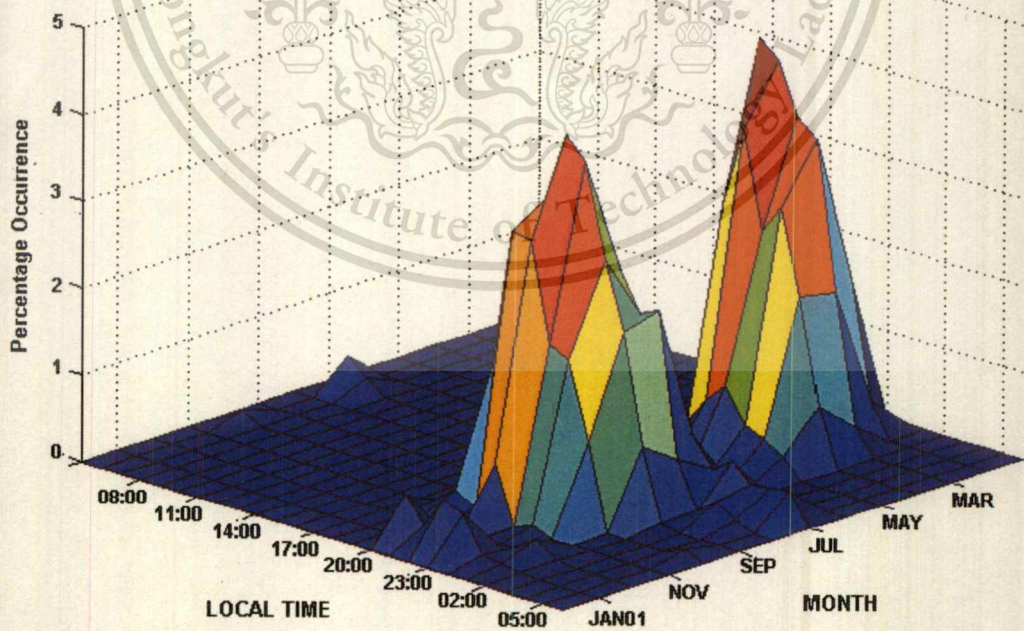
Fig. 3.12 Average total electron content measured at both stations in 2000

This material is reserved for educational use only, not allowed for commercial use.

Forbidden to modify the content, and cite the document when use.



(a) KMITL, Bangkok station

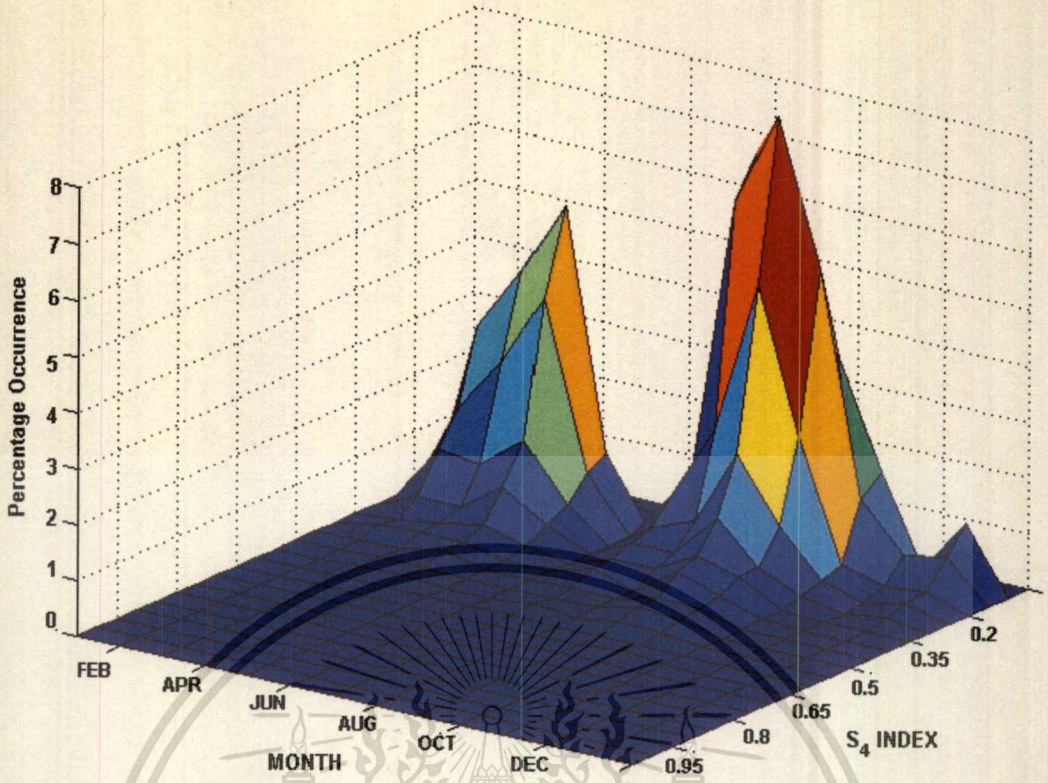


(b) CMU, Chiang Mai station

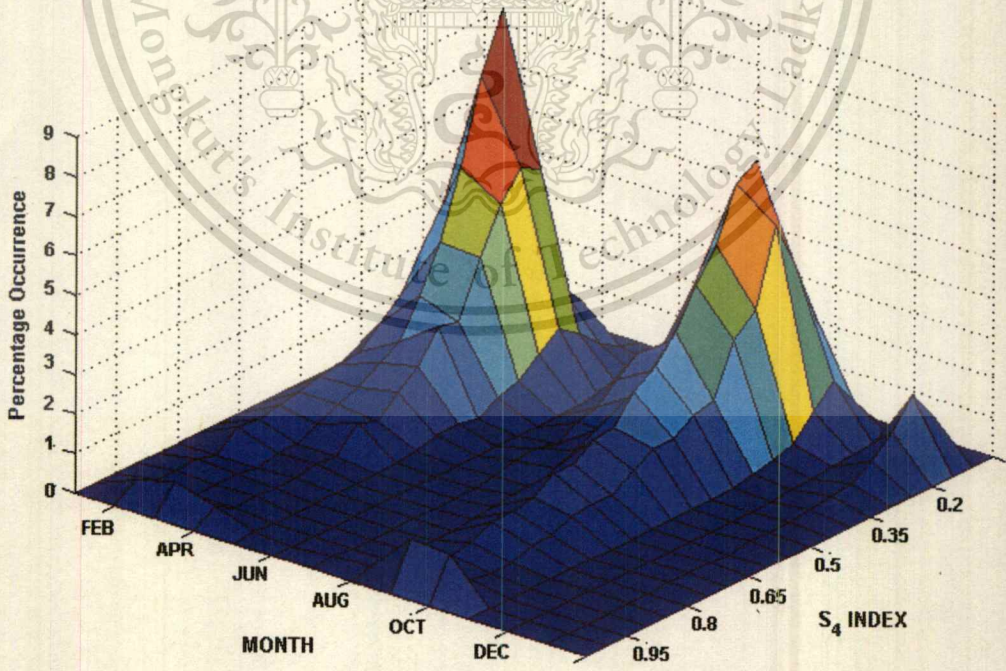
Fig. 3.13 Diurnal and seasonal variation of scintillation (Feb. 2000 – Jan. 2001)

This material is reserved for educational use only, not allowed for commercial use.

Forbidden to modify the content, and cite the document when use.



(a) KMITL, Bangkok station

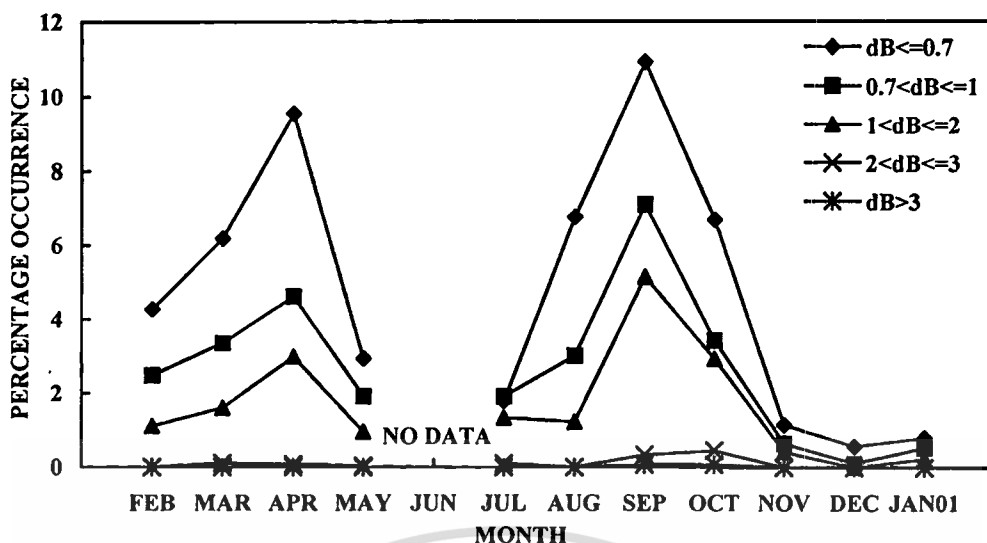


(b) CMU, Chiang Mai station

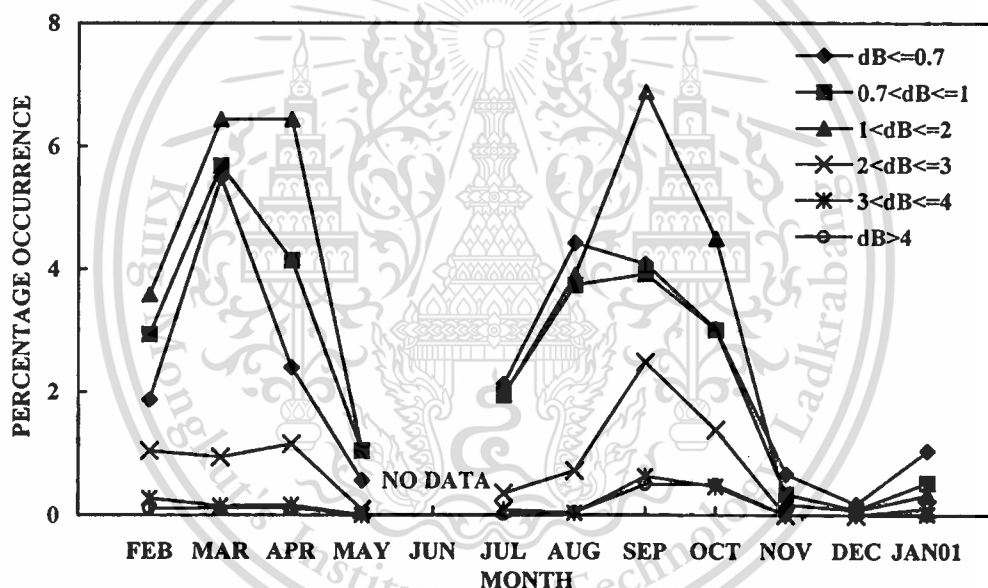
Fig. 3.14 S_4 index distribution (Feb.2000 – Jan. 2001)

This material is reserved for educational use only, not allowed for commercial use.

Forbidden to modify the content, and cite the document when use.



(a) KMITL, Bangkok station



(b) CMU, Chiang Mai station

Fig. 3.15 Classification of amplitude level scintillation (Feb. 2000 – Jan. 2001)

shown in Fig. 2.5, higher scintillation intensity can be observed between equatorial anomaly region where closer to the CMU geomagnetic position. These can be assumed to be the causes of higher scintillation intensity occurring at CMU observation station than KMITL station.

Fig. 3.13 and 3.14 present the diurnal and seasonal variation of scintillation occurrences, and S_4 index intensity respectively for both stations. For the diurnal variation, the time when scintillation usually occurred was around 19.00-02.00 LT. In

This material is reserved for educational use only, not allowed for commercial use.

Forbidden to modify the content, and cite the document when use.

some events, especially in July and December, scintillation occurred exceedingly after that period until morning of the next day. These were due to the scintillation caused by electrojet irregularities. Considering seasonal variation, the percentage occurrences of scintillation at KMITL were maximum in April after that they grew decreasingly and reached maximum again in September. On the other hand, at CMU station, the scintillation occurrences were maximum in March and September corresponding to the seasonal variation of vernal and autumnal equinox respectively. In June, there was not any scintillation analysis at both stations due to receiver system broke down. Figure 3.14 (a) and (b) describe about the intensity of scintillation index S_4 . The high levels of S_4 index distributed continuously as observed at CMU station. The S_4 levels were between 0.15 to 1. On the contrary for KMITL station, the intensity levels of S_4 did not exceed 0.6. These can indicate that there were many stronger scintillation events occurring at CMU more than at KMITL station corresponding to the geomagnetic latitude dependence as discussed previously.

According to the results in Fig. 3.15, the monthly variations of all levels were similar. When comparing the amplitude scintillation levels of both stations, the results clearly shown that ionospheric scintillation occurring at CMU had stronger scintillation intensity more than KMITL. The high amplitude fluctuation levels between 2 to 4 dB could be observed, and the signals usually fluctuated between 1 to 2 dB as observed at CMU station. On the other hand, the high fluctuation levels, exceeded 4 dB, was rarely observed; and the amplitude signals generally fluctuated less than 1 dB at BKK station. From Fig. 3.15 (a), most fluctuation levels were maximum in April and September; and in March and September for CMU station. Moreover, small percentage occurrences of higher fluctuation levels, $2 < \text{dB} \leq 3$ and $3 < \text{dB} \leq 4$, were observed in April and February respectively.

Nevertheless, this section presents the scintillation characteristics between two different locations, then some parameters and scintillation data should be used similarly between these two stations. Scintillation data used to analyze for this study were different when comparing with Section 3.2.2 that characterize only KMITL station individually. This causes the different scintillation characteristics between two sections for KMITL station, such as seasonal variation, occurrence numbers and amplitude fluctuation levels that the intensity is less than characterization using 5 Hz scintillation data as presented in Section 3.2.2.

This material is reserved for educational use only, not allowed for commercial use.

Forbidden to modify the content, and cite the document when use.

3.3 Conclusion

Based on morphological characteristics of ionospheric scintillation observed at both stations, the diurnal and seasonal variation of scintillation characteristics seemed to be the same. This nighttime scintillation usually occurred at 18.00-02.00 LT. Some events continued occurring after this time until daytime of the next day. These might be due to the scintillation effected by daytime electrojet irregularities. For KMITL station, scintillation mostly occurred at 20.00-21.00 LT in the maximum solar cycle year especially in March and September. On the contrary, in 2001 scintillation occurrences mostly appeared at 20.00 LT in September, but for the first equinox period, scintillation could be observed obviously at 20.00 and 23.00 LT not frequently as occurred in September. Seasonal variation could be observed clearly, and had the good relation with the average TEC and solar activity in vernal and autumnal equinox periods, March and September. Fig. 3.8 and 3.9 present the average intensity occurring hourly in each month. Some high scintillation intensity events could be observed here in May 2000 and January 2002. However, these results are hourly averaged values for each month; if consider scintillation intensity in each fluctuating levels, the good agreement of high intensity levels varying seasonally can be obtained.

The results of geomagnetic latitude dependence were described in Section 3.2.3. The location of CMU station is closer to the equatorial anomaly than KMITL location. Consequently, the higher scintillation intensity events and more scintillation occurrences could be observed in this station.

This chapter presents only morphological scintillation characteristics, then for the relation between scintillation characteristics and ionospheric irregularities will be presented in the next chapter.

CHAPTER 4

INSTANTANEOUS ANALYSIS OF FREQUENCY-TIME SCINTILLATION STRUCTURES

Since ionospheric scintillation has been believed that is caused by relative stationary irregularities moving perpendicularly to the radiowave path, the spatial and temporal frequency and time scintillation structures are related by these drift velocities. The actual relationship depends on the irregularities' composition (power spectra and decorrelation time) and other physical factors. The previous chapter presented only the magnitude variation of scintillation; however in order to study the effect of irregularities on satellite signal, the frequency and time structure of scintillating signals should be considered. All two years scintillation events at KMITL station were analyzed by using 5 Hz re-sampled signal data. Each scintillation events were divided to many 5-7 minutes sections depending on fluctuating period of individual events. All data sections were used to determine the frequency and time structure of scintillation by power spectral density and autocorrelation analysis respectively.

The power spectral density (PSD) of the signal characterizes the distribution of the signal's power in the frequency domain. If a real-valued power signal is a periodic signal, $x(t)$, with period T_0 , the expression for the average power of a periodic signal where the time average is taken over the signal period T_0 can be given by (Sklar. 1988).

$$P_x = \frac{1}{T_0} \int_{-T_0/2}^{T_0/2} x^2(t) dt \quad (4.1)$$

Using Parseval's theorem, the power of such signal expressed in time domain can be related to the power expressed in frequency domain, as follows:

$$P_x = \frac{1}{T_0} \int_{-T_0/2}^{T_0/2} x^2(t) dt = \sum_{n=-\infty}^{\infty} |c_n|^2 \quad (4.2)$$

This material is reserved for educational use only, not allowed for commercial use.

Forbidden to modify the content, and cite the document when use.

where $|c_n|$ terms are the complex Fourier series coefficients of the periodic signal. Only the magnitude of these coefficients should be considered.

The power spectral density function $G_x(f)$ of periodic signal, $x(t)$, is a real, even, and nonnegative function of frequency that gives the distribution of the power of $x(t)$ in the frequency domain, defined as

$$G_x(f) = \sum_{n=-\infty}^{\infty} |c_n|^2 \delta(f - nf_0) \quad (4.3)$$

This means that all powers are concentrated at the harmonics of the fundamental frequency, and the power at the n th harmonic (nf_0) is $|c_n|^2$, that is magnitude square of the corresponding Fourier series coefficient. $G_x(f)$ defines the power spectral density as a succession of the weighted delta functions. Therefore, the PSD of the periodic signal is the discrete function of frequency. If $x(t)$ is the nonperiodic signal, it can not be expressed by Fourier series; and if it is the nonperiodic power signal, it may not have the Fourier transform. However, if forming a truncated version, $x_T(t)$, of the nonperiodic power signal, $x(t)$, by observing only interval $(-T/2, T/2)$, then $x_T(t)$ has finite energy and a proper Fourier transform, $X_T(f)$. Therefore, the power spectral density of the nonperiodic signal $x(t)$ can be defined in the limit as

$$G_x(f) = \lim_{T \rightarrow \infty} \frac{1}{T} |X_T(f)|^2 \quad (4.4)$$

Autocorrelation, $R_x(\tau)$, provides a measure of how closely the signal matches a copy of itself as the copy is shifted τ units in time. This is not a function of time; it is only a function of the time difference, τ , between the waveform and its shifted copy. The autocorrelation function of a real-valued periodic power signal, $x(t)$, with a single period T_0 can be expressed as

$$R_x(\tau) = \frac{1}{T_0} \int_{-T_0/2}^{T_0/2} x(t)x(t+\tau)dt \quad \text{for } -\infty < \tau < \infty \quad (4.5)$$

This material is reserved for educational use only, not allowed for commercial use.

Forbidden to modify the content, and cite the document when use.

The autocorrelation function and power spectral density function form a Fourier transform pair, $R_x(\tau) \leftrightarrow G_x(f)$:

$$G_x(f) = F (R_x(\tau)) \quad (4.6)$$

4.1 Power Spectrum Analysis of Scintillation Signal

4.1.1 Temporal Scintillation Analysis

The power spectrum of scintillation event contains the information about the spectral content of irregularities when the satellite signals propagate through them. The study of the power spectrum is useful for identifying parameters such as scale sizes, elongation, and drift speeds of the irregularities that help to determine the physical origin of scintillation. All scintillation sections were analyzed by Fast Fourier Transform (FFT) to determine the PSD of those scintillation events.

The power spectral density of the scintillation event is consisting of a relatively flat low frequency portion, a high frequency roll-off and a noise floor. The transition between the low frequency, or flat up portion, and the high frequency roll-off portion of spectrum is defined as the “ Fresnel frequency ” or “ corner frequency ”. The high frequency roll-off portion is assumed to have the close relation to the irregularities spectrum. It contains the important information about the structure of the irregularities. The spectrum starts to roll-off in the neighborhood of the Fresnel frequency that defined as the ratio of the velocity of the irregularities transverse to the satellite signal path, as given by Equation (4.7) (Banerjee *et.al.* 1992). This Fresnel frequency has the same value as the first Fresnel minimum frequency as described in Equation (2.4). Allnutt (1989 : 79) has described that the first Fresnel minimum, which is the inverse of the coherence time (see Section 4.2) can cause the roll-off portion to appear steeply than it actually is.

$$f_F = \frac{\nu}{\sqrt{\lambda z}} \quad (4.7)$$

where ν is the mean drift velocity of the irregularities medium transverse to the propagation path. λ is the wavelength of signal and z is the mean height of the irregularities. Figure 4.1 describes the power spectral density of scintillation events

occurred on 21 March 2001, 19 September, and 22 September 2000. These instantaneous spectrum behaviors were analyzed over 5 minutes, and the Fresnel frequency, spectral slope and noise floor starting frequency can be observed for each log-log plot spectrum.

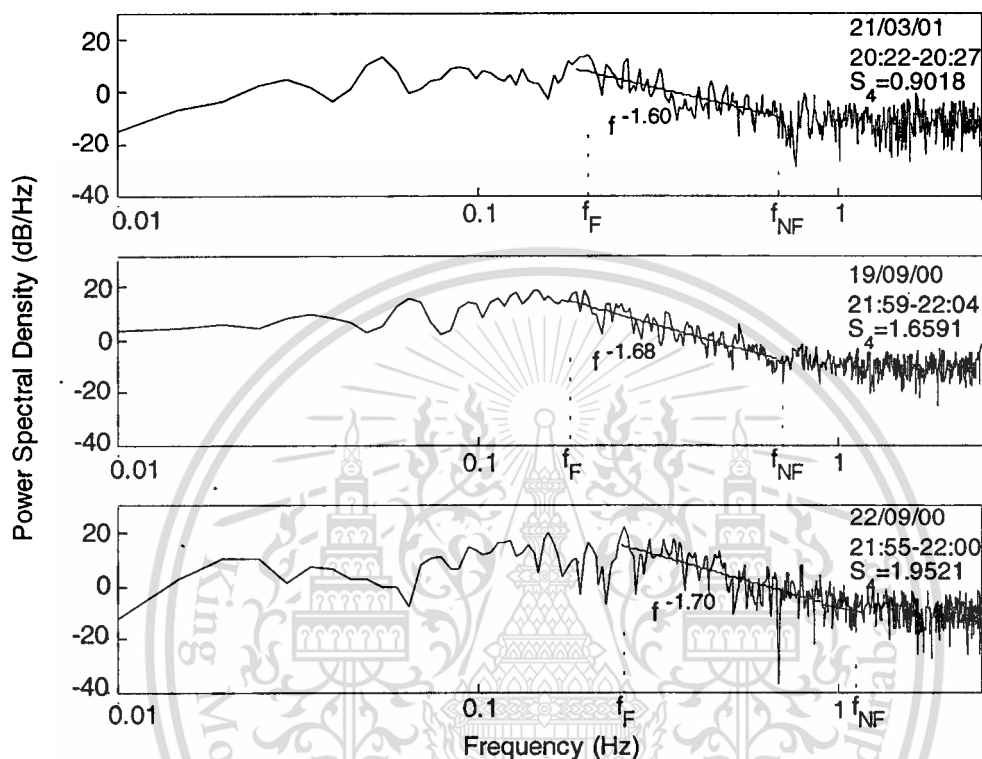


Fig. 4.1 Power spectral density of scintillation signals

Table 4.1 Parameters of scintillation power spectral density

Scintillation Event	S_4 Index	Spectral Slope	Spectral Index	Fresnel Frequency, f_F	Noise Floor Starting Frequency, f_{NF}
21/03/01	0.90	-3.40	1.60	198.3 mHz	0.743 Hz
19/09/00	1.66	-3.74	1.68	141.2 mHz	0.731 Hz
22/09/00	1.95	-3.80	1.70	251.7 mHz	1.142 Hz

Taking least square log linear fitting over the high frequency roll of part can derive the slope of power spectral density, ν , or high-frequency asymptote, or power index of the power spectrum throughout the whole frequency range, limited only data length. This high frequency slope is related to the power spectrum of the irregularities

This material is reserved for educational use only, not allowed for commercial use.

Forbidden to modify the content, and cite the document when use.

as followed.

$$p = 1 - \nu \quad (4.8)$$

where p is the spectral index of irregularities spectrum.

Yeh and Liu (1982) have proposed the frequency dependence of S_4 index related to the power spectrum of the irregularities as given by

$$S_4 \propto f^{-n} \quad (4.9)$$

where $n = (p + 2)/4$

therefore

$$S_4 \propto f^{-(p+2)/4} \propto f^{-(3-\nu)/4} \quad (4.10)$$

According to the result in Fig. 4.1, spectral slopes of these three events are $\nu = -3.40, -3.74$ and -3.80 respectively. The spectral index of scintillation signals have been calculated using Equation (4.10), hence these spectral index, n , are 1.6., 1.68 and 1.70 respectively. Other parameters of scintillating power spectral density of Fig. 4.1, such as, Fresnel frequency or noise floor starting frequency, are summarized in Table 4.1. The low frequency portion of spectrum can be either flat or increasing with frequency depending on whether the irregularities are isotropic in the plane transverse to the signal propagation (Singleton. 1974). The low frequency portion of 21/03/01 event is flatter than others that are gradually increasing with frequency; consequently, these can be assumed the isotropic condition of irregularities at 21/03/01 event, but the others irregularities conditions might seem to be unstable. Furthermore, the relation between spectral slope and scintillation intensity can be obtained. The low value of spectral slope, ν , corresponds to the scintillation intensity as indicated by the low value of S_4 index. This means that the spectral slope increases in value when S_4 increases, and then the spectral index also increases. This relation can be described clearly in the next section that whole segments of scintillation events have been considered. The Fresnel frequency and noise floor starting frequencies do not related with the scintillation intensity individually. The bandwidth between Fresnel frequency

This material is reserved for educational use only, not allowed for commercial use.

Forbidden to modify the content, and cite the document when use.

and noise floor starting frequency corresponds inversely to the fluctuating rate of scintillating signals as will be described in Section 4.3.

4.1.2 Spectral Behavior of Scintillation

As is well known, the spectrum of the scintillation signal contains information about the spectral content of the irregularities. All two years events, 2756 and 2516 events, for scintillation spectra provided the ample database to study the diurnal and seasonal variation of the irregularities. All events have been analyzed power spectrum density, and determined the spectral slope (ν), spectral index (n), Fresnel frequency (f_F), and noise floor starting frequency (f_{NF}). The distribution characteristics of these parameters varying with time and S_4 index can be obtained here. Those can be used to assume the distribution of the irregularities. Figure 4.2 shows the diurnal variation of spectral slopes of two years scintillation events. Scintillation events have been divided to 4 groups, February – April, May – July, August – October, and November – January, corresponding to the intensity and occurrences as discussed in the previous chapter. Time series of each group correspond to scintillation time occurred for all events. The blue dots present the distribution of spectral slopes before midnight and the red ones present spectral slopes after midnight until daytime in the morning. From the results, spectral slopes gradually increase in value with time during 18.00-00.00. Some slopes continue increasing after midnight such as in February – April and May – July 2000. The steepness of spectral slope stops increasing and gradually grows to the opposite direction; or exists at that slope value continuously, after midnight or in daytime. These correspond to the movement of the irregularities that the postsunset irregularities move in the eastward direction and gradually decline in speed. After local midnight, these irregularities may halt movement and reverse direction. Then the westward irregularities gradually increase their velocity (Mollen *et.al.* 1988). This might seem to effect the variation of spectral slope. Furthermore, taking slope ν to determine spectral index, n , as described in Equation (4.8-4.10), and determining the variation of spectral index with local time can describe the characteristics of scintillation spectrum related to irregularities more obviously as the results in Fig. 4.3 and 4.4. All values of spectral index have been plotted against local time; similarly to Fig. 4.2, the blue and red dots present postsunset and after midnight spectral index respectively. Only spectral index distributions for postsunset time have been fitted by

This material is reserved for educational use only, not allowed for commercial use.

Forbidden to modify the content, and cite the document when use.

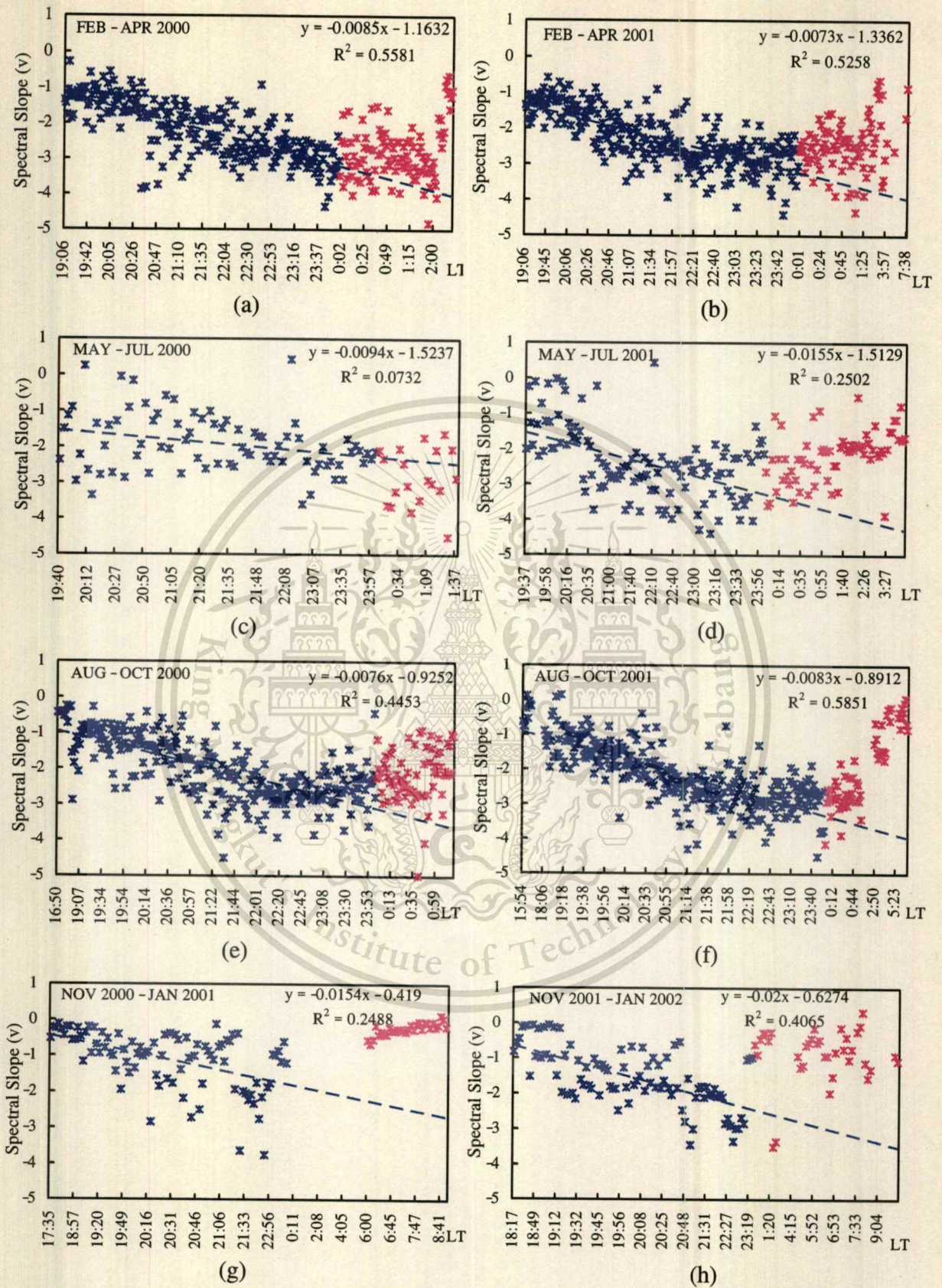
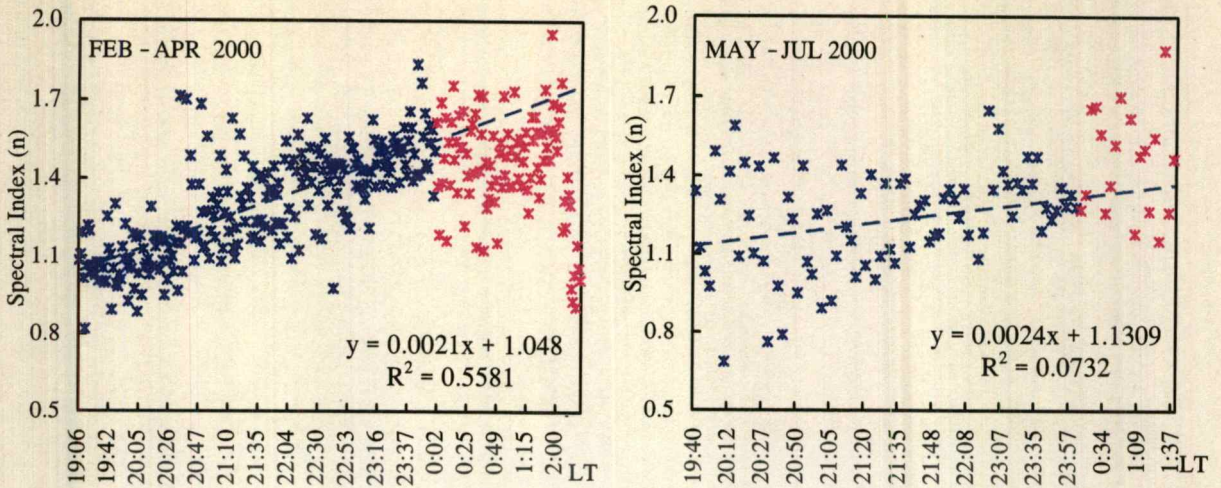


Fig. 4.2 Variation of scintillation's spectral slope versus local time (Feb. 2000-Jan. 2002)

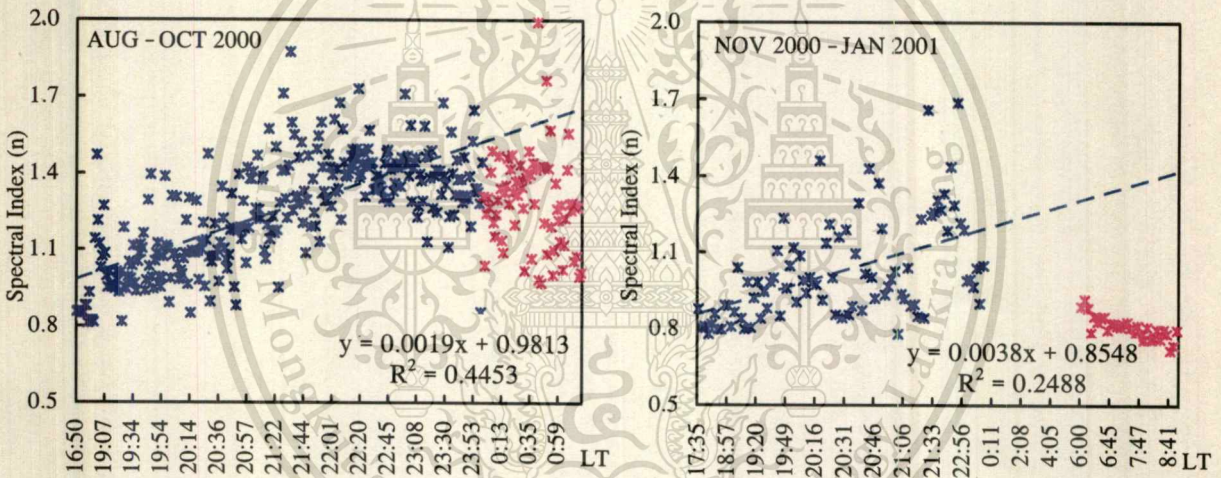
This material is reserved for educational use only, not allowed for commercial use.

Forbidden to modify the content, and cite the document when use.



(a) 1143 events 19.06 ~ 03.15 LT
 n : 0.82 ~ 1.95 v : -4.81 ~ -0.28
 S₄: 0.35 ~ 2.25

(b) 122 events 09.40 ~ 01.37 LT
 n : 0.64 ~ 2.04 v : -5.18 ~ 0.44
 S₄: 0.32 ~ 1.72



(c) 1202 events 16.50 ~ 01.42 LT
 n : 0.81 ~ 2.04 v : -6.71 ~ -0.25
 S₄: 0.31 ~ 2.12

(d) 159 events 17.35 ~ 08.53 LT
 n : 0.72 ~ 1.69 v : -3.75 ~ 0.13
 S₄: 0.34 ~ 1.2

Fig. 4.3 Variation of scintillation's spectral index versus local time during 2000

least square linear regression. Most of spectral index increase with time increasing before midnight; after that they become decreasingly or scatter randomly. According to Fig. 4.4 (c), Fig. 4.3 (a) and Fig. 4.4 (a), spectral index have the good linearity of data during 19.00 - 00.00 LT respectively. After midnight spectral index become decreasing rapidly in Aug.- Oct. 2001 and also Nov. 2001- Jan. 2002; but in Fig. 4.3 and 4.4 (a), the variations of spectral index do not change instantly but the index data are gradually scattering outwardly from the fitting line. These can be assumed that the

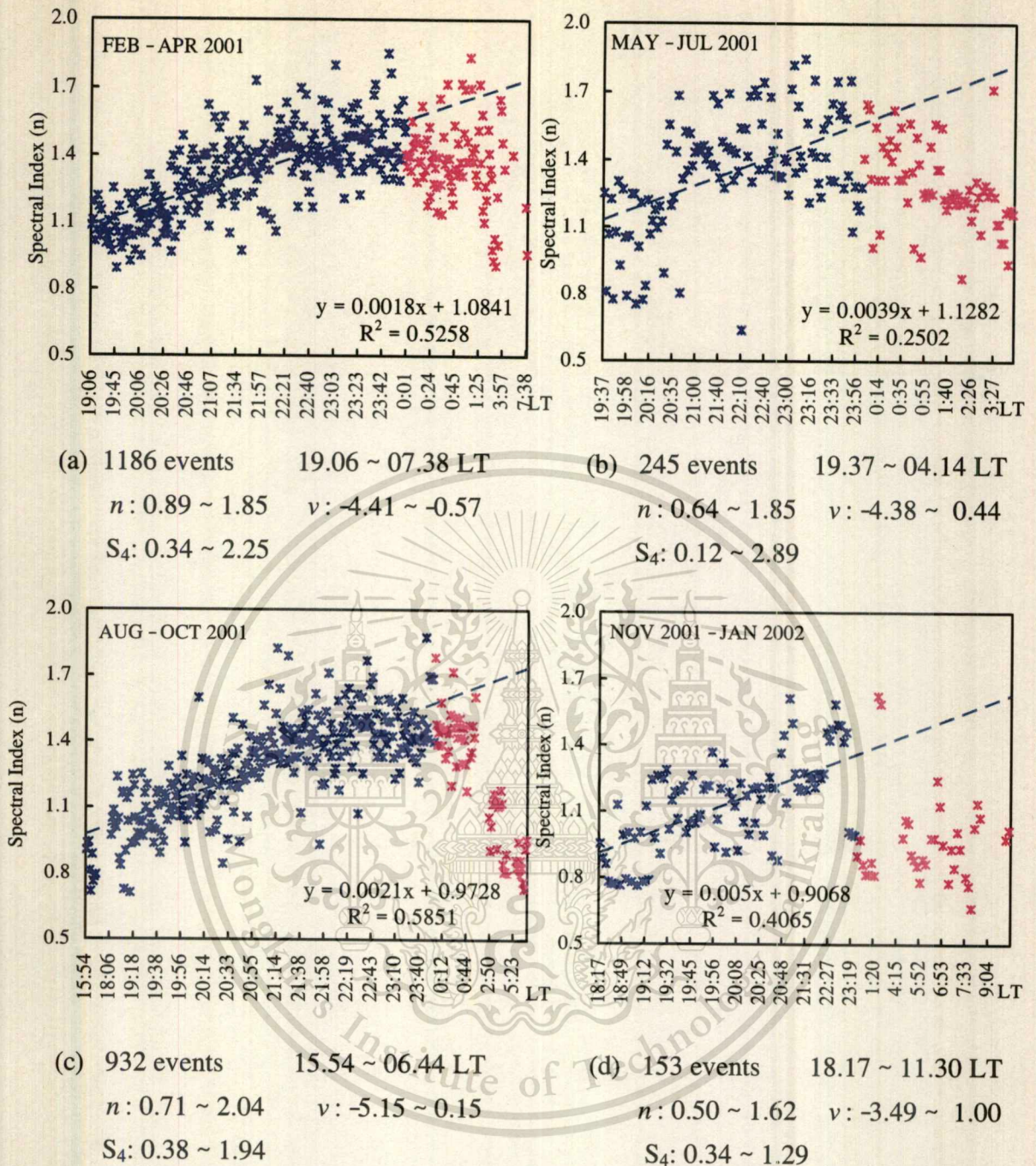


Fig. 4.4 Variation of scintillation's spectral index versus local time during 2001

irregularities movement changed immediately after midnight time in Aug. 2001 – Jan. 2002; on the contrary, in Feb. – Apr. 2000 and 2001, the irregularities halted, or, and then gradually changed the movement after midnight time. Fig. 4.3 (d) and 4.4 (d) show spectral index for daytime scintillation. As the results, the spectral index are very low comparing to the last condition's values in nighttime. These can indicate that although there was scintillation occurring in daytime, but the irregularities characteristics were different from others. These also mean the medium through that

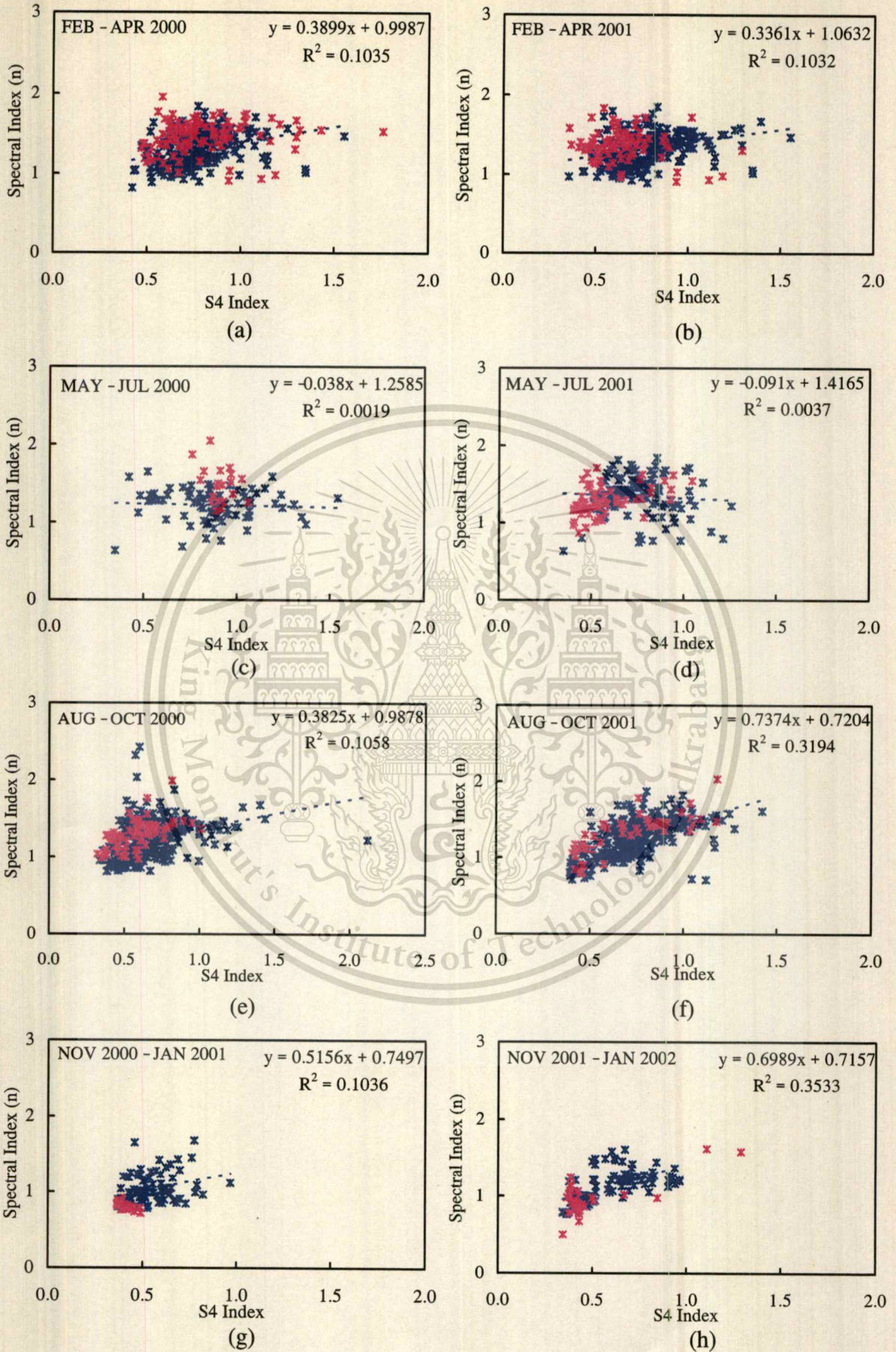


Fig. 4.5 Relation between spectral index and S_4 index (Feb. 2000-Jan. 2002)

satellite signals passed in daytime might be not the irregularities; consequently, or these fluctuating signal's events were not the ionospheric scintillation.

In view of the relationship between the temporal structure of scintillation and the spatial structure of ionospheric irregularities, the spectral index, n , of scintillation have been determined the variation based on the scintillation intensity by plotting values against the scintillation S_4 index. The small trends of increasing spectral index with increasing scintillation index are evident as the results in Fig. 4.5. The same scintillation groups have been analyzed similarly to the previous results. In Fig. 4.5 (c) and (d), the small relations between spectral index and S_4 index can be observed. The trend lines of both results are nearly zero slope or negative. This might seem to be the low intensity of irregularities and scintillation. Refer to Fig. 4.3 and Fig. 4.4 (d), low spectral index are observed in daytime (06.00~11.00 LT); furthermore when considering Fig. 4.5 (g) and (h), low values of spectral index corresponding to weak scintillation intensity are also observed. These results can be mentioned that the rapid fluctuated signals occurred during these periods may be not related with the ionospheric irregularities. In addition, from the relation of $S_4 \propto f^{-n}$ as given by Equation (4.9) and the above results, we can note that the spectral index, n , is not a constant any more; it depends on S_4 . The meaning of f^{-n} mentions that for the same ionospheric condition, the spectral index curves are different for different frequencies. This is due to the fact that at different frequencies the degrees of S_4 saturation are also different (Yeh and Liu. 1982).

Figure (4.6) and (4.7) present the Fresnel frequency and noise floor starting frequency varying with local time. These frequencies are the frequency components of signal fluctuation. Scintillating signals fluctuate randomly therefore many fluctuating frequencies components exist. The frequency ranges between these two frequencies have the rapid power dissipation. From the results, the variations in time of both frequencies are the same. Both Fresnel and noise floor frequencies increase gradually and generally approach the maximum around 21.00 and 22.00 LT; then frequencies start to decrease continuously until after midnight time. However, there are some results of events in May.-Jul. 2000 and Nov.-Jan. 2001, 2002 differently from the above mentions. Nevertheless, the values of Fresnel frequency and the noise floor frequency are not much meaningful than their frequency bandwidth; that can indicate the fluctuation rates of signal. This will be described again in Section 4.3.

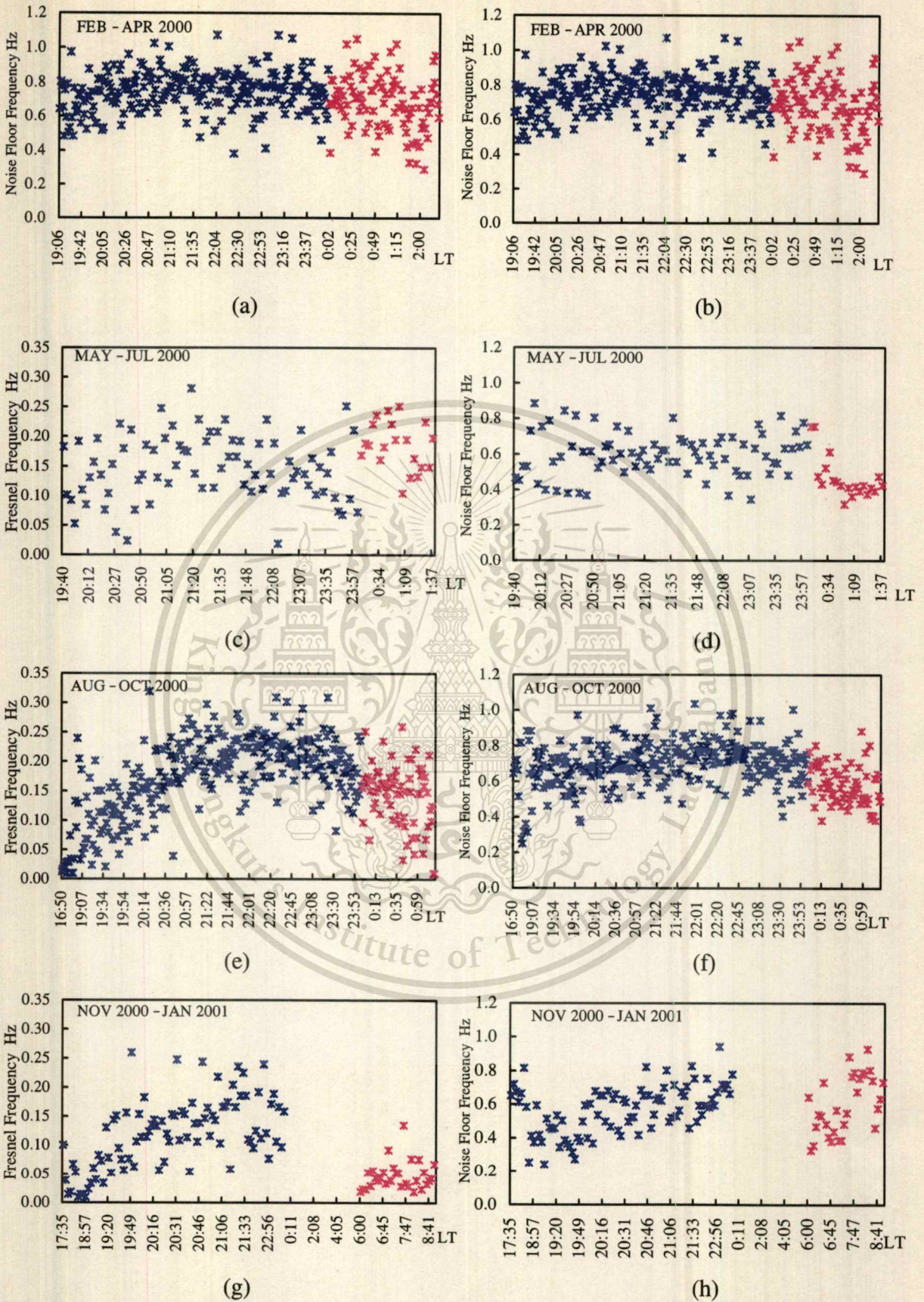


Fig. 4.6 Variation of Fresnel frequency and noise floor frequency versus local time (Feb. 2000 – Jan. 2001)

This material is for personal educational use only, not allowed for commercial use.

Forbidden to modify the content, and cite the document when use.

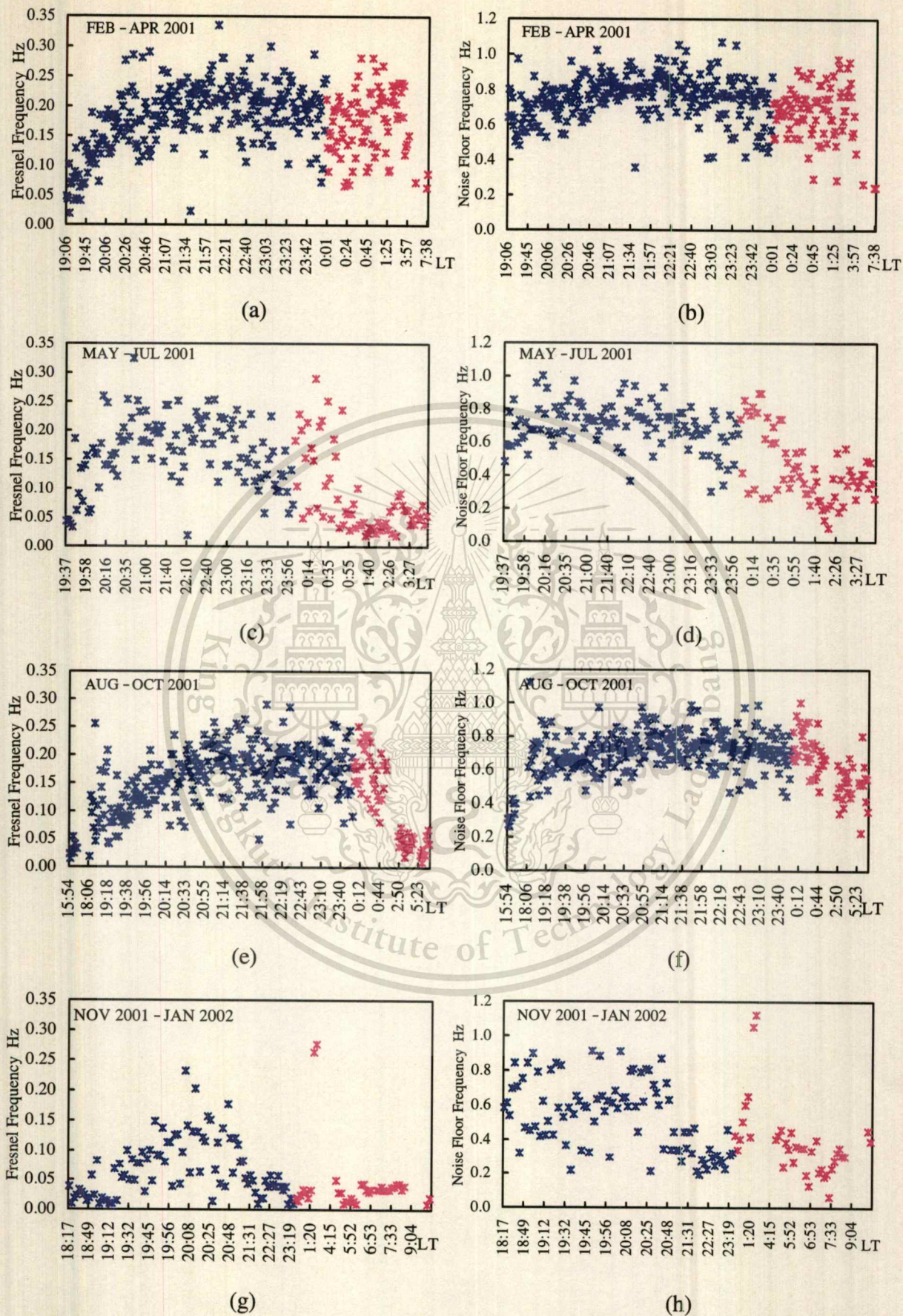


Fig. 4.7 Variation of Fresnel frequency and noise floor frequency versus local time

(Feb. 2001 – Jan. 2002)

Forbidden to modify the content, and cite the document when use.

4.2 Autocorrelation Analysis of Scintillation Signal

The autocorrelation analysis is another method of characterizing scintillation fading. It is also an effective mean of achieving time diversity improvement. Calculation of the autocorrelation of digitized scintillation data can establish a correlation interval or coherent time or decorrelation time, τ . The quantity τ is defined as the time lag for which the level of correlation decreases to 50% of its maximum value. Yeh and Liu (1982) have proposed that this decorrelation time depends on two factors; the Fresnel zone size, $\sqrt{\lambda(z-l/2)}$, as defined in Equation (2.6b), where λ is the wavelength of the signal and z is the mean distance of propagation path between ionospheric irregularities layer (thickness $\approx l$) and the receiver. Another factor is the drift speed of the irregularities transverse to the propagation path of the satellite signal. This decorrelation time is caused by multiple scattering of the satellite signal from the irregularities. The most dominant contributions to strong scintillation come from the irregularities that scale sizes approximately equal to the dimension of the first Fresnel zone. Therefore, the decorrelation distance from the strong fluctuation should be approximately equal to the Fresnel zone dimension. The relation between the decorrelation distance, L , and the decorrelation time, τ , can be simplified by

$$\tau = \frac{L}{v} \quad (4.11)$$

where v is the transverse drift speed. And from Equation (2.4), $v = \sqrt{\lambda z} f_{\min}$, therefore the decorrelation time is also inversely proportional to the first Fresnel minimum frequency in theory, or the Fresnel frequency in the power spectral density.

Fig. 4.8 presents the autocorrelation function of scintillation signals for events in Fig. 4.1, 21 March 2001, 19 September and 22 September 2000. Time unit (T) presents the time lag of 5 Hz digitized scintillation data, therefore decorrelation time, τ (sec) can be obtained by $T/5$ Hz with second unit. Five minutes duration of scintillation data was calculated, therefore time unit for each event equals 1500. But in this study, the time lag at the correlation coefficient equal to 0.5 is considered, as described in Fig. 4.9, then it is not necessary to determine and present the correlation coefficients of the scintillating data at the farther time series. Correlation coefficients

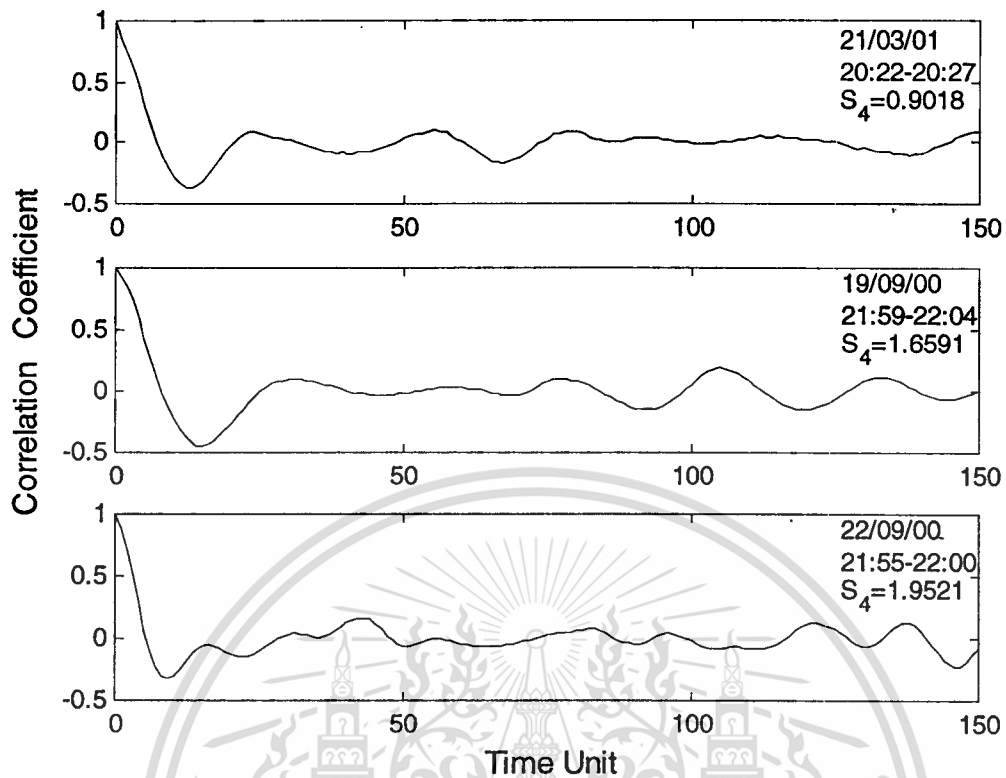


Fig. 4.8 Autocorrelation of scintillation signals

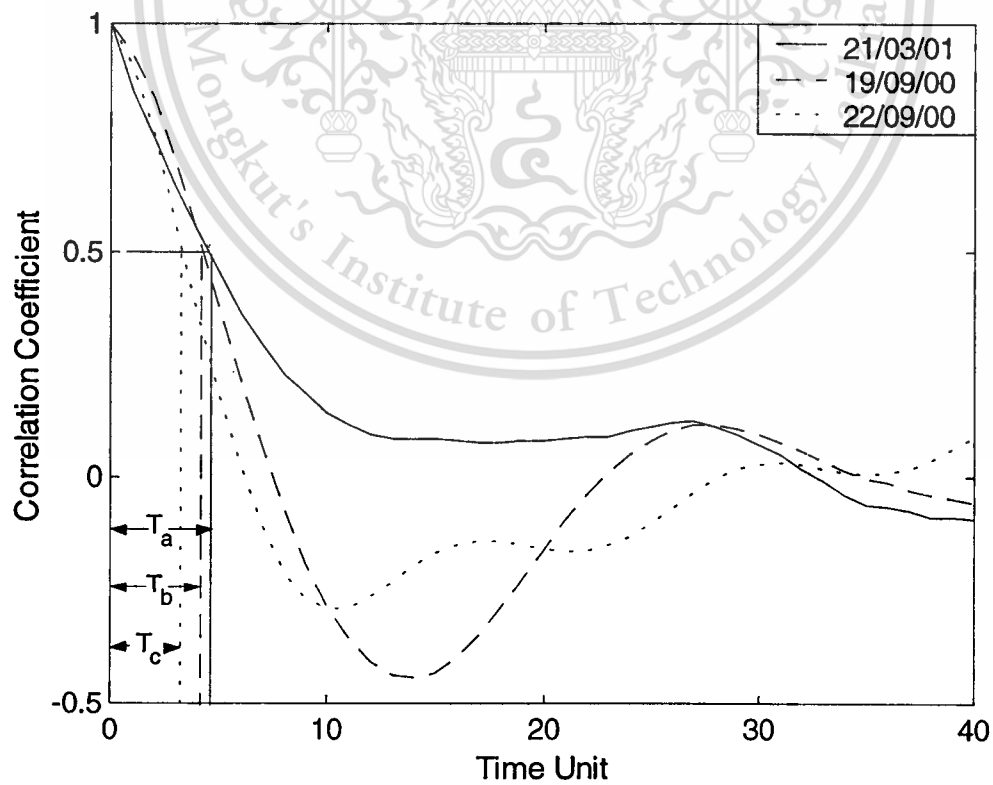


Fig. 4.9 Determination of correlation interval using time lag

This material is reserved for educational use only, not allowed for commercial use.

Forbidden to modify the content, and cite the document when use.

of each scintillation event change rapidly or not, depending on the intensity of scintillation. From Fig. 4.9, time lag of 21/03/01 event equals 4.484 and for 19/09/00 and 22/09/00 the time lags are 3.6365 and 2.9905 unit respectively. Then the correlation interval or decorrelation times can be calculated as 0.8968, 0.7273 and 0.5981 seconds respectively. When comparing with the scintillation intensity S_4 index of each event, the rapid decrease of correlation coefficient can be observed for stronger scintillation. This means that the signal does not match the T-shifted itself closely due to the strong fluctuating. For the weaker scintillation such as in 21/03/01 and 19/09/00 events, the correlation coefficients change and oscillate more slowly than 22/09/00 event that is stronger scintillation.

As is well known, the irregularities move in eastward direction in postsunset time and move in westward direction after midnight; consequently, plots of the decorrelation time varying with local time can present these irregularities movements, as the results in Fig. 4.10 and Fig. 4.11. To make the diurnal variation of the decorrelation time more meaningful, the normalized decorrelation time is taken to account; by normalizing the decorrelation time of each event with the average decorrelation time respecting to all events at the same evening. The decorrelation times of scintillation events that occurred continuously during period of 19.00 ~ 00.00 LT or after midnight have been presented in the results. The results have shown that the decorrelation times progressively increase to exceed 1.2 seconds after midnight. The decorrelation times trends do not stop moving immediately; some trends continue increasingly after midnight, and then the decorrelation times gradually decrease their values until scintillation events disappear. These can assume the movement of the irregularities that the halt direction occurred around or after midnight time. Furthermore in Fig. 4.10 (b) 22/08/00, Fig. 4.11 (a) 24/03/01 and Fig. 4.11 (b) 19/04/01, the apparent reversals can be observed. The decorrelation times become increasing again after decreasing their values around midnight. These correspond to the reversal direction, westward movement, of the irregularities. However the irregularities movement can not be determined certainly by the decorrelation time, it is solely possible to conclude whether irregularities speed varies over the diurnal period by noting the trend slope of plotting between the decorrelation time versus local time. The halt and reverse direction can be assumed to occur when the slope changes sign.

This material is reserved for educational use only, not allowed for commercial use.

Forbidden to modify the content, and cite the document when use.

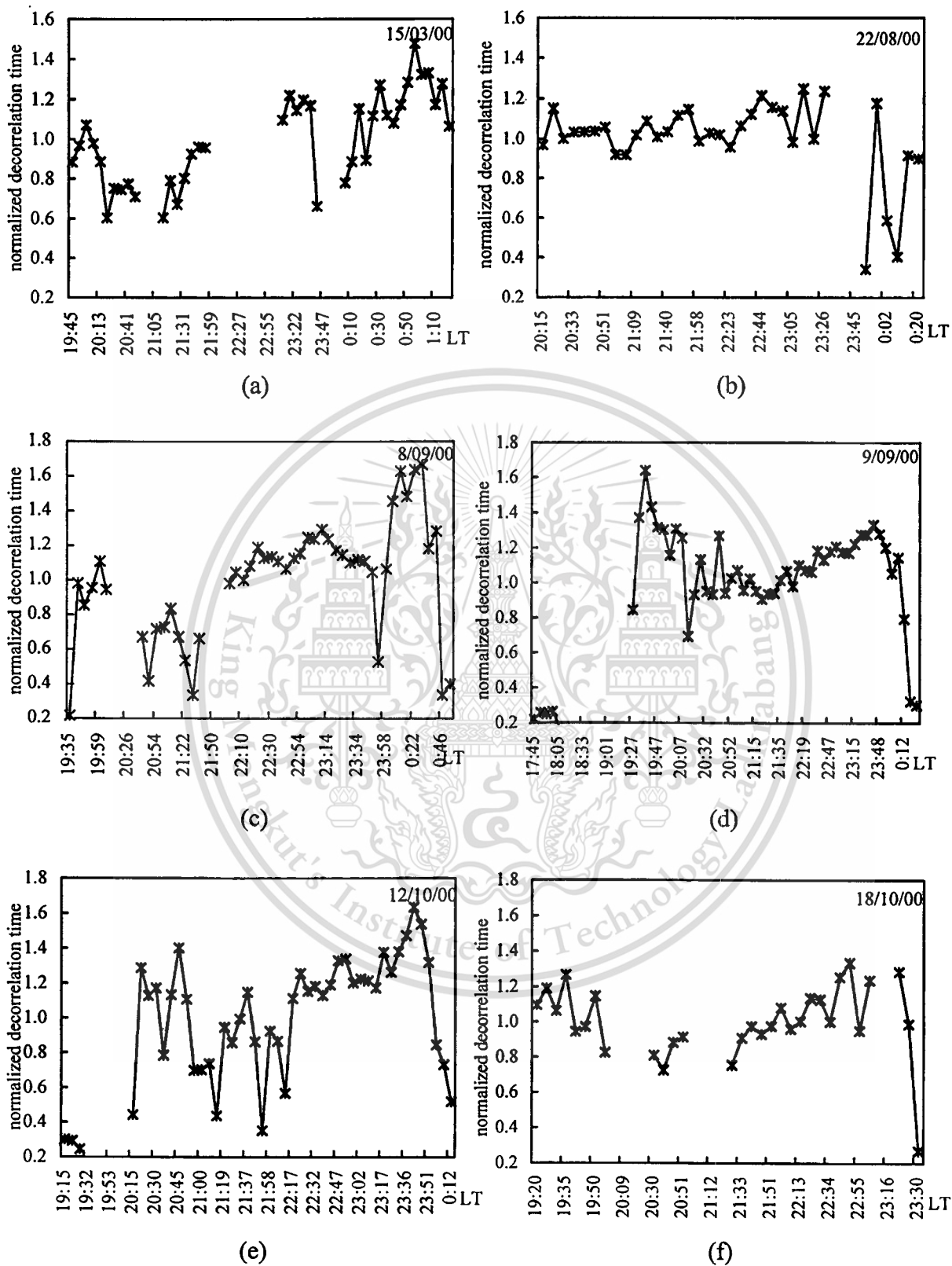


Fig. 4.10 Normalized decorrelation time versus local time of particular scintillation events in 2000

This material is reserved for educational use only, not allowed for commercial use.

Forbidden to modify the content, and cite the document when use.

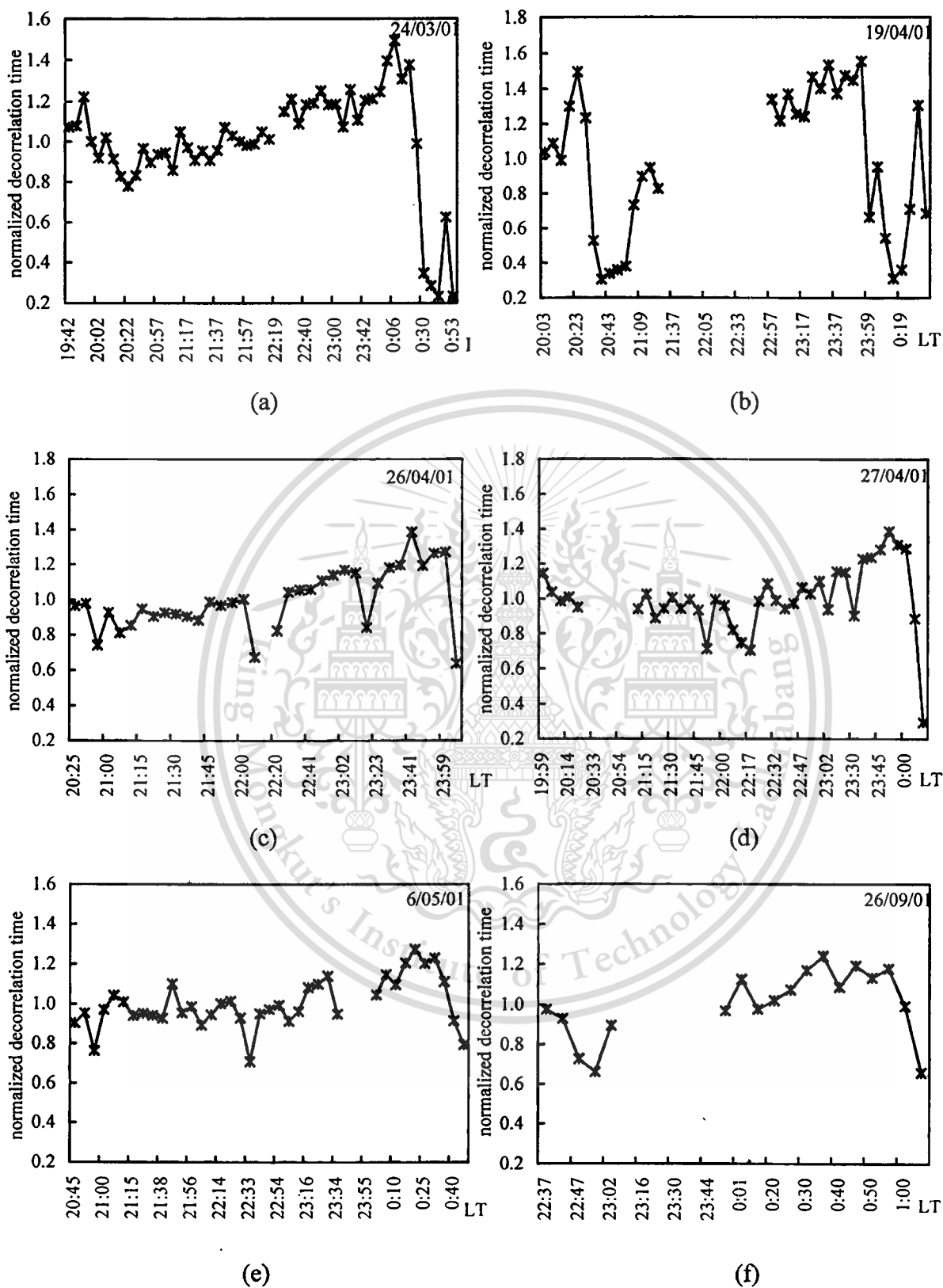


Fig. 4.11 Normalized decorrelation time versus local time of particular scintillation events in 2001

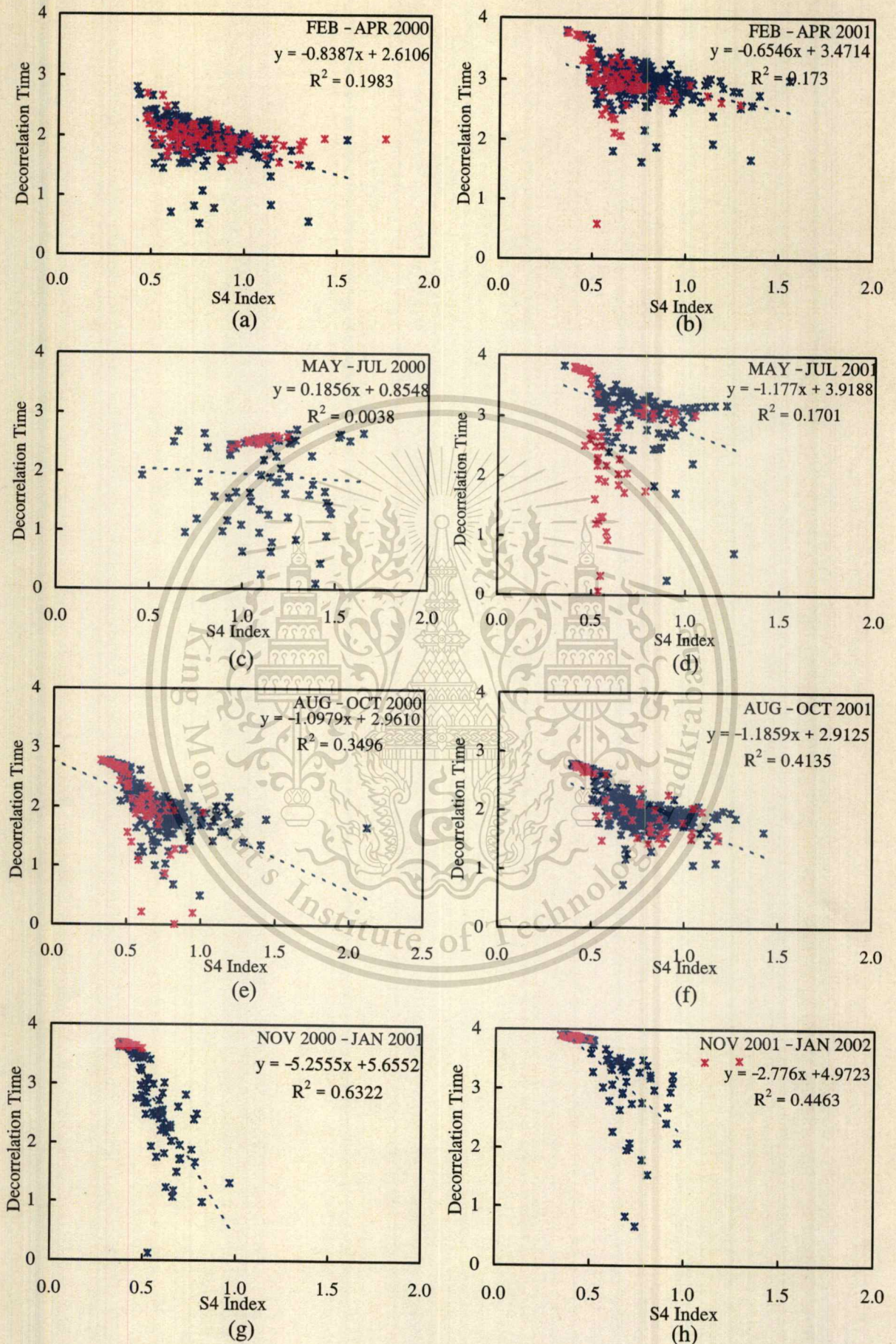


Fig. 4.12 Relation between decorrelation time and S₄ index (Feb. 2000 – Jan. 2002)

When Consider long-term analysis of decorrelation time, the variation of decorrelation time, τ , versus the scintillation intensity, S_4 index, can be obtained as the results in Fig. 4.12. Plotting between normalized decorrelation time and S_4 index of all scintillation events, that seasonally classified similarly to Fig. 4.5, presents the relation of these two data during postsunset time, blue dots; and after midnight time, red dots. The results have shown that the linear regression lines fit the relation between these normalized decorrelation time data and S_4 index data with the decreasing trend. With the exception of Fig 4.12 (c) and (d), the relation between these two data scatters randomly during postsunset time, but has the good decreasing trend after midnight for Fig. (c) May. – Jul. 2000. On the contrary, May. – Jul. 2001 in Fig. (d), the decreasing trend can be observed during post sunset time, but the random scattering can be observed after midnight instead. For scintillation events during period of Nov. – Jan. of both 2000 and 2001 as show in Fig. 4.12 (g) and (h), the decorrelation times decrease well with the increasing of scintillation intensity after midnight time; although some small occurrences appears. Furthermore for weak scintillation, ($0.2 < S_4 \leq 0.5$), the decorrelation time decreases well with the increasing of S_4 index. This can be observed clearly in both of postsunset and after midnight times. Generally, the decorrelation time decreasing rapidly in case of strong scintillation can signify the faster decorrelation of the signal itself.

4.3 Scintillating Frequency-Time Structure for Communications

4.3.1 Analysis of Scintillation Rate by Power Spectral Density and Autocorrelation Function

The decorrelation time, τ , is generally inversely related to the spectral width of roll-off part frequency of the scintillation power spectrum density. When the scintillation intensity increases, the roll-off frequency part of power spectrum density broadens; that is, the spectral width expands (Basu, S. and Basu, Su. 1981 ; Rino and Owen. 1981). According to Table 4.2, the scintillation intensity, decorrelation time and power spectral density are presented. The broadening of spectral bandwidth with the increasing of S_4 index can be observed obviously. However, the opposite conditions have also presented for events of 14/10/01 and 24/03/00. The roll-off bandwidth of these power spectral densities increases as the scintillation intensity

Table 4.2 The parameters obtained from power spectrum and autocorrelation analysis of the events (arranged in order of scintillation intensity)

Scintillation events	S_4 Index	Spectral Index, n	f_{Fresnel} (Hz)	$f_{\text{noise floor}}$ (Hz)	Roll-off Part BW	Decorrelation Time, τ
14/10/01	0.52	1.19	0.125	0.857	0.732	0.22
21/03/01	0.90	1.60	0.198	0.743	0.545	0.90
02/04/01	1.39	1.64	0.189	0.779	0.590	0.73
19/09/00	1.66	1.68	0.141	0.731	0.590	0.73
22/09/00	1.95	1.70	0.251	1.142	0.890	0.60
24/03/00	2.23	1.75	0.192	0.720	0.528	0.80

decreases; and vice versa, the bandwidth is reduced as scintillation intensity increases as described in events 14/10/01 and 24/03/00 respectively. The first case for 14/10/01 event can be assumed that satellite signal also passed through, and was effected by the tropospheric medium or multiple scattering. Then the spectral bandwidth broadened although it was weak scintillation. The latter condition can be assumed that scintillation was mainly effected by the irregularities, with smaller sizes than the Fresnel size, at the fixed altitude where the irregularities were concentrated; and the irregularities drifted across the antenna receiver beam with constant speed. However the results in Table 4.2 are not conclusive; and the variation of decorrelation time can be both broadening and narrowing. A more realistic statement is that irregularities are not stationary with non-steady speed, and multiple scattering can occur. All of these can effect the spectrum width and decorrelation time in the complicated manner (Fang and Liu. 1984).

The power spectral density and autocorrelation function of scintillation signals are studied in order to characterize the irregularities effects to satellite signals. Moreover these also can estimate the satellite signal degradation and estimate the improvement of receiver system to avoid or improve signal effected by ionospheric scintillation. The scintillation rate or fade rate can be determined by 1) power spectrum of scintillation 2) decorrelation time and 3) signal fluctuation rate over 1 second using mean crossing technique. Vilar *et.al.* (1985) have mentioned that the important feature is the apparent frequency of scintillation spectrum and the average numbers of mean crossings per second. This is referred to the scintillation fade rate,

This material is reserved for educational use only, not allowed for commercial use.

Forbidden to modify the content, and cite the document when use.

and also directly related to the power spectral density $G_x(\omega)$ and the associated autocorrelation function $R_x(\tau)$. The parameter that related to the power spectral density and autocorrelation function is the average numbers of zero crossings per second, $\overline{N_0}$. To evaluate this value, mean crossing technique is considered. In this method, the numbers of times that the signal crosses its mean level are counted and divided by two, because in each cycle of fluctuation, the signal crosses the mean level twice, as described below.

$$\overline{N_0} = \frac{N(A_t \rightarrow \pm A_{average})}{2 \times period \text{ (sec)}} \quad (4.11)$$

Where A_t is any signal level and $A_{average}$ is the mean level of the signal or 0 dB. The sign of “ $\pm A_{average}$ ” means that the signal can fluctuate over mean level twice, positive and negative direction.

$\overline{N_0}$ represents the natural frequency, $2f_0$ of the amplitude scintillation noise. The power spectrum density can be approximated by the narrow band Gaussian process with uniform density up to the corner frequency f_c to be the flat low frequency, and then spectrums rapidly decreases to be the roll-off part as discussed previously. The number $\overline{N_0}$ is theoretically given by (Vilar *et.al.* 1985).

$$\overline{N_0} = \frac{1}{\pi} \left[\frac{\int_0^{\infty} \omega^2 G_x(\omega) d\omega}{\int_0^{\infty} G_x(\omega) d\omega} \right]^{\frac{1}{2}} = \frac{1}{\pi} \left[-\frac{\ddot{R}(0)}{R(0)} \right] \quad (4.12)$$

Model that fits well with the experimental $R(\tau)$ is the exponential cosine function of

$$R(\tau) = Ae^{-x\tau} \cos(x\tau) \quad (4.13)$$

One can show that the natural frequency f_0 is given by

This material is reserved for educational use only, not allowed for commercial use.

Forbidden to modify the content, and cite the document when use.

$$f_0 = x\sqrt{3}/2\pi = 0.276x \quad (4.14)$$

The 3 dB corner frequency of the spectrum, f_c , is given by $0.35x$, the spectral density can directly provide the value of x and then f_0 . Accordingly, these values are used to estimate the statistics of scintillation fade rate.

Equation (4.12) and (4.13) present the theoretical relation of scintillation fade rate determining from mean crossing technique, power spectral density and autocorrelation function. For the experiment, Equation (4.11) and (4.14) are considered to calculate $\overline{N_0}$. For instance, event 19/09/00 has the 3 dB corner

frequency, $f_c = 0.187$ Hz. From $f_c = 0.35x$ as mentioned above, $x = \frac{0.187}{0.35} = 0.534$

, then from (4.14) $f_0 = 0.1475$, finally the scintillation fade rate determined from power spectrum can be determined; $\overline{N_0} = 2f_0 = 0.29$ zero crossings/sec or one

crossing every 3.39 seconds. The scintillation fade rate can be determined from the autocorrelation function by taking the inverse of the 50% decorrelation time, $\frac{1}{\tau}$. In

this case using τ without dividing by sampling data is considered, consequently, fade rate can be calculated equal to $\frac{1}{3.636} = 0.275$. The mean crossing technique can

estimate the number of times that signal crossing zero mean, $N = 188$ times, $\therefore \overline{N_0} = \frac{188 \text{ times}}{2 \times 300 \text{ sec}} = 0.313$ zero crossings/sec or about 0.31 Hz or one crossing every 3.19 s.

Table 4.3 describes the scintillation fade rate determined by mean crossing technique, autocorrelation function and power spectrum density of the events in Table 4.2. Fade rate calculation from each method does not have the good agreement with all other method. As the results, scintillation fade rate values calculated by power spectrum are generally close to the values calculated by mean crossing technique, as presented for 21/03/01, 02/04/01 and 19/09/00 events. The events of 22/09/00 and 24/03/00 have the close values of scintillation fade rate between mean crossing technique and autocorrelation method. For event 14/10/01, there is not the relation between the fade rate calculated from any method. This may be caused by the structure of the medium through that signals propagated or the signal fluctuation due to multiple scattering as discussed previously. However, these results can not be concluded absolutely that

which method can inform the rate of scintillation actually depending on the numbers of scintillation events used to analyze.

Table 4.3 Calculation of scintillation fade rate (arranged in order of scintillation intensity)

Scintillation Events	Times of zero mean crossing / event	3 dB Corner Frequency (f_c Hz)	Decorrelation Time (τ sec)	Scintillation Fade Rate (\overline{N}_0) calculated by		
				Mean Crossing	PSD	Auto Correlation
14/10/01 20:27-20:32	114	0.182	0.22	0.38	0.29	0.90
21/03/01 20:22-20:27	135	0.278	0.90	0.45	0.44	0.22
02/04/01 23:33-23:38	115	0.228	0.73	0.38	0.37	0.27
19/09/00 21:59-22:04	93	0.187	0.73	0.31	0.29	0.27
22/09/00 21:55-22:00	107	0.256	0.60	0.36	0.40	0.33
24/03/00 22:50-22:55	81	0.203	0.80	0.27	0.32	0.25

4.3.2 Ground Decorrelation Distance for Space Diversity Antenna

The study of this chapter can obtain some characteristics of the irregularities that can be applied for communication system in order to avoid or improve signal degradation due to ionospheric scintillation. The multiplication between the decorrelation time and the drift velocity of the irregularities can give the decorrelation distance on the ground. This ground decorrelation distance can be used for the required antenna diversity or space diversity.

Table 4.4 presents the ground decorrelation distances of scintillation events by multiplying τ with the drift velocity of transverse irregularities. This velocity has been determined from average eastward drift velocity, 100 m/s, by taking into account

Table 4.4 Ground decorrelation distance

Scintillation Events	Decorrelation Time, (τ sec.)	Ground Decorrelation Distance, ($v \times \tau$ m.)
14/10/01	0.22	18.12
21/03/01	0.90	73.72
02/04/01	0.73	60.28
19/09/00	0.73	59.78
22/09/00	0.60	49.16
24/03/00	0.80	65.98

the respective path inclination angle, as discussed previously in Chapter 3. From Equation (3.2), the estimated drift speed perpendicular to the propagation path is equal to $V_{\perp} = 100 \sin(42.40^{\circ}) + 20 \cos(42.40^{\circ}) = 82.12$ m/s. Therefore, the decorrelation distances = $V_{\perp} \times \tau = 82.12 \tau$ as presented in Table 4.3. This drift can be determined differently for other station depending on the average velocity over that station and the inclination path of receiving signal. The results in Tables 4.4 suggest that the antenna separations of the distance about 70 meters may be required for space diversity operation.

The average long-term decorrelation distances from two years scintillation events have been determined such as; for year 2000, Feb.–Apr. ≈ 47 m., May.–Jul. ≈ 28 m., Aug.–Sep. ≈ 37 m. and Nov. 2000- Jan. 2001 ≈ 22 m. Then, for year 2001, the average decorrelation distances are 46 m., 53 m., 41 m. and 34 m. respectively. Therefore, when consider these results, the decorrelation distance corresponding to the irregularities effects of these 2 years data can be estimated about 50 meters. Generally, the ground decorrelation distance should not be exceeded the Fresnel zone size, about 219 meters for KMITL site. However the decorrelation distances of more long-term events should be calculated to determine the actual distance appropriately to the effect of ionospheric irregularities of the individual station. In addition, the decorrelation distance equal to the Fresnel zone size (≈ 219 m.) can be used to separate the space-receiver observations in order to measure the drift velocity over the station. Three space-receiver observations can obtain the mutual correlation analysis among received signals to study the irregularities drift speed (Liu and Franke. 1986).

This material is reserved for educational use only, not allowed for commercial use.

4.4 Conclusion

The frequency and time structures of scintillation signal have been studied and presented here by analyses of scintillation power spectral density and autocorrelation function respectively. The scintillation slope, spectral index, decorrelation time and other parameters have been computed for each event segment over 5 minutes, and averaged to obtain the statistical parameters for the whole data segments. Many important parameters can be obtained such as spectral slope, spectral index, Fresnel/noise floor frequency and decorrelation time. Seasonal variation can not be found in these results, but the diurnal variation can be observed clearly especially after midnight. The linear increasing of the power spectral index with time increasing indicates more rapid dissipation of smaller-scale irregularities for later scintillation events. The halt or reversal movement of the irregularities can be presented by the scattering or the decreasing values of the spectral index after midnight. Moreover, the spectral index relates to S_4 index as the relation of $S_4 \propto f^{-n}$; spectral index increases as scintillation intensity increases. On the contrary, the decorrelation time has a dependence on S_4 in the opposite way; it decreases rapidly in case of strong scintillation that signifies the faster decorrelation of the signal. Comparing with the PSD, the broadening of PSD is closely related to the decorrelation time; the smaller decorrelation time is, the more the spectrum broadening. The decorrelation time also has the diurnal variation. It gradually increases its value until around or after midnight. The value of the decorrelation time becomes decrease immediately before the scintillation event disappears. This can inform the halt of the irregularities drift after midnight. In some events, the decorrelation time increases again corresponding to the reversal movement of the irregularities to westward direction.

Finally, parameters obtained from above analyses are also applied to the communications. Using 3-dB corner frequency, the decorrelation time, and mean crossing technique can determine the scintillation fade rate. Period of time signal fluctuating in one cycle can be estimated; and used to design the sufficiently fast response time for step-tracking or uplink power control systems in order to compensate scintillation effects. The ground decorrelation distances, $V_{\perp} \times \tau$, can be used for space-diversity antenna to improve or avoid the degradation of scintillation signals. The distance ≈ 219 m. (Fresnel zone size) is also useful for multipoint observations to study the mechanisms which form irregularities structures.

CHAPTER 5

AMPLITUDE DISTRIBUTION AND FADE ANALYSIS OF SCINTILLATION SIGNAL

Although the morphological study provided the global view of the scintillation phenomena, this must be augmented by a study of signal statistics such as the probability density function, the cumulative distribution function and fade statistics as provided in this chapter. However, these statistical analyses describe only short-term amplitude distribution of temporal scintillation. Long-term analysis corresponding to the random medium of the irregularities will be considered in the next chapter.

5.1 Probability Distribution Relevant to Amplitude Fluctuation

For the description of scintillation effect to satellite signal, the time series of signal fluctuation should be observed and modeled its amplitude distribution. Amplitude scintillation constitutes a random process which is nonstationary due to the changing of the irregularities medium. However, one can regard the process as being the quasi-stationary during period that is short enough for the irregularities conditions remaining reasonably constant. Amplitude fluctuation during period of the stationarity can be evaluated the short-term probability density function (PDF) as Gaussian or Nakagami-m distribution. In some cases the distribution can be including of these two models. These two distribution have been presented below (Rec. ITU-R PN.1057. 1994). Gaussian distribution can be applied to a continuous variable of any sign; but Nakagami-m distribution is applied to the non-limited positive variable.

Gaussian or normal distribution has the probability density function as:

$$p(x) = \frac{1}{\sigma\sqrt{2\pi}} \exp\left(-\frac{1}{2}\left(\frac{x-m}{\sigma}\right)^2\right) \quad (5.1)$$

where m is the mean value and σ is the standard deviation

Hence the cumulative distribution function (CDF) of Gaussian form which yields the probability that the value x is not exceeded, is given by

This material is reserved for educational use only, not allowed for commercial use.

Forbidden to modify the content, and cite the document when use.

$$F(x) = \frac{1}{\sigma\sqrt{2\pi}} \int_{-\infty}^x \exp\left(-\frac{1}{2}\left(\frac{t-m}{\sigma}\right)^2\right) dt = \frac{1}{2} \left(1 + \operatorname{erf}\left(\frac{x-m}{\sigma\sqrt{2}}\right)\right) \quad (5.2)$$

Therefore, the probability that the value x is exceeded can give by $1 - F(x)$

Nakagami-m distribution has the probability density function as

$$p(x) = \frac{2m^m}{\Gamma(m)\Omega^m} x^{2m-1} e^{-\frac{m}{\Omega}x^2} \quad (5.3)$$

where $\Omega = \overline{x^2}$ presents the average signal power, and m -coefficient is related to the scintillation index S_4 by (Rec. ITU-R P.531-4. 1997)

$$m = \left(\frac{\Omega}{x^2 - \Omega}\right)^2 = \frac{1}{S_4^2} \geq \frac{1}{2} \quad (5.4)$$

Its CDF has a close form expression which is given below, where $\Gamma(m, mI)$ and $\Gamma(m)$ are the incomplete gamma function and gamma function, respectively.

$$F(x) = \int_0^x p(x) dt = \frac{\Gamma(m, mI)}{\Gamma(m)} \quad (5.5)$$

The results for amplitude fluctuation distribution and statistics have been presented and compared with the theoretical models. Fig. 5.1 and 5.2 show the typical probability density function (PDF) and cumulative distribution function (CDF) for amplitude scintillation, occurred simultaneously at KMITL and CMU, and compared with the predicted distribution for Gaussian and Nakagami-m distribution. As can be seen from the results, both models fit well with the observed amplitude distribution. The slightly greater spread in the tails of the experimental PDF than either of the two models can be observed. This may be the result of using scintillation data that was probably not short enough for the scintillation intensity σ to remain constant. The Gaussian PDF is a closer fit to the large enhancements while the Nakagami-m is a closer fit to the large fades. For small fluctuations, there is small difference between

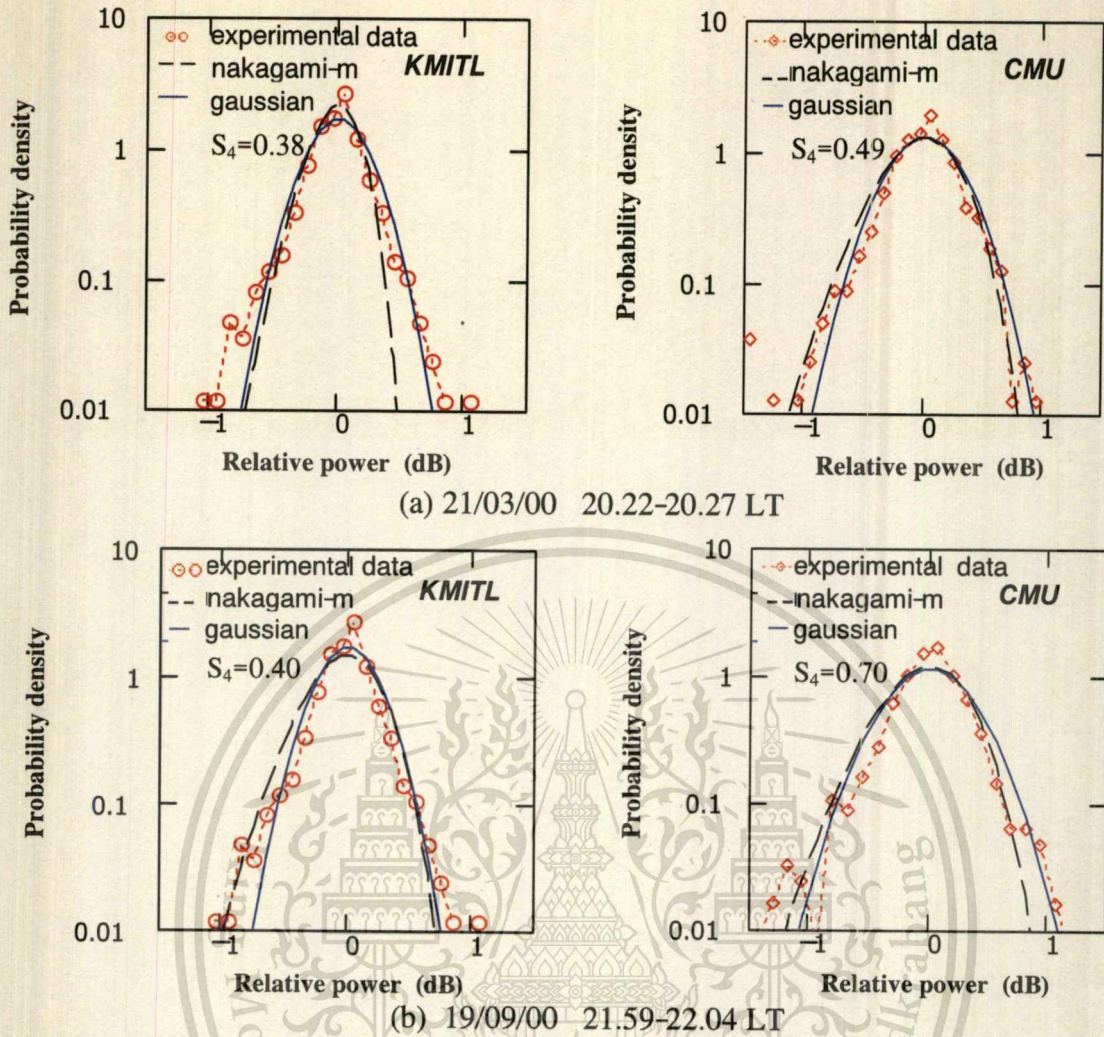


Fig. 5.1 Comparison between experimental data, Nakagami-m and Gaussian probability density function of KMITL and CMU scintillation

these distributions. Therefore, the PDF of weak scintillation can be presented equally well by either Gaussian or Nakagami-m distribution. The information of the CDF can define the fade margin requirement for communication systems as it expresses the probability that the signal level will equal or exceed the given decibel level. The scintillation levels which are particularly interesting for a system engineer, and can be obtained from the CDF are the peak enhancement, maximum fade, 5% peak and 95% fade. Difference between the 5% peak and 95% fade level presents the receiver dynamic range to be employed in the satellite system receiver (Banerjee *et.al.* 1992). Table 5.1 presents the dynamic ranges corresponding to CDF results of Fig. 5.2. The receiver dynamic ranges relate to the increases of scintillation intensity. However all scintillation events calculation can obtain the average receiver dynamic ranges appropriately to the scintillation characteristics in the particular station.

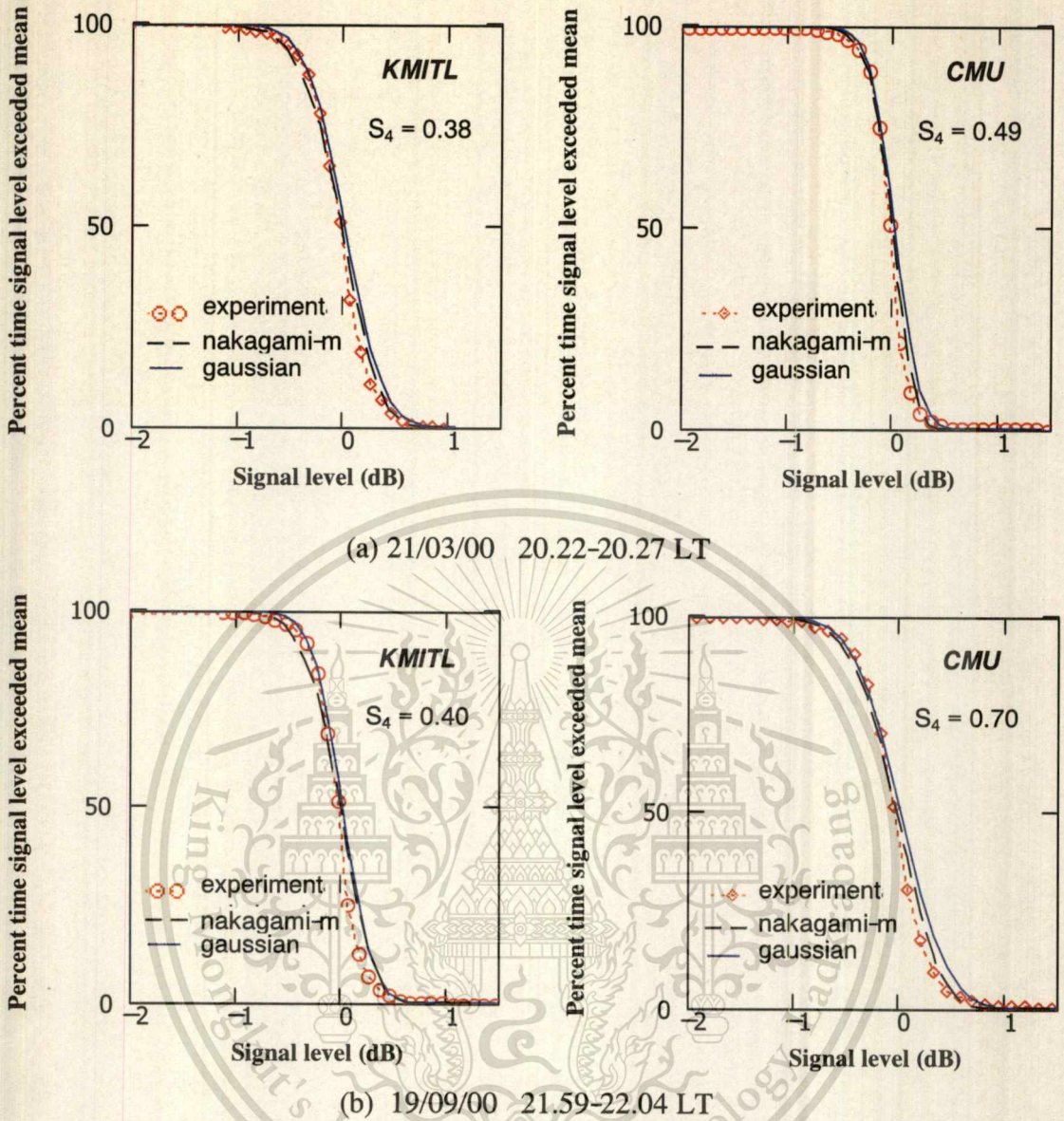


Fig. 5.2 Comparison between experimental data, Nakagami-m and Gaussian cumulative distribution function of KMITL and CMU scintillation

Table 5.1 Cumulative distribution function statistics

Scintillation Events	S_4 Index	Peak Enhancement (dB)	Maximum Fade (dB)	5 % Peak (dB)	95 % Fade (dB)
KMITL 21/03/00	0.38	1.315	-1.405	0.625	-0.785
KMITL 19/09/00	0.40	1.416	-1.284	0.566	-0.814
CMU 21/03/00	0.49	1.796	-2.314	0.796	-1.064
CMU 19/09/00	0.70	2.065	-2.635	1.30	-1.545

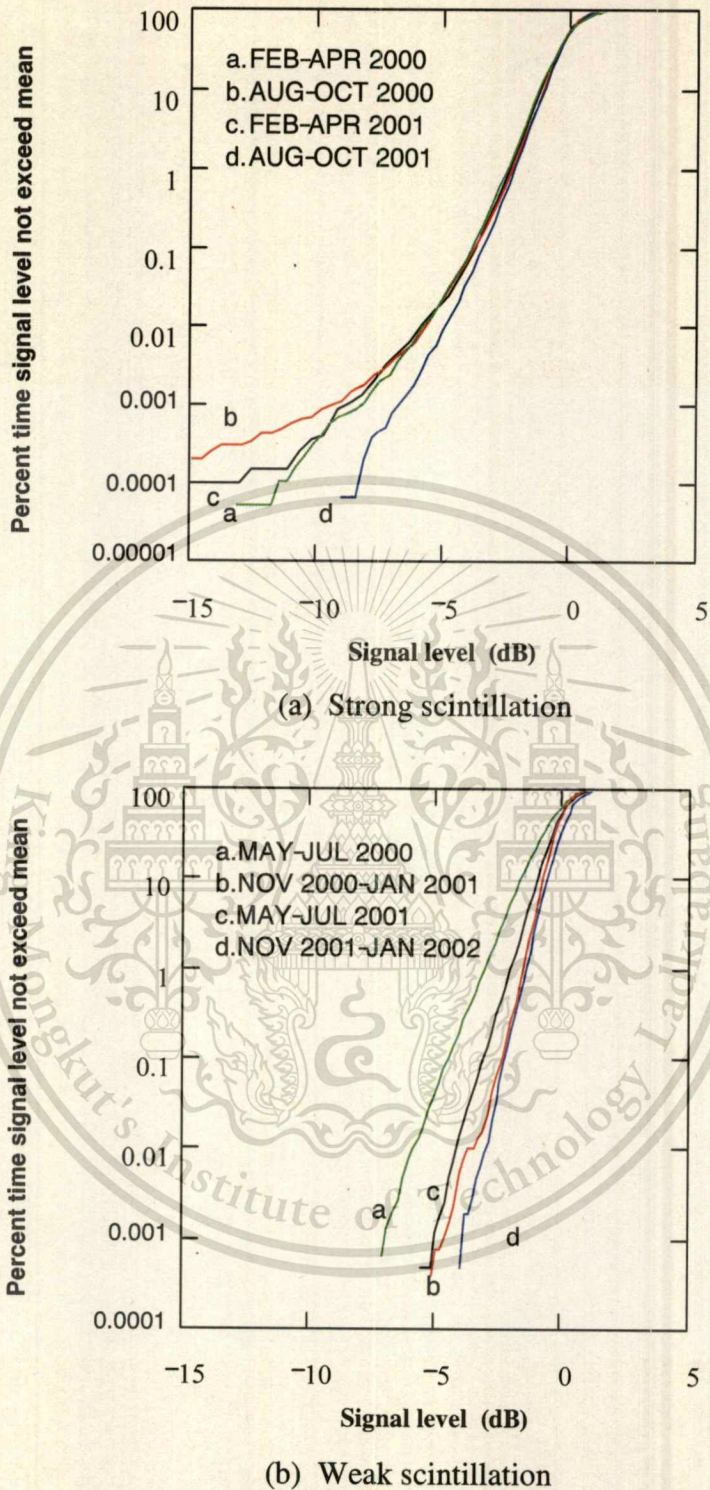


Fig. 5.3 Cumulative distribution of amplitude fluctuation at KMITL station
 (a) Strong scintillation (b) Weak scintillation

Fig. 5.3 presents the cumulative distribution for strong and weak scintillation with the abscissa indicating the probability $F(x < X)$ for the fluctuation values not exceeding x . This material is reserved for educational use only, not allowed for commercial use.

exceeding the decibel levels in X-axis. The signals not exceeding zero mean have the 50 percentage for strong scintillation and weak scintillation. In weak scintillation, although scintillation occurred in May. – Jul. 2000 has the intensity less than others; but the fade scintillation characteristics are dominant. Signal fading is more important than signal enhancement. These results present the amplitude fluctuation in fade and can be used to determine the fade margin for overcoming this propagation effect. These will be discussed later.

5.2 Fade Statistic Analysis of Scintillation Signal

In addition to the information of the scintillation fading on the amplitude signals estimated by the cumulative distribution, statistical description of the fade rate is important to characterize the scintillation effects on the communication channel. Information on the fade rate can be evaluated either by level-crossing techniques or by Fourier techniques which determine power spectral density and auto-correlation function as have been described in Chapter 4. The terms “fading” and “scintillating” or “scintillation fading” are frequently used interchangeably; although fading usually refers to the deeper fading, while the last two terms generally refer to the milder condition.

5.2.1 Fade Duration Distribution

The level crossing technique proposed by (Whitney and Basu. 1977) gives the measurement of the distribution of the fades and enhancement at various levels with respect to the mean level. The fade number and fade duration have been counted every 1-dB change. According to the morphological results and the cumulative distribution of scintillation signals, this observation system, KMITL, can be assumed to be the low margin system. Most events have the relative signal fluctuation not exceeding -10 dB. Therefore, the specific threshold levels of -8 dB \sim -1 dB can be assigned for calculating the fade duration distribution.

Fig. 5.4 and 5.5 present the fade duration distribution of two years scintillation by plotting the cumulative fade duration that does not exceed the duration time in X axis. It can be described from the results; such as in April 2000, the fade margin is -6 dB, the cumulative numbers of fade corresponding to the duration time less than or equal

This material is reserved for educational use only, not allowed for commercial use.

Forbidden to modify the content, and cite the document when use.

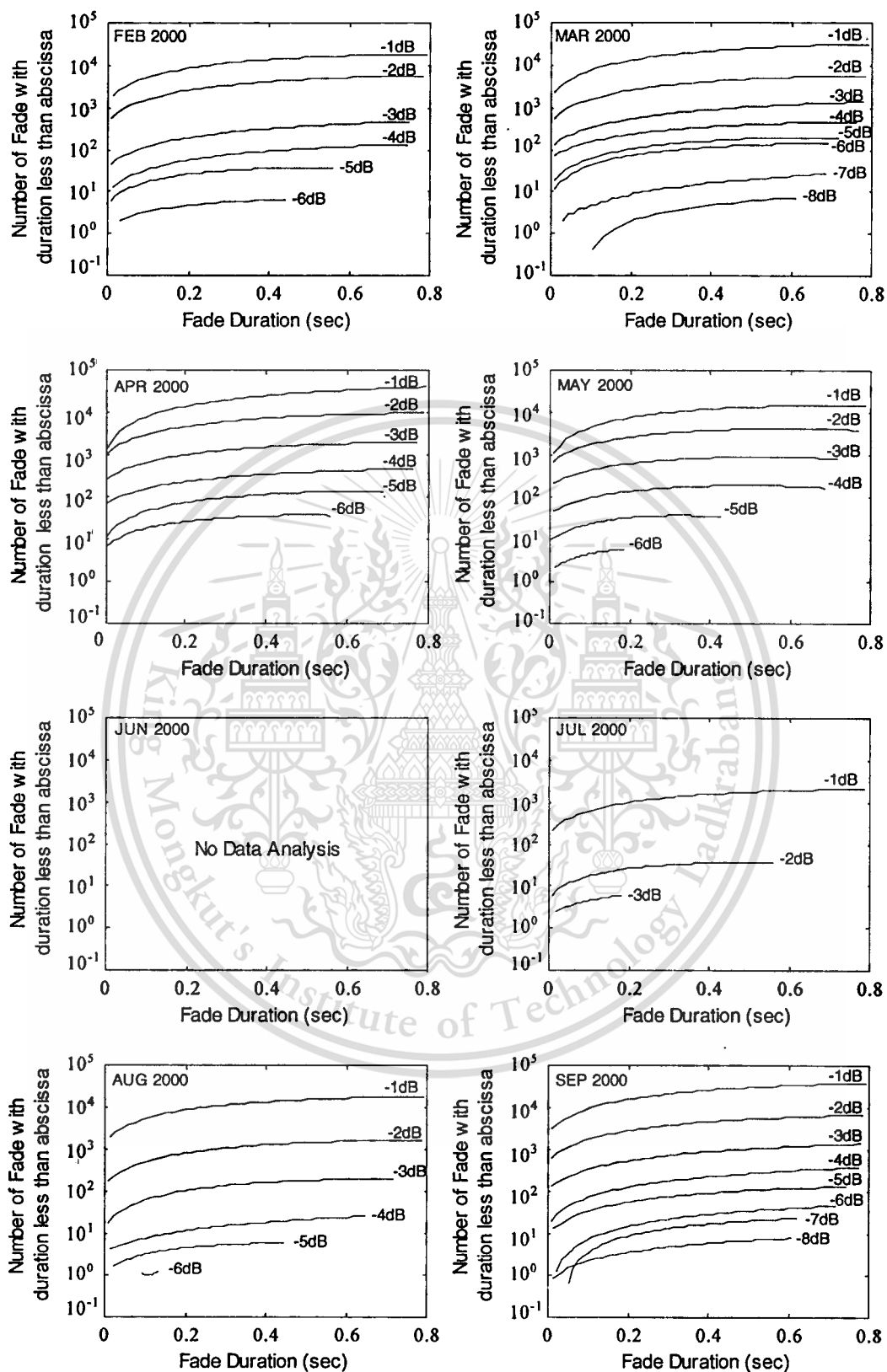


Fig. 5.4 Fade duration distribution at different fade levels for all scintillation events occurred in Feb. 2000 – Jan. 2001

This material is reserved for educational use only, not allowed for commercial use.

Forbidden to modify the content, and cite the document when use.

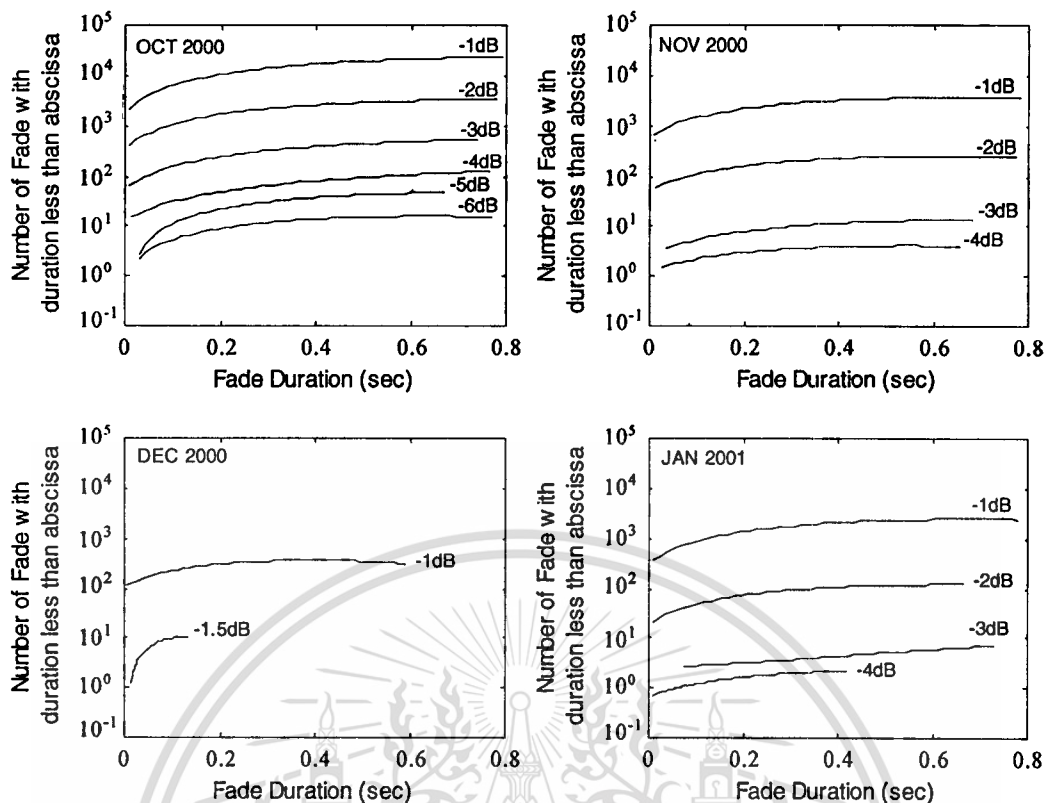


Fig. 5.4 (cont'd) Fade duration distribution at different fade levels for all scintillation events occurred in Feb. 2000 – Jan. 2001

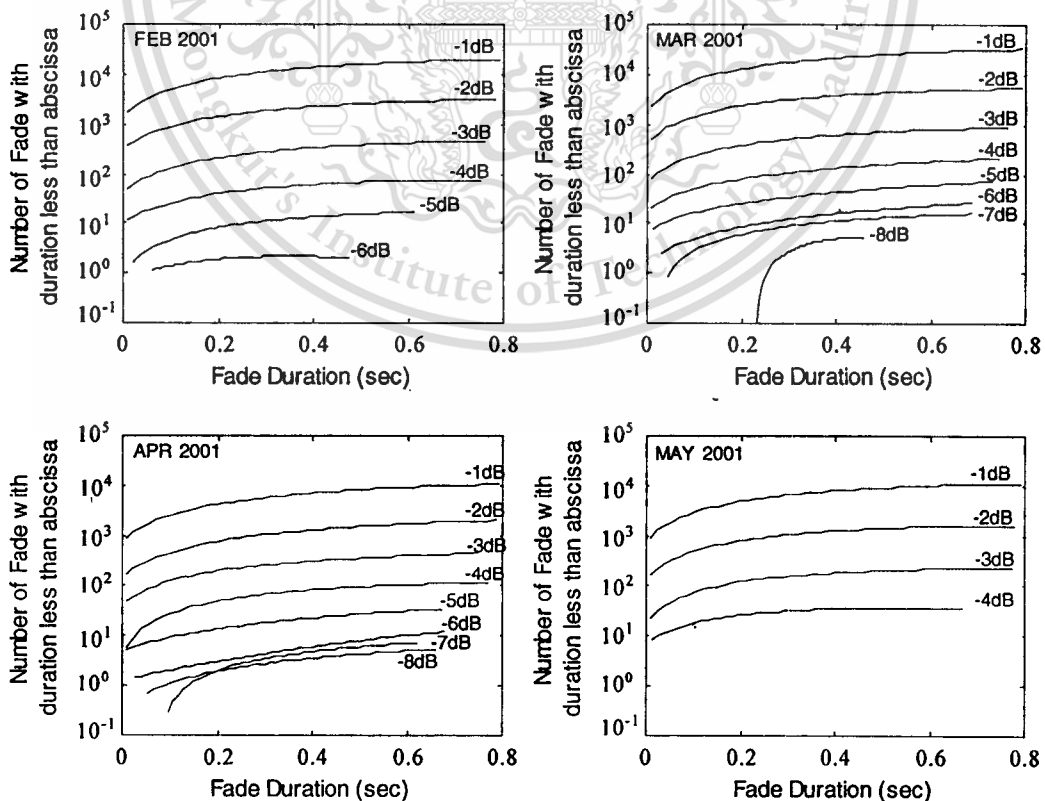


Fig. 5.5 Fade duration distribution at different fade levels for all scintillation events occurred in Feb. 2001 – Jan. 2002

This material is reserved for educational use only, not allowed for commercial use.

Forbidden to modify the content, and cite the document when use.

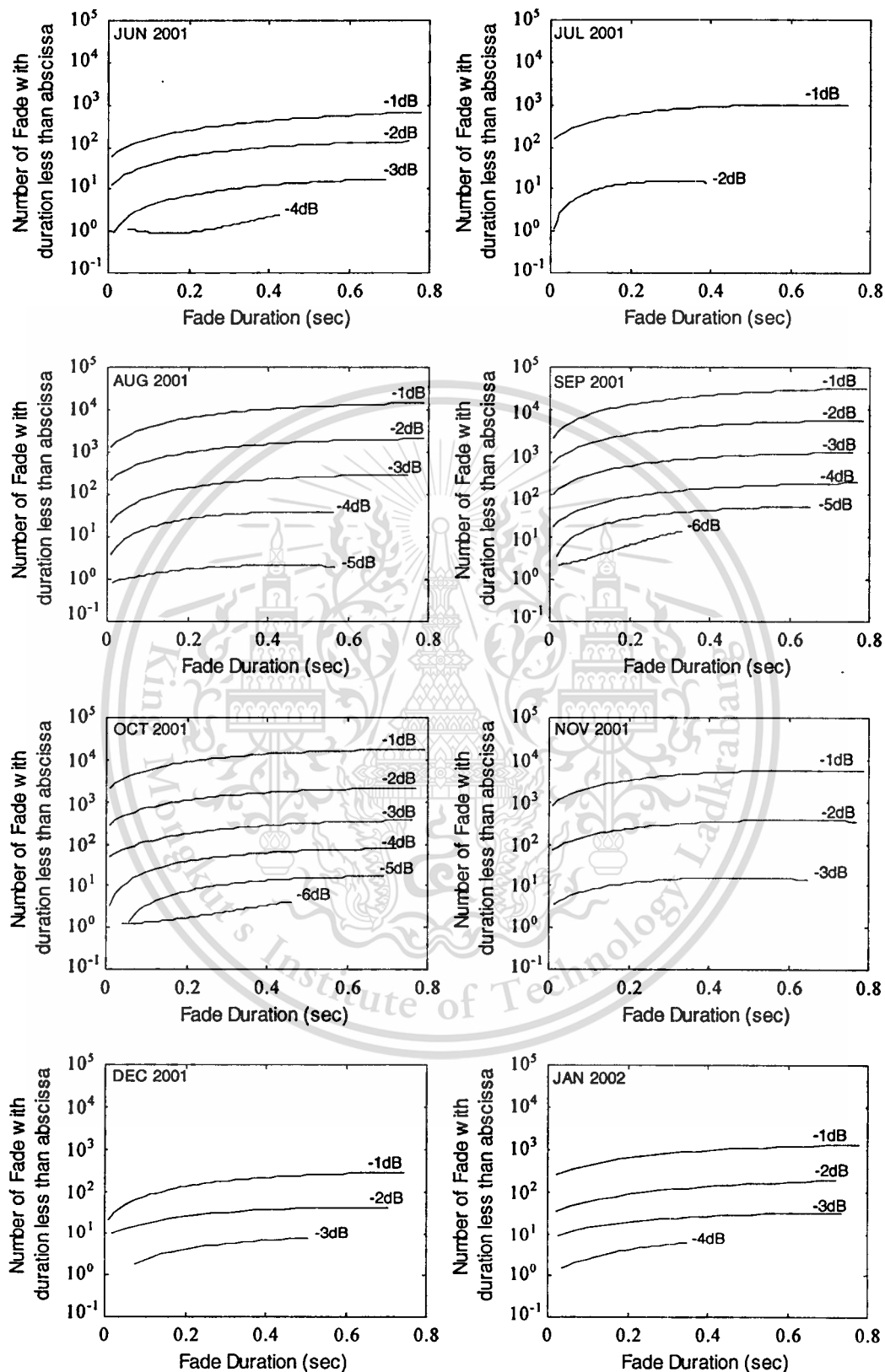


Fig. 5.5 (cont'd) Fade duration distribution at different fade levels for all scintillation events occurred in Feb. 2001 – Jan. 2002

This material is reserved for educational use only, not allowed for commercial use.

Forbidden to modify the content, and cite the document when use.

to 36. Similarly, in April 2001, the cumulative numbers of fades with duration time less than or equal to 0.6 s. for the fade margin level equal to -6 dB are only 5. But deeper scintillation fading levels can be observed in this month. The stronger scintillation can determine the numbers of fade duration at various fade levels more than weak scintillation. The number of scintillation fading exceeded -8 dB can be observed in March and September 2000, and March and April 2001. In December 2000, scintillation intensity was very weak; the fading signals did not exceed -2 dB. These results of fade duration distribution at any margin level have been used to determine the message reliability as will be described in Section 5.2.2.

Fig. 5.6 presents the cumulative fade numbers of signals fading exceeded the specific fade levels of scintillation in each month, February 2000 to January 2001 and February 2001 to January 2002. The total fade duration time when signals fluctuating exceeded the specific fade margins have been described in Fig. 5.7. According to the results of the scintillation occurrences such as amplitude levels of scintillation signals and scintillation intensity as presented in Chapter 3, these results can inform the intensity of scintillation; but for communications links, sometimes these information can not be used to estimate the losses due to scintillation. For example, when considering the occurrence numbers of scintillation between March and September 2000, scintillation occurred in September more than March. However, from the results in Fig. 5.6 and 5.7, the percentage of fade number and the total fade duration at the deep fade levels (-5 to -8 dB) of March are more than September. It means that for low margin system, lost communication can occur in March more than September. On the contrary, in March and September 2001, the peak amplitude fluctuation in September is higher than March; but from Fig. 5.6 and 5.7, more lost communication can be observed in March.

Information on the fade duration distribution and numbers of fade for various levels of fade margin are needed to characterize the communications effected by ionospheric scintillation. For high-speed digital transmission, if the duration of fade is longer than the message length, and the fade depth is below the system threshold; information could be lost fully or partially. The message reliability can present these communication losses.

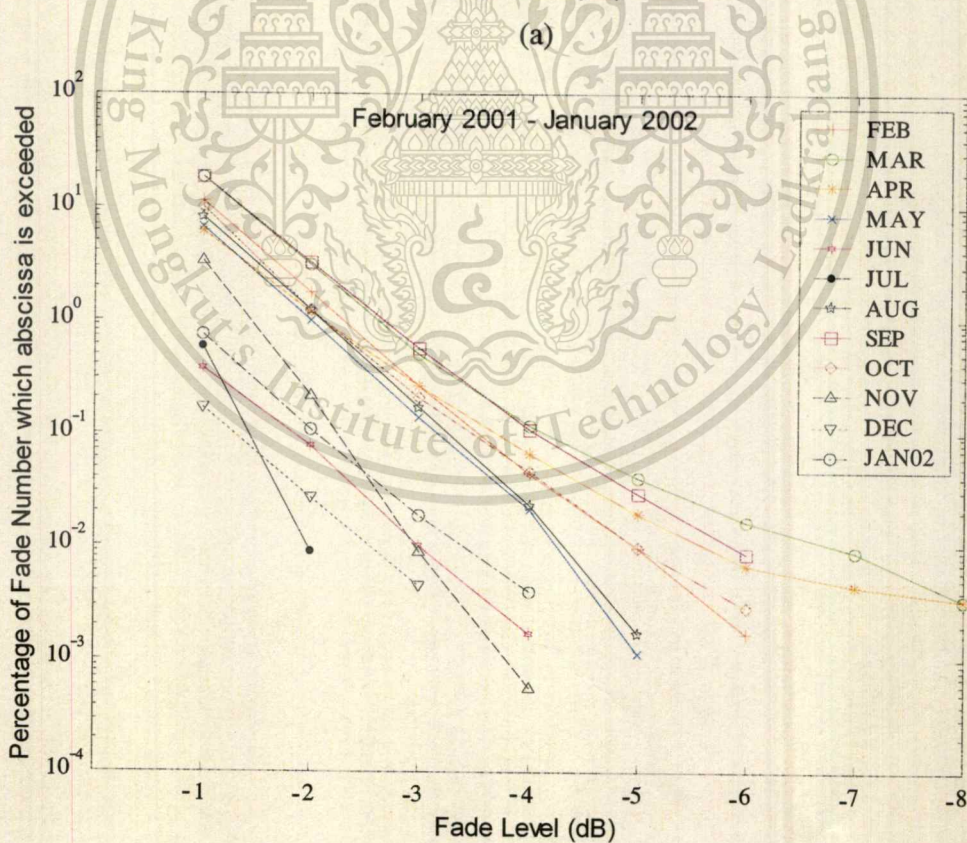
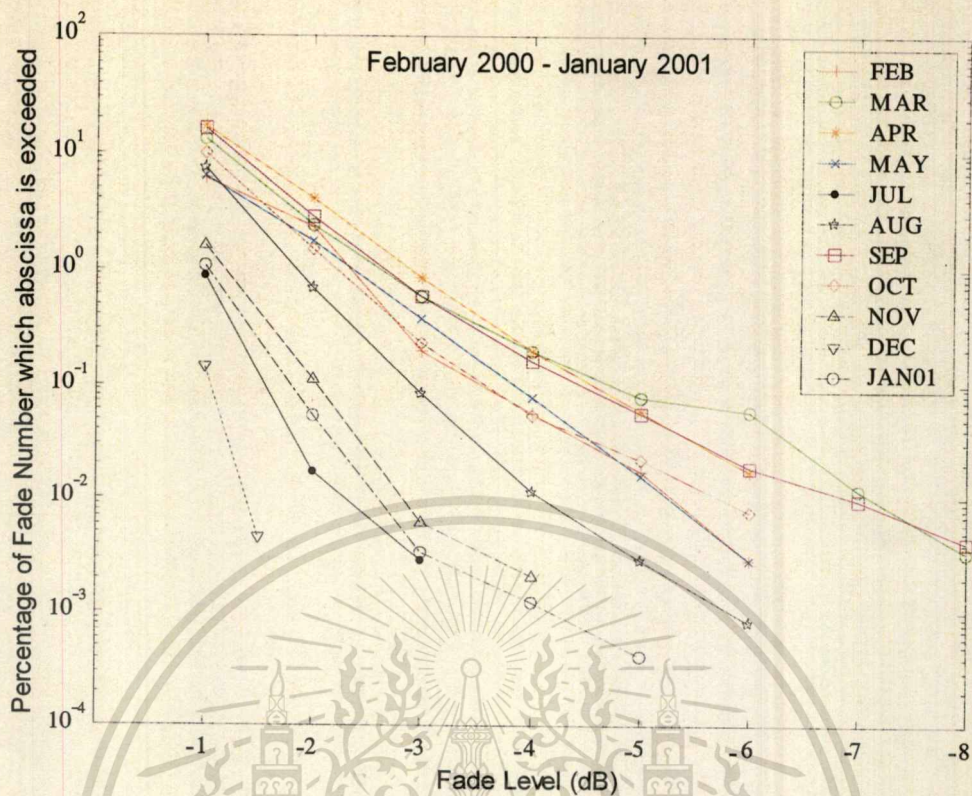


Fig. 5.6 Cumulative numbers of signal fading exceeded the specific fade levels (Feb.2000 – Jan.2002)

This material is reserved for educational use only, not allowed for commercial use.

Forbidden to modify the content, and cite the document when use.

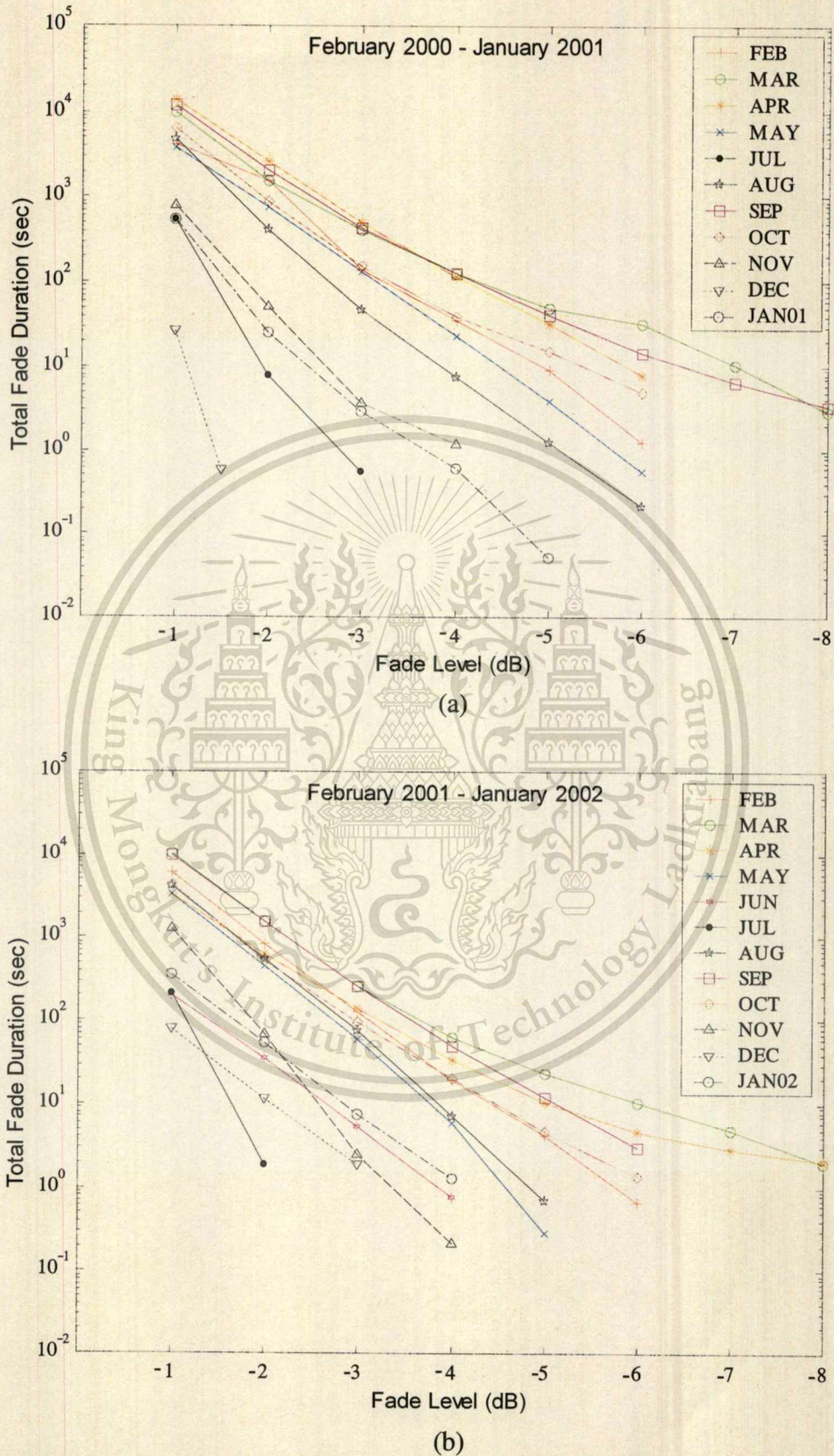


Fig. 5.7 Total fade duration time of signal fading exceeded the specific fade levels

(Feb.2000 – Jan.2002)

This material is for educational use only, not allowed for commercial use.

Forbidden to modify the content, and cite the document when use.

5.2.2 Message Reliability of Scintillation Channel

The information loss due to the ionospheric scintillation depends on the message length. The perfect message can be received only during the time interval when the signal level is greater than the fade margin, the threshold level of the given system. The message reliability has been estimated by determining the number of time intervals that completely fit within the signal enhancements or increase above the specified system threshold levels. This number will be compared with the total possible numbers or total time in the entire sample segments under consideration. The message reliability evaluation can be described as followed for any threshold level.

$$\frac{\text{Total Time} - \left(\sum T_{fade}(T \geq T_0) + n_{fade}(T < T_0)T_0 \right)}{\text{Total Time}} \times 100\% \quad (5.6)$$

where T_{fade} is the fade duration that is equal to or longer than message length, T_0

n_{fade} is the number of fade that its duration time is shorter than message length

Total Time is all possible times of entire sample segments

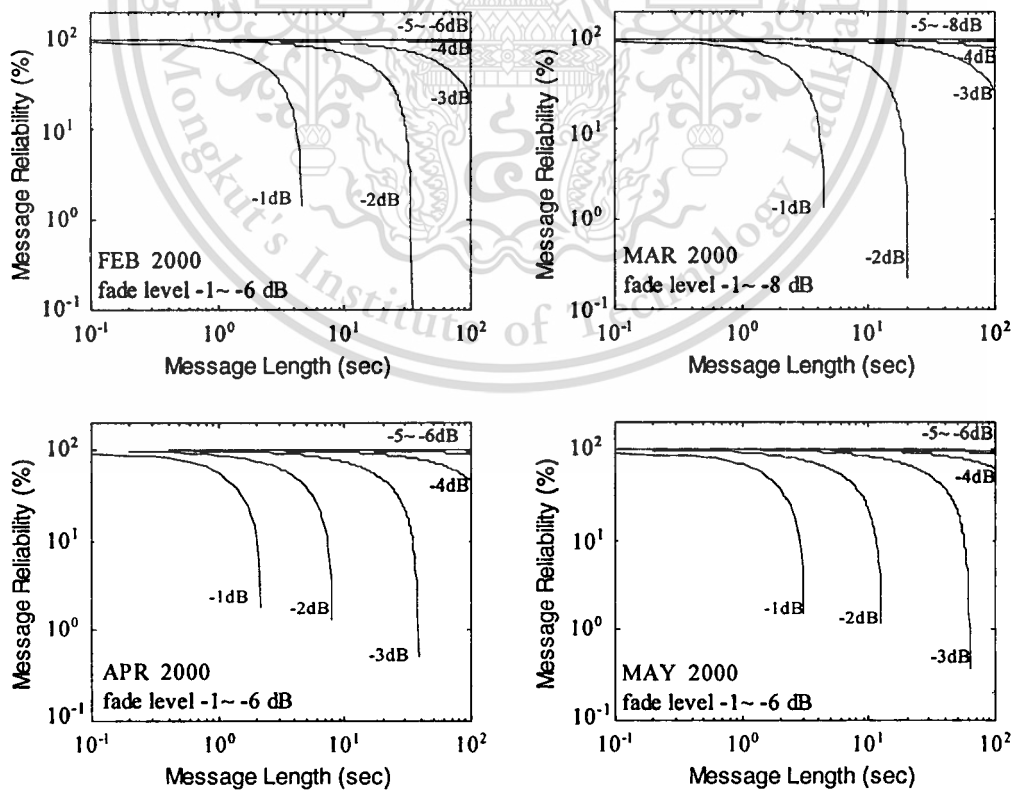


Fig. 5.8 Effect of the scintillation on the perfect messages reception for various

message lengths and fade margin levels (Feb.2000 – Jan. 2001)

This material is protected by copyright, for restricted commercial use.

Forbidden to modify the content, and cite the document when use.

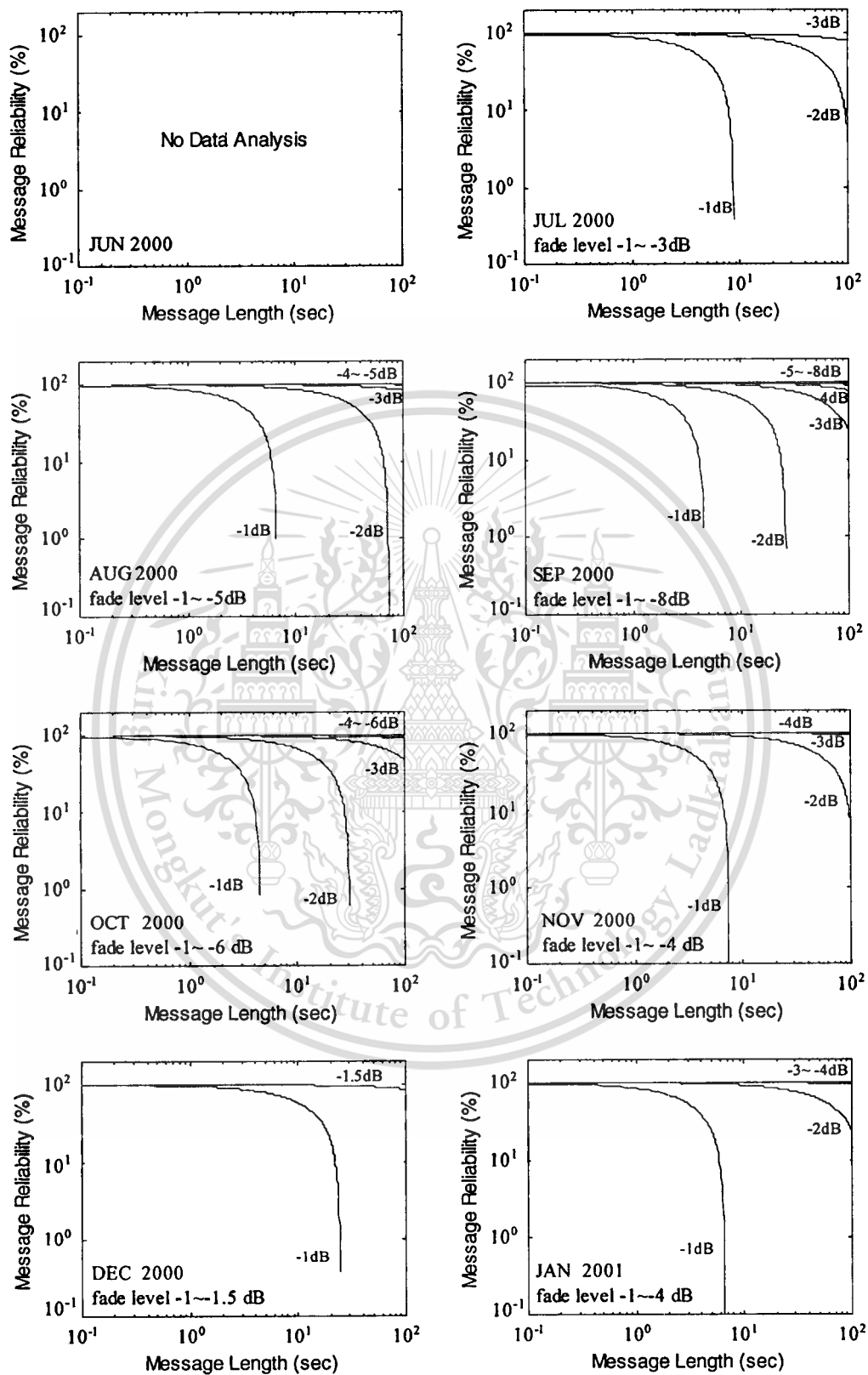


Fig. 5.8 (cont'd) Effect of the scintillation on the perfect messages reception for various message lengths and fade margin levels (Feb. 2000 – Jan. 2001)

This material is reserved for educational use only, not allowed for commercial use.

Forbidden to modify the content, and cite the document when use.

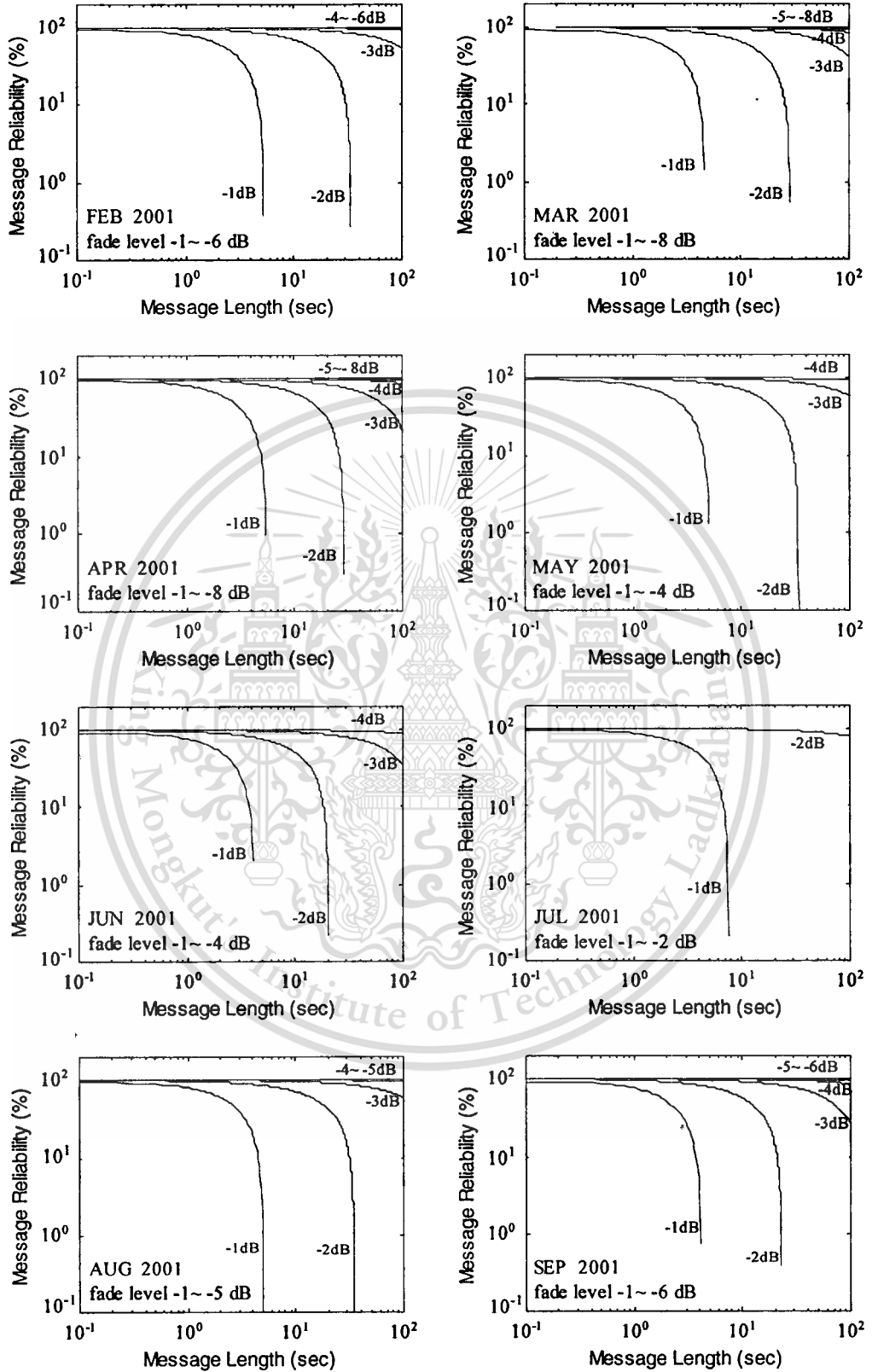


Fig. 5.9 Effect of the scintillation on the perfect messages reception for various message lengths and fade margin levels (Feb.2001 – Jan. 2002)

This material is reserved for educational use only, not allowed for commercial use.

Forbidden to modify the content, and cite the document when use.

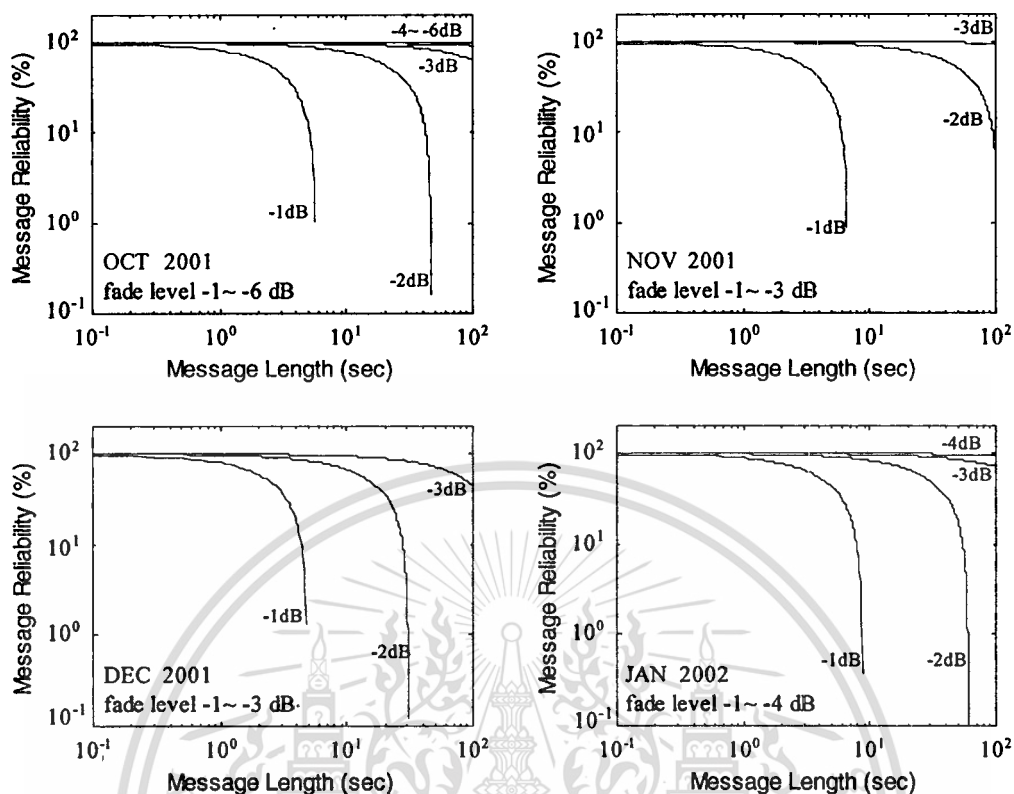


Fig. 5.9 (cont'd) Effect of the scintillation on the perfect messages reception for various message lengths and fade margin levels (Feb.2001 – Jan. 2002)

Fig. 5.8 and 5.9 present the determination of message reliability corresponding to the distribution of fade duration presented in Fig. 5.4 and 5.5 respectively. The message reliability has been estimated for different fade margins by varying message lengths. It can be observed from the results that for a given fade margin, the message reliability decreases as the message length increases. Also, the message reliability falls off more rapidly as the fade margins decrease. When considering fading rate of scintillation, if the fade rate is so fast that the time interval between fades (the duration time before scintillating signal fading next time) is shorter than the message length, this can be mentioned that no messages can be received without error.

5.3 Conclusion

This chapter presents the statistical analyses of amplitude fluctuation and scintillation fading. These short-term analyses characterize the instantaneous variability of scintillation. Moreover the results also relate to the communication

This material is reserved for educational use only, not allowed for commercial use.

Forbidden to modify the content, and cite the document when use.

performance under scintillation condition. The distribution of amplitude fluctuation is fit well with the Gaussian and Nakagami-m distribution. The Gaussian distribution closely fits to the large enhancement; and Nakagami-m distribution closely fits to the large fades. Gaussian distribution is suitable for fitting weak-to-moderate fluctuation distribution as similar to the characteristics of these scintillation; but for very large scintillation fluctuation, a better distribution is Nakagami-m. Therefore, long-term and short-term scintillation channel modeling consider only Gaussian model as will be discussed in the next chapter. Gaussian distribution is related to the standard deviation, σ , that become various values when considering many scintillation events. These values of σ will be taken into account with the short-term and long-term models.

For communication performance under ionospheric scintillation, the CDF of amplitude scintillation can inform the receiver dynamic range, between 5% peak values and 95% fade values. The fade duration distribution and message reliability present the lost communication possibility of satellite signal effected by ionospheric scintillation. More deeper fade is, more lower message reliability can be obtained. This can be mentioned that the fade statistics analysis and the message reliability can indicate the lost of communication during scintillation effects more obviously than the occurrence numbers of amplitude fluctuation.

CHAPTER 6

CHANNEL MODELING OF SCINTILLATION AND ITS IMPACT ON COMMUNICATION SYSTEM

The random characteristics of the medium through that signal propagates can effect the intensity of the signal randomly. The scintillation channel modeling and long-term distribution have also been proposed here. In addition to the fade statistics and message reliability, other communication performance effected by ionospheric scintillation such as the channel capacity and the average bit error probability evaluated by scintillation channel modeling are also presented in this chapter.

6.1 Scintillation Channel Modeling

Amplitude scintillation constitutes a random process which is nonstationary due to the irregularities medium. This leads to the constructive and destructive time-variant interference at the receiver. Therefore, not only the magnitudes of these fluctuations but the rate at which they occur are also important when regarding to the effect on communication. If the instantaneous signal amplitude received at the station is $A(t)$, and A_0 is the mean signal or unfaded amplitude. Using the Rytov approximation, the relation between both values can be written by

$$A(t) = A_0 \exp(\chi(t)) \quad (6.1)$$

where $\chi(t)$ is the random process in unit of neper. If considering in the decibel scale, the received signal $X(t)$ in dB can be obtained by

$$X(t) = 20 \log_{10} \frac{A(t)}{A_0} \text{ (dB)} = 8.686 \chi(t) \text{ dB} \quad (6.2)$$

6.1.1 Moulslley-Vilar Distribution

Long-term model of the scintillation process is based on the modified form of the Gaussian distribution in which the standard deviation is also a random variable. Assuming that the process has a zero mean value, the mathematical expectation of the

long-term probability density can be given by (Moulsley and Vilar. 1982).

$$\langle p(\chi) \rangle = \int_0^{\infty} p(\sigma_\chi) p(\chi, \sigma_\chi) d\sigma_\chi \quad (6.3)$$

where $p(\chi, \sigma_\chi)$ is the Gaussian probability density function of short-term scintillation process as a function of σ_χ and χ . According to Equation (5.1), $p(\chi, \sigma_\chi)$ can be given by

$$p(\chi, \sigma_\chi) = \frac{1}{\sigma_\chi \sqrt{2\pi}} \exp\left(-\frac{\chi^2}{2\sigma_\chi^2}\right) \quad (6.4)$$

$p(\sigma_\chi)$ is the probability density function of the standard deviation σ_χ . The square values of this random variable distribute log-normally, hence $p(\sigma_\chi^2)$ is the log-normal density function. However, according to Equation (6.3) and (6.4), it is more useful to consider that $p(\sigma_\chi^2)$ has the normal or Gaussian distribution by defining $p(\ln \sigma_\chi^2)$ instead. The value of $\ln \sigma_\chi^2$ has the normal distribution form as

$$p(\ln \sigma_\chi^2) = \frac{1}{\sigma_\sigma \sqrt{2\pi}} \exp\left(-\left(\frac{\ln \sigma_\chi^2 - \ln \sigma_m^2}{2\sigma_\sigma^2}\right)^2\right) \quad (6.5)$$

where the mean value of $\ln \sigma_\chi^2$, $\overline{\ln \sigma_\chi^2} = \ln \sigma_m^2$ and the standard deviation of $\ln \sigma_\chi^2$, $\sigma(\ln \sigma_\chi^2) = \sigma_\sigma$. From the conventional transformation of two probabilities;

$$P_y(y) = \frac{P_x(x)}{|g'(x)|} \quad (6.6)$$

σ_χ can be defined as y and $\ln \sigma_\chi^2$ can be defined as x ; where y is the function of x , $y = g(x) = \sqrt{\exp(\chi)}$ (Papoulis. 1991). Hence $p(\sigma_\chi)$ can be determined by using

This material is reserved for educational use only, not allowed for commercial use.

Equation (6.6) and $p(\ln \sigma_\chi^2)$ as following

$$p(\sigma_\chi) = \frac{1}{\sigma_\sigma \sigma_\chi} \sqrt{\frac{2}{\pi}} \exp \left[-\frac{(\ln \sigma_\chi^2 - \ln \sigma_m^2)^2}{2\sigma_\sigma^2} \right] \quad (6.7)$$

Combining Equation (6.3), (6.4) and (6.7), then the long-term probability density function of χ can be obtained as Equation (6.8).

$$\langle p(\chi) \rangle = \int_0^\infty \frac{1}{\sigma_\chi \sqrt{2\pi}} \exp\left(-\frac{\chi^2}{2\sigma_\chi^2}\right) \frac{1}{\sigma_\sigma \sigma_\chi} \sqrt{\frac{2}{\pi}} \exp \left[-\frac{(\ln \sigma_\chi^2 - \ln \sigma_m^2)^2}{2\sigma_\sigma^2} \right] d\sigma_\chi$$

$$\therefore p(\chi) = \frac{1}{\sigma_\sigma \pi} \int_0^\infty \frac{1}{\sigma_\chi^2} \exp \left[-\frac{\chi^2}{2\sigma_\chi^2} - \frac{(\ln(\sigma_\chi^2 / \sigma_m^2))^2}{2\sigma_\sigma^2} \right] d\sigma_\chi \quad (6.8)$$

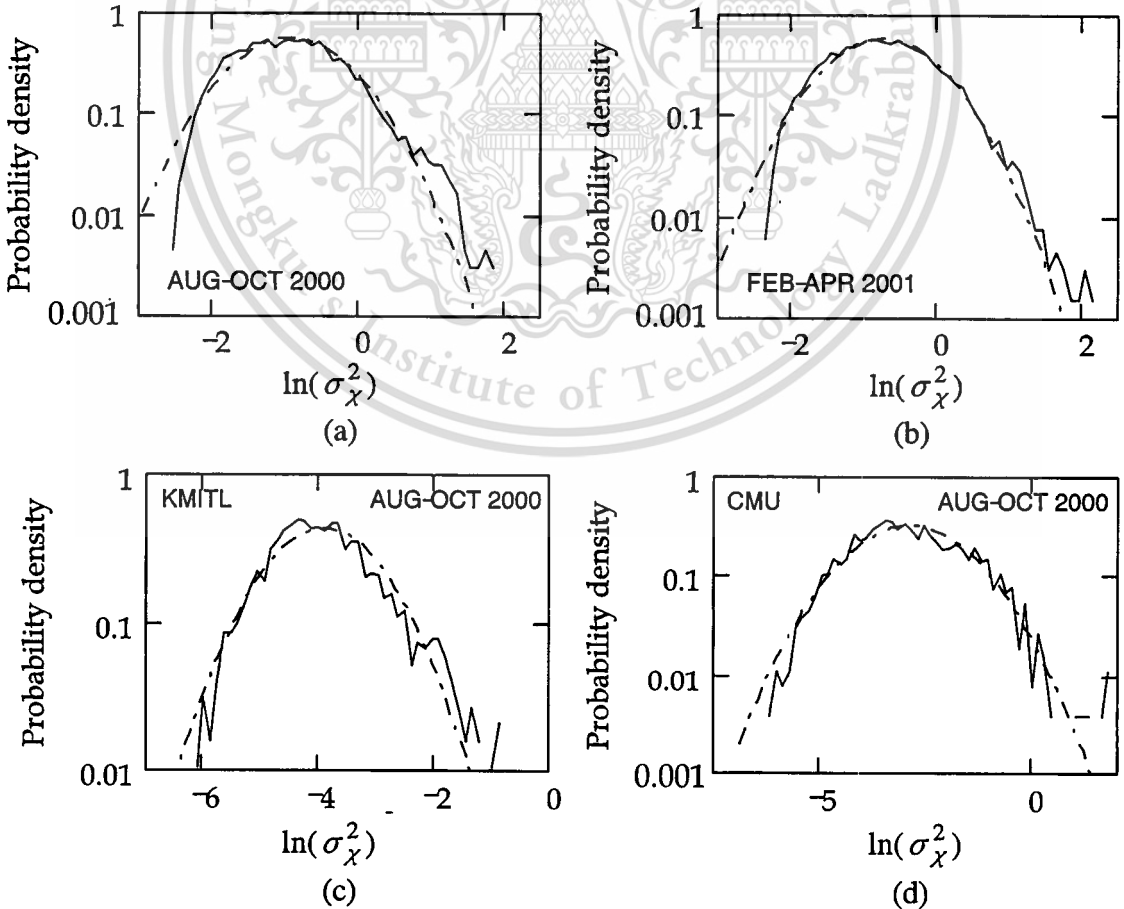


Fig. 6.1 Probability density function of log-scintillation variance $p(\ln \sigma_\chi^2)$

Fig. 6.1 (a) and (b) show the probability density function of $\ln(\sigma_\chi^2)$ for Aug. – Oct. 2000 and Feb. – Apr. 2001, plotted in red lines. The results have shown that these distributions are similar to the Gaussian PDF, black lines, with the mean values of -0.961 and -0.762 respectively. The parameters of σ_σ obtained from these two variances are $\sigma_\sigma = 0.718$ and 0.697 with the parameters of $\sigma_m = 0.618$ and 0.683 respectively. Also, for Fig. 6.1 (c) and (d) show the PDF of $\ln(\sigma_\chi^2)$ for Aug. – Oct. 2000 comparing between KMITL and CMU station by using 0.1 Hz data. The values of parameters are $\sigma_\sigma = 0.922$, $\sigma_m = 0.134$ and $\sigma_\sigma = 1.26$, $\sigma_m = 0.219$ for KMITL and CMU scintillation events respectively.

The long-term probability density function $p(\chi)$ of amplitude scintillation for autumnal equinox (August-October) in 2000, vernal equinox (February-April) in 2001 for 5 Hz scintillation data at KMITL; and 0.1 Hz scintillation data for comparison between two stations have been obtained by combining all 5 minutes scintillation events during this period. The parameters of σ_m and σ_σ can be obtained directly by all values of $\ln\sigma_\chi^2$ in each event as the results in Fig. 6.1 (a)-(d) respectively. As mentioned previously, from the results, the Gaussian distribution can not fit well with the long-term distribution of the experimental data, especially at both tails of the distribution. The Gaussian distribution form is limited by one constant value of the standard deviation for all amplitude fluctuation random values; in addition, its PDF's skewness is usually zero. Therefore, this model is unable to inform the long-term amplitude scintillation distribution especially for the fade and enhancement distributions. On the contrary, the PDF form of Moulslley-Vilar model can be observed to give a reasonable fit to the experimental distribution; however, according to the results in Fig. 6.2, this model underestimates the magnitudes of fades and overestimates the magnitudes of enhancements. These are the results of using the symmetrical model, based on Gaussian distribution as shown in Equation (6.4) and (6.5), to try and fit the experimental distribution which is slightly skew in the positive direction due to the large fading and small enhancement. From the results, the positive skewness can be observed in Fig. 6.2 (a) and (b), but the symmetrical model can be observed in Fig. (c) and (d). This is due to the lower re-sampling data that excludes the higher fade fluctuation, then the symmetrical distribution can be obtained.

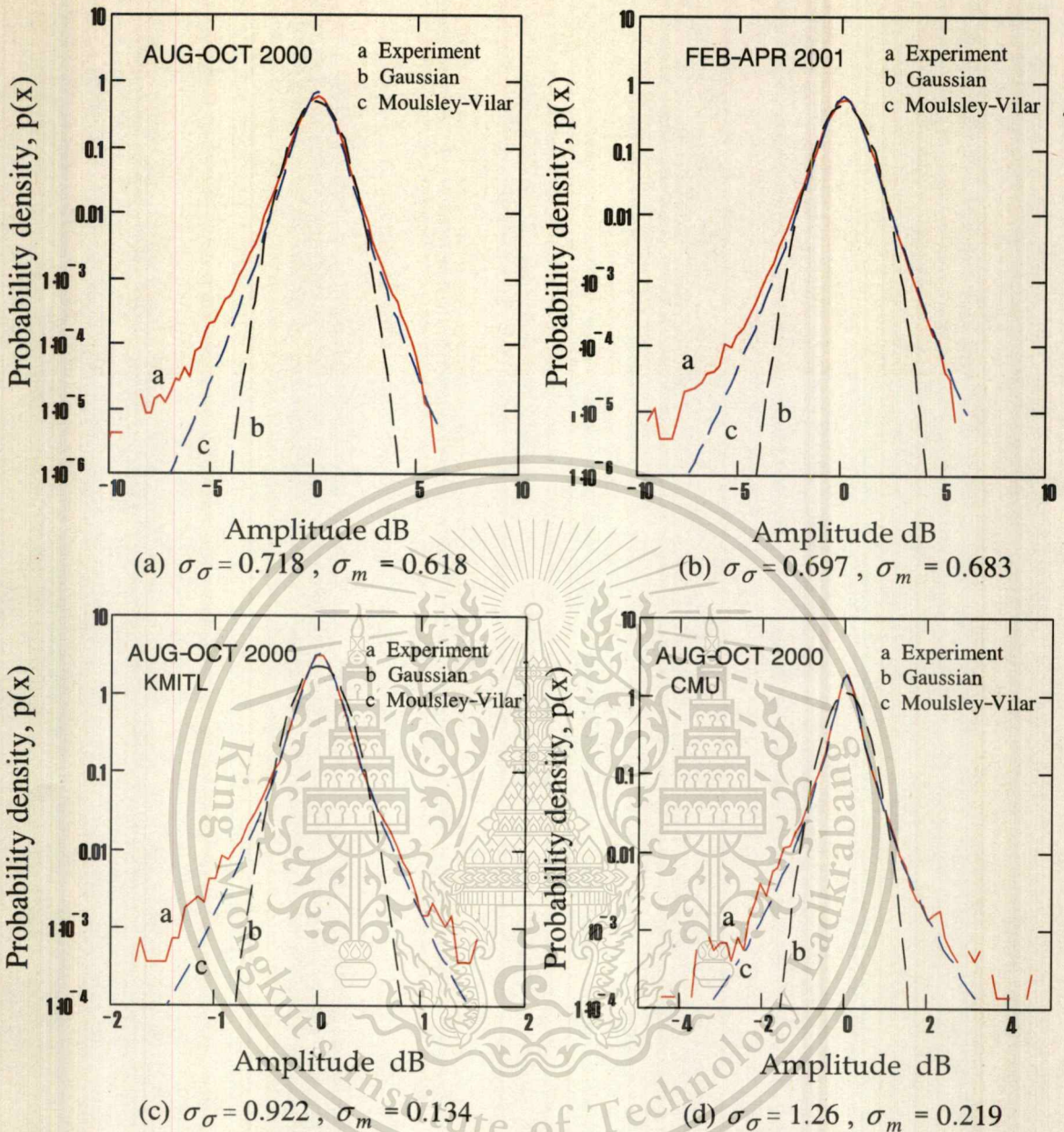


Fig. 6.2 Long - term probability density function $p(\chi)$ of scintillation amplitude

6.1.2 Analytical Approximation

Moulsey-Vilar model has been obtained by using Johnson-Su empirical distribution (Johnson. 1949), which is the four-parameter model. Suppose y is the random variation whose distribution has been expressed by

$$p(y) = \frac{\eta}{\sqrt{2\pi}} \frac{1}{\sqrt{(y-\varepsilon)^2 + \lambda^2}} \exp\left(-\frac{1}{2}\left(\gamma + \eta \ln\left[\left(\frac{y-\varepsilon}{\lambda}\right) + \sqrt{\left(\frac{y-\varepsilon}{\lambda}\right)^2 + 1}\right]\right)^2\right) \quad (6.9)$$

This material is reserved for educational use only, not allowed for commercial use.

Forbidden to modify the content, and cite the document when use.

where $\gamma, \eta, \varepsilon$ and λ are four parameters. The objective is to use the above expression to approximate $p(\chi)$ as given in section 6.1.1. However, the Mousley-Vilar model has zero mean, $\varepsilon = 0$, and zero skewness, $\gamma = 0$; and hence, $p(y)$ reduces to the two-parameter form dependent on just λ and η ; where

$$\eta = \left[\frac{1}{2} \ln \left[\sqrt{6 \exp \sigma_{\sigma}^2} - 2 - 1 \right] \right]^{-1/2}, \lambda = \sigma_m \left(2 \exp \left[\sigma_{\sigma}^2 / 2 \right] \right)^{1/2} \left(\exp \left[2 / \eta^2 \right] - 1 \right)^{-1/2} \quad (6.10)$$

Then the approximated formula for $p(\chi)$ can be obtained as following where $\chi = y - \varepsilon$.

$$\therefore p(\chi) \approx \frac{\eta}{\sqrt{2\pi(\chi^2 + \lambda^2)}} \exp \left[-\frac{[F(\chi)]^2}{2} \right] \quad (6.11)$$

where

$$F(\chi) = \eta \ln \left[\left(\frac{\chi}{\lambda} \right) + \left[\left(\frac{\chi}{\lambda} \right)^2 + 1 \right]^{1/2} \right] \quad (6.12)$$

The goodness of fit of this approximate formula to the actual Mousley-Vilar distribution in Equation (6.8) can be observed by the next results.

Fig. 6.3 presents the comparison of the long-term probability density models of scintillation events corresponding to Fig. 6.2. Gaussian distribution, Mousley-Vilar model and analytical approximation are compared with the experimental distribution. Gaussian distribution has the standard deviation values of 0.797, 0.815, 0.179 and 0.36 respectively. These Mousley-Vilar and analytical models have the positive skewness with the amplitude fluctuation between $-10 - 6$ dB for only Fig. 6.3 (a) and (b). The analytical approximation has the very good fitting with the Mousley-Vilar model for enhancement, but has the small difference in fade. It fits in fade with the experimental distribution well than the Mousley-Vilar model as the results in Fig. 6.3 (a) and (b). But for Fig. 6.3 (c) and (d), these two models have the very good fitting without any difference. Similarly to the previous reason, these are related with the rough sampling scintillation data. Moreover these might seem to be that these two

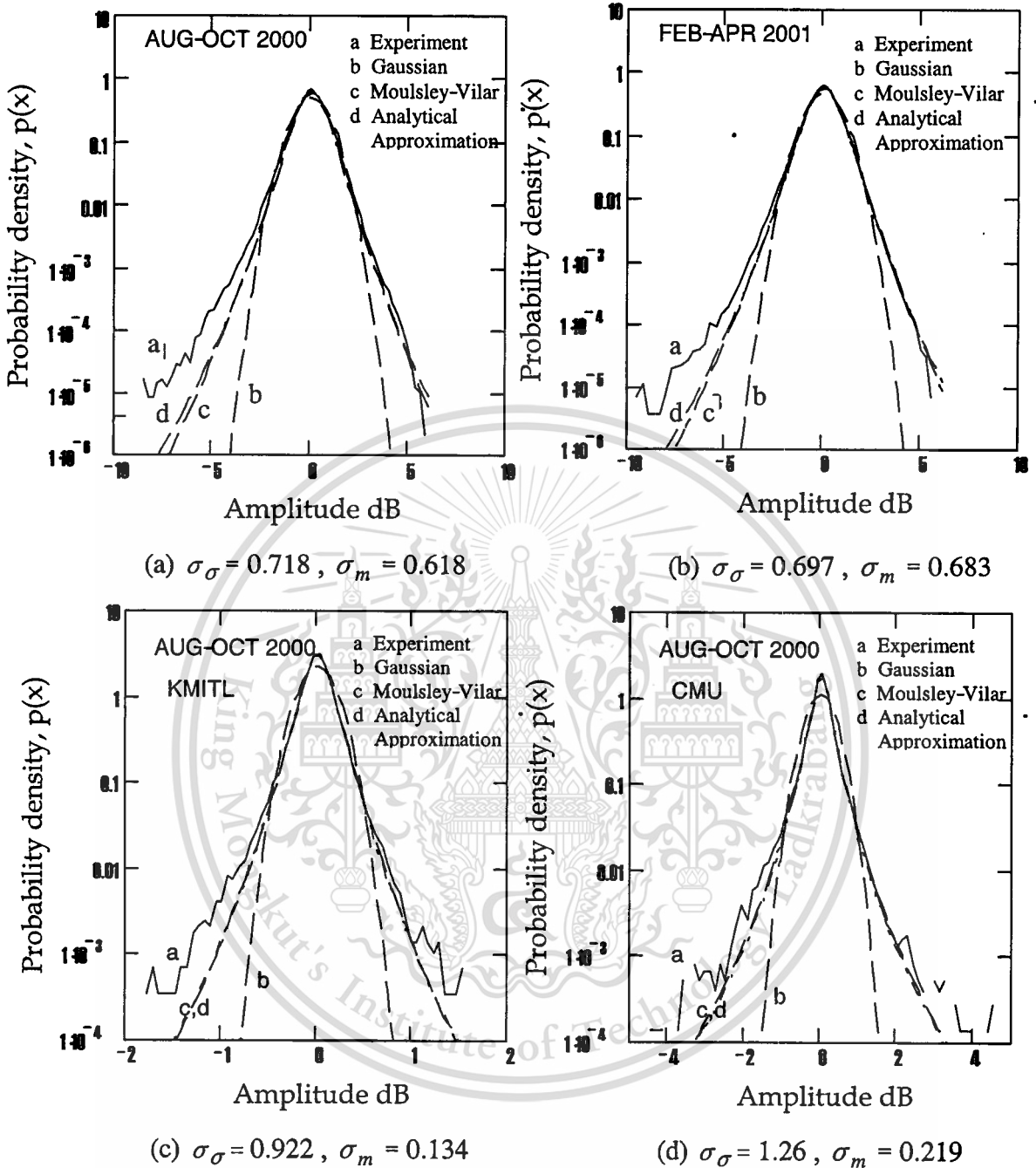


Fig. 6.3 Comparison of all long-term probability density function models

models are suitable for weak to moderate scintillation; the model curves fit well with each other at the low levels fluctuation (within ± 4 dB). For stronger fluctuation levels, these two-model curves start to separate. Nevertheless, these two probability density models are considered to be good enough for using in system design and obtaining the rough estimation of the effects of scintillation on communication link performance.

6.2 Channel Capacity in Scintillation Channel

Channel capacity is the maximum rate at which reliable transmission of information over the channel is possible. This denotes not only the physical medium over which transmission take place but also the various parts of transmitter and receiver. Channel capacity varies with the changes in propagation medium; or can mention that it is related to the stochastic properties of the fading process. The scintillation fading process is considered in this study.

The capacity, C for the continuous channel with additive white Gaussian noise can be given by Shannon's expression (Proakis. 2001).

$$C = B \log_2 \left(1 + \frac{S}{N} \right) \quad (\text{b/s}) \quad (6.13)$$

where B is the channel bandwidth in Hz, and S/N is the signal-to-noise power ratio in the channel. In order to make the analysis independent of the actual bandwidth of the channel, Equation (6.13) can be written as

$$\frac{C}{B} = \log_2 \left(1 + \frac{S}{N} \right) \quad \left(\frac{\text{b/s}}{\text{Hz}} \right) \quad (6.14)$$

The term C/B is the channel capacity per unit bandwidth. If considering the scintillation fading, the term S/N is random variable with its distribution corresponding to scintillation. Then the random channel capacity can be determined using those of S/N , or equivalently, those of scintillation fading process.

According to Equation (6.14), hence the transformations can be obtained by (Filip and Vilar. 1990).

$$f(x) = y = a \ln(1 + x) \quad (6.15)$$

where $y = C/B$, $x = S/N$ and $a = (\ln 2)^{-1}$. From the conventional probability theory in Equation (6.6), the probability density function of y , $p_Y(y)$ can be determined.

where $p_X(x)$ is the probability density function of random S/N due to scintillation fading as the probability density function in Equation (6.8). Then we can obtain

$$p_Y(y) = \frac{1}{a} \exp\left(\frac{y}{a}\right) \cdot p_X\left(\exp\left(\frac{y}{a}\right) - 1\right) \quad (6.16)$$

In some conditions, it may be more convenient to deal with the cumulative distribution function instead as given by

$$\begin{aligned} F_Y(y) &= \Pr\{Y \leq y\} = \int_0^y p_Y(u) du \\ &= \Pr\{X \leq f^{-1}(y)\} = \int_R p_X(v) dv \end{aligned} \quad (6.17)$$

where $f^{-1}(y) = \exp\left(\frac{y}{a}\right) - 1$; $a > 0, y > 0$. R denotes the region of $p_X(x)$ corresponding to the values of $X \leq f^{-1}(y)$. Then Equation (6.17) becomes

$$F_Y(y) = \int_0^{\exp(y/a)-1} p_X(x) dx \quad (6.18)$$

If consider the scintillation fading process, its PDF in Equation (6.8) and (6.11) will be taken in to account. The received signal-to-noise power ratio in the presence of scintillation is then given by

$$\frac{S}{N} = \frac{S}{N_0} + L_\chi \quad [\text{dBW}] \quad (6.19)$$

where $L_\chi = 8.686\chi$. The long-term probability density function of amplitude scintillation $P(\chi)$ has the form of (6.8) and (6.11). From Equation (6.17) and (6.18), the cumulative distribution function of channel capacity can be written as

$$\begin{aligned}
F_{C/B}(y) &= \Pr\left\{\frac{C}{B} \leq y\right\} = \Pr\left\{\frac{S}{N} \leq f^{-1}(y)\right\} \\
&= \Pr\left\{L_x \leq f^{-1}(y) - \frac{S}{N_0}\right\} = F_{L_x}\left(f^{-1}(y) - \left(\frac{S}{N_0}\right)\right) \\
&= \int_0^{(\exp(y/a)-1)-S/N_0} p_L(x) dx \tag{6.20}
\end{aligned}$$

The long-term cumulative distribution function of channel capacity ($F_{C/B}$) is plotted in both linear and logarithmic scale as presented in Fig. 6.4 and 6.5 respectively. The dotted lines indicate the cumulative distribution function of the channel capacity in case of unfaded signal-to-noise ratio in the channel. The CDF for this non-stochastic case forms the step function given directly by Equation (6.14) with unfaded signal-to-noise ratio values $S/N_0 = 10, 15, 20$ and 25 dB as shown in Fig. 6.4. Long-term probability density of Moulisley-Vilar model and the analytical approximation are used to determine the channel capacity. For linear scale, the distinction between channel capacity obtained by both models can not be determined; but only the difference at the small percentages (corresponding to the difference at the fade of scintillation model, see Fig. 6.3) can be observed in the logarithmic scale. The rapid reduction of capacity for small percentages of the time at 0.01 ($F_{C/B} < 0.01$ or 1%) can be seen more clearly in Fig. 6.5. Furthermore, the capacities are greater than those of the free space case of Shannon channel capacities (dash line) at 40 % of time for $S/N_0 = 10$ and 15 50 % for $S/N_0 = 20$ dB; but about 20% of time for $S/N_0 = 25$ dB. However, the last two channel capacities are close to the free space channel capacities as the step function; then the percentage of time of the channel capacities for scintillation process that are greater than free space cases can not absolutely specified. These greater capacities than free-space cases might seem to be due to the scintillation enhancements.

When considering the secure operation for the M-PSK modulation with the BER not greater than 10^{-7} , the minimum channel (or threshold) capacities required to these

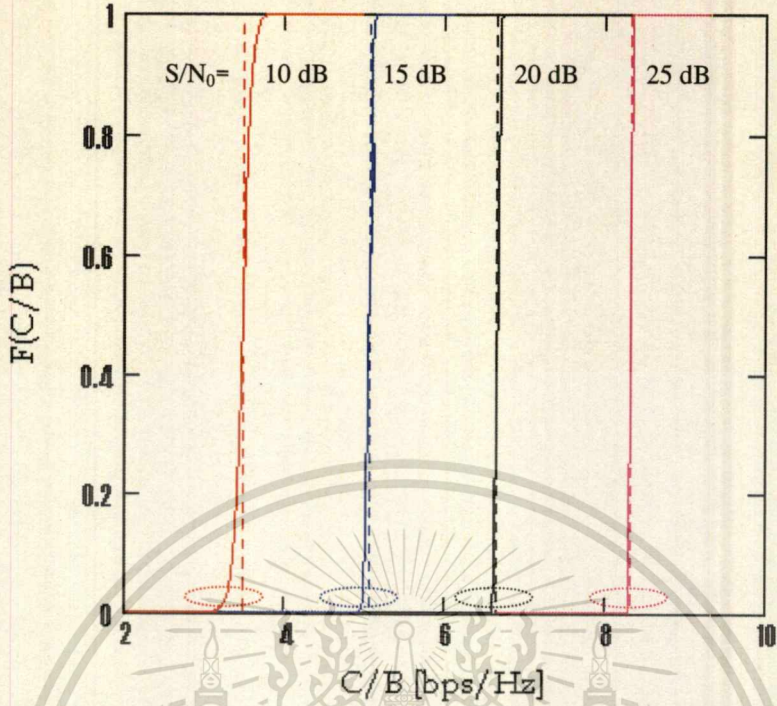


Fig. 6.4 Cumulative distribution function of channel capacity of scintillation channel compared with free space case (linear scale)

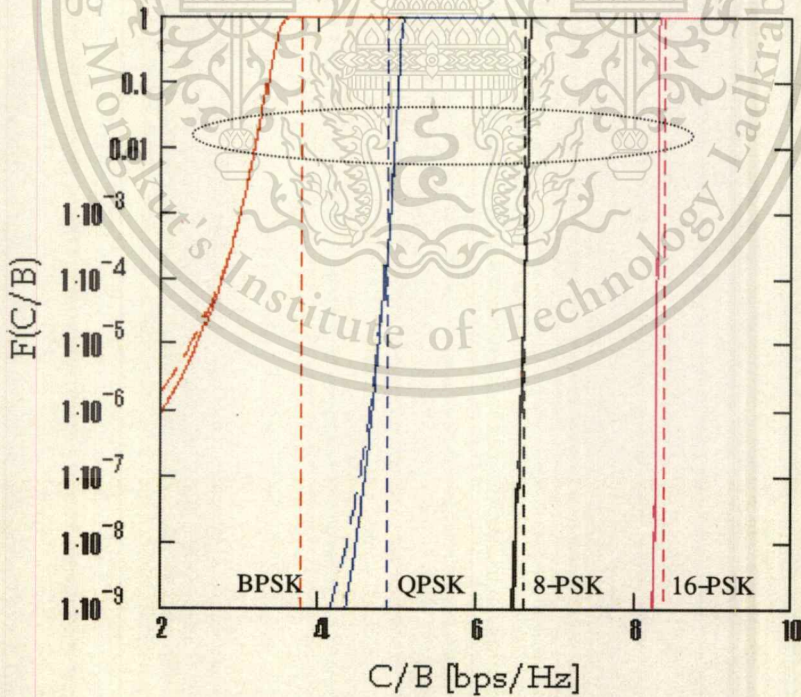


Fig. 6.5 Cumulative distribution function of channel capacity of scintillation channel compared with the minimum capacity for M-PSK system (logarithmic scale)

with $S/N_0 = 10, 15, 20$ and 25 dB for BPSK, QPSK, 8-PSK and 16-PSK respectively, for BER of 10^{-7} (Feher. 1987). The results have shown that the threshold capacity of 16-PSK is exceeded for approximately 6 percentage of time, or not exceeded for 0.94 on the cumulative basis. This means that the channel is theoretically capable to operate with 16-PSK for 6 percentage of time. On the other hand, the channel rarely can operate with BPSK since its capacity exceeds the required minimum capacity approximately only 0.11 %. For QPSK and 8-PSK, the channel can operate about 100 % under scintillation fading.

If consider the digital satellite link with unfaded $S/N_0 = 25$ dB, the maximum attainable channel capacity limited by the unfaded S/N_0 value would approximately be 8.3 b/s/Hz. If, for example, the modulation that is allowed to use is only uncoded PSK for BER not greater than 10^{-7} . It is clear that all we could use are BPSK, QPSK or 8-PSK. But 16-PSK requires the C/B of 8.4 b/s which is greater than the limitation, 8.3 b/s/Hz.

6.3 Estimation of Bit Error Probability during Scintillation

From the previous section, the results have shown that the Moulslley-Vilar distribution or the analytical approximation form is good enough for practical purposes to determine the system impacts of ionospheric scintillation. Therefore, using this long-term amplitude scintillation distribution can predict the average bit error probability of a digital satellite link. According to the section 6.1, the model gives the probability density of log amplitude fluctuation in decibel as $\chi = 20(\log_{10} A - \log_{10} A_0)$. The signal-to-noise ratio, γ can be given by the following equation with the relation to the amplitude fluctuation, where N is the additive white Gaussian noise power (AWGN) in the radio bandwidth assuming to be constant.

$$\gamma = \frac{A^2}{2N} \quad (6.21)$$

The variation in γ is taken to be due to the variation of A caused by the scintillation process; but for non-scintillation process $\gamma_0 = A_0^2/2N$. From Equation

This material is reserved for educational use only, not allowed for commercial use.

Forbidden to modify the content, and cite the document when use.

(6.2), we can obtain the relation of $\chi = 10 \log(A^2/A_0^2)$, then the relation between the amplitude fluctuation, χ and signal-to-noise ratio, γ can be written as:

$$\chi = 10 \log \left(\frac{\gamma}{\gamma_0} \right) \quad (6.22)$$

$$\therefore \gamma = \gamma_0 10^{\frac{\chi}{10}} \quad (6.23)$$

When assuming the theoretical optimum detection, γ is also equal to the energy (per bit) to noise density ratio, (E_b/N_0) .

The probability of bit error for a given γ is $P_b(\gamma)$. Because of the scintillation process makes the variables γ to be random, therefore in order to estimate the bit error probability, the average E_b/N_0 and the average probability of bit error should be considered by taking the expectations of $\langle E_b/N_0 \rangle$ and $\langle P_b \rangle$ over the whole fading process. Therefore, the average probability of bit error and the average E_b/N_0 can be given as followed (Banjo and Vilar. 1985).

$$\langle P_b \rangle = \int_{-\infty}^{\infty} P_b(Z(u)) I(u) du \quad (6.24)$$

$$\langle \gamma \rangle = \int_{-\infty}^{\infty} Z(u) I(u) du \quad (6.25)$$

where $Z(u) = \gamma = \gamma_0 10^{\frac{\chi}{10}}$ and $I(u) = p(\chi)$. However, according to the previous sections (6.1 and 6.2), the distinction between using Mousley-Vilar model and the analytical approximation can not be observed obviously. Therefore, only Mousley-Vilar scintillation model will be taken into account with $I(u)$ for the estimations in Equation (6.24) and (6.25).

Three types of modulation formats have been considered here to illustrate the principles. These are binary coherent phase-shift-keying (CPSK), binary noncoherent

This material is reserved for educational use only, not allowed for commercial use.

Forbidden to modify the content, and cite the document when use.

frequency-shift-keying (NCFSK) and direct-sequence spread spectrum (DS-SS) systems. The theoretical probability of bit error due to AWGN as a function of E_b/N_0 , γ , (Sklar. 1988) for:

CPSK modulation:
$$P_b(\gamma) = \frac{1}{2} \operatorname{erfc}(\sqrt{\gamma}) \quad (6.26)$$

from
$$Q(x) = \frac{1}{\sqrt{2\pi}} \int_x^{\infty} \exp(-t^2/2) dt = \frac{1}{2} \operatorname{erfc}\left(\frac{x}{\sqrt{2}}\right) \quad (6.27)$$

hence
$$\langle P_b \rangle_{\text{CPSK}} = \frac{1}{2} \int_{-\infty}^{\infty} (\operatorname{erfc}(\sqrt{\gamma_0} 10^{20} \frac{x}{\sqrt{2}})) p(x) dx$$

or
$$= \frac{1}{2} \int_{-\infty}^{\infty} Q(\sqrt{2\gamma_0} 10^{20} \frac{x}{\sqrt{2}}) p(x) dx \quad (6.28)$$

NCFSK modulation:
$$P_b(\gamma) = \frac{1}{2} \exp\left(-\frac{\gamma}{2}\right) \quad (6.29)$$

hence
$$\langle P_b \rangle_{\text{NCFSK}} = \frac{1}{2} \int_{-\infty}^{\infty} \exp\left(-\frac{\gamma_0 10^{10} x^2}{2}\right) p(x) dx \quad (6.30)$$

For a multi-user binary DS-SS system, the i^{th} user's conditional bit error probability (\overline{BER}_i) for a binary coherent (CPSK) modulation can be obtained under the Gaussian approximation as (Glisic and Vucetic. 1997 ; Proakis and Salehi. 1997)

$$P_{b_i}(\gamma) = \overline{BER}_i(\gamma) = Q(\overline{SNR}_i(\gamma)) \quad (6.31)$$

from (6.23) and the i^{th} user's average conditional signal-to-noise ratio $\overline{SNR}_i(\gamma)$ is

$$\overline{SNR}_i(\chi) = \left(\frac{R_i^K}{6N^3} + \frac{1}{2\gamma_0 10^{\frac{\chi}{10}}} \right)^{\frac{1}{2}} \quad (6.32)$$

where $R_i^K \approx (K-1)/2N^2$ is the total interference parameter caused by the other $K-1$ codes and N is the processing gain. For overall system performance, the average probability of bit error is considered for an average user for which the total interference parameter is equal to $R_{av}^K = \frac{1}{K} \sum_{i=1}^K R_i^K$, hence $\overline{SNR}_{av}(\chi)$

$$\overline{SNR}_{av}(\chi) = \left(\frac{\sum_{i=1}^K (K_i - 1)}{3N^2} + \frac{1}{2\gamma_0 10^{\frac{\chi}{10}}} \right)^{\frac{1}{2}} \quad (6.33)$$

hence

$$\langle P_b \rangle_{DS-SS} = \langle BER_{av} \rangle = \int_{-\infty}^{\infty} Q(\overline{SNR}_{av}(\chi)) p(\chi) d\chi \quad (6.34)$$

Finally, the average probability of bit error in Equation (6.28), (6.30) and (6.34) have been plotted versus the average signal-to-noise density ratio, (6.25), as given by

$$\langle E_b/N_0 \rangle = \langle \gamma \rangle = \gamma_0 \int_{-\infty}^{\infty} 10^{\frac{\chi}{10}} p(\chi) d\chi \quad (6.35)$$

Fig 6.6 shows the approximated $\langle P_b \rangle$ plotted against $\langle \gamma \rangle$ (using Moulsey-Vilar model for $P(\chi)$) under the condition of various values of σ_m , but the parameter $\sigma_\sigma = 0$ for the CPSK and NCFSK modulation formats. The solid lines present the average probability of bit error for CPSK modulation; and the dash lines present for NCFSK modulation. Comparison with the non-scintillating cases in curve a and e shows the increases in $\langle P_b \rangle$ due to the increases of scintillation intensity indicated by parameter σ_m . Fig. 6.7 presents the average probability of bit error for scintillation obtained from the experiment. Using the parameters $\sigma_\sigma = 0.718$, $\sigma_m = 0.618$ for

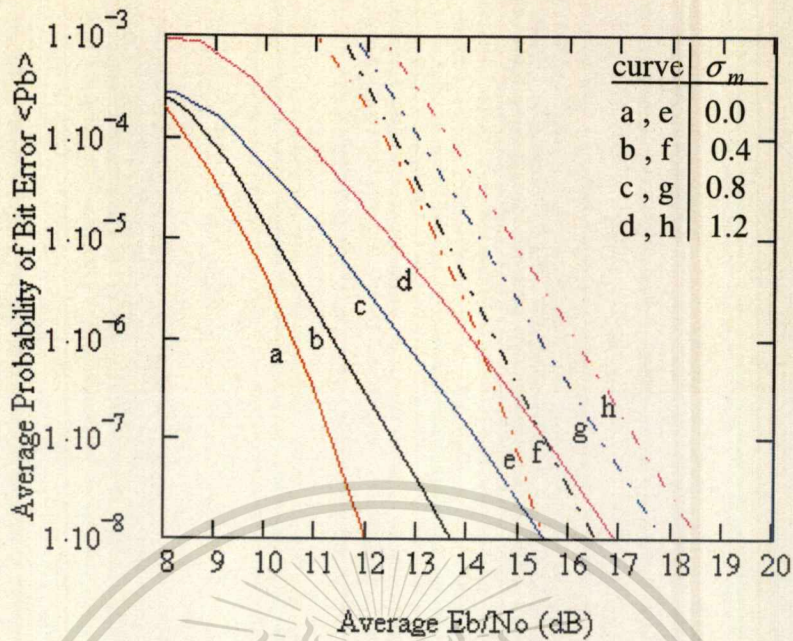


Fig. 6.6 Average BER for nonvariable scintillation intensity ($\sigma_\sigma = 0, \ln \sigma_m^2 = \overline{\ln \sigma_\chi^2}$) for CPSK (solid line) and NCFSK (dash-dot line) modulation techniques

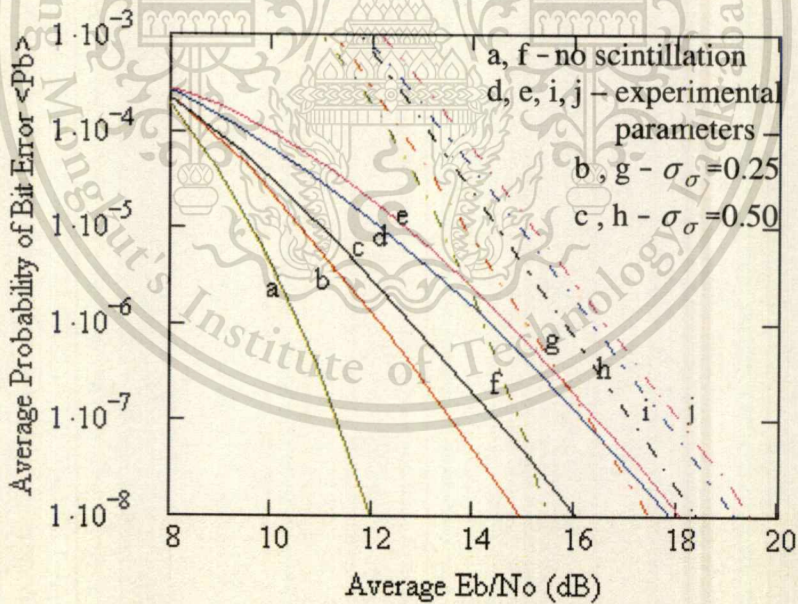


Fig. 6.7 Average BER for variable scintillation intensity $\sigma_m = 0.5, \sigma_\sigma = 0.25, 0.5$

$\sigma_\sigma = 0.718, \sigma_m = 0.618$ (curve d, i) and $\sigma_\sigma = 0.697, \sigma_m = 0.683$ (curve e, j)

Moulsley-Vilar model $P(\chi)$, then the average probability of bit error can be obtained as shown in curve d and i, and using parameters $\sigma_\sigma = 0.697, \sigma_m = 0.683$ for curve e

This material is reserved for educational use only, not allowed for commercial use.

Table 6.1 E_b/N_0 degradation for various scintillation conditions

Modulation Technique	Condition		E_b/N_0 degradation at BER= 10^{-6} (dB)
	σ_m	σ_σ	
CPSK (b)	0.5	0.25	1.70
CPSK (c)	0.5	0.50	2.45
CPSK (d)	0.618	0.718	4.21
CPSK (e)	0.683	0.697	4.53
NCFSK (g)	0.5	0.25	0.78
NCFSK (h)	0.5	0.50	1.55
NCFSK (i)	0.618	0.718	2.05
NCFSK (j)	0.683	0.697	2.31

and j corresponding to models in Fig. 6.2 (a) and (b) respectively. The performance degradation can be expressed in term of the increase in average $E_b/N_0, \langle \gamma \rangle$ which is required for taking the $\langle P_b \rangle$ values under scintillation fading to the same values as for the unfaded situation. Table 6.1 shows the examples of the performance degradation from non-scintillation cases (curve a and f) at the average BER of 10^{-6} for various conditions corresponded to Fig. 6.7.

The results of the average BER for DS-SS system effected by scintillation presents in Fig. 6.8- 6.10. The effect of scintillation on the system with a fixed number of active users, $K = 20$ and processing gain, $N = 511$ has been estimated here as the results in Fig. 6.8 and 6.9. In Fig. 6.8, the performance curves (b, c, d) are plotted in case of increasing scintillation intensity at the fixed parameter $\sigma_\sigma = 0$, compared with the non-scintillation case (curve a), similarly to Fig. 6.6. As can be expected, the average probability of bit error increases as σ_m increases. Fig. 6.9 illustrates the degradation of the performance by keeping long-term standard deviation constant σ_m at 0.5 and increasing parameter σ_σ instead. Similarly to the CPSK and NCFSK system, the results show the worse degraded performance for the increasing of σ_σ .

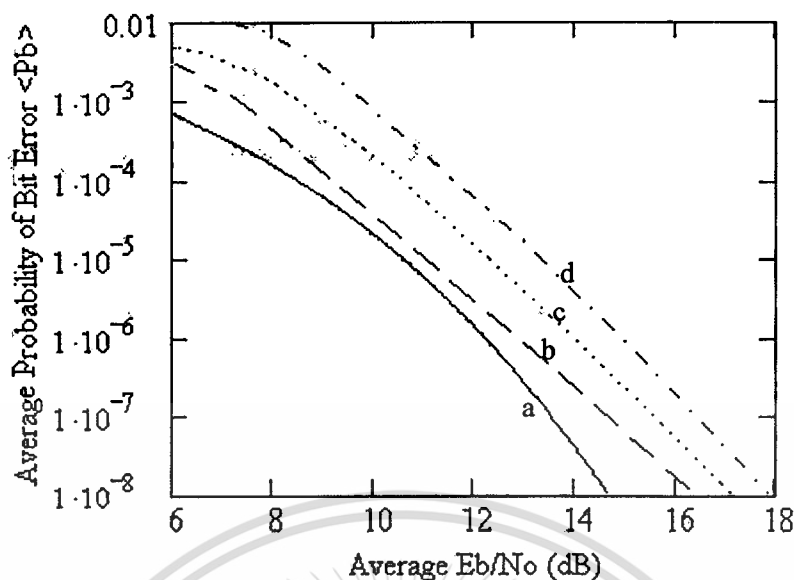


Fig. 6.8 Average BER for nonvariable scintillation intensity ($\sigma_\sigma = 0$) for DS-SS technique with (a) $\sigma_m = 0$; (b) $\sigma_m = 0.4$, (c) $\sigma_m = 0.8$ and (d) $\sigma_m = 1.2$

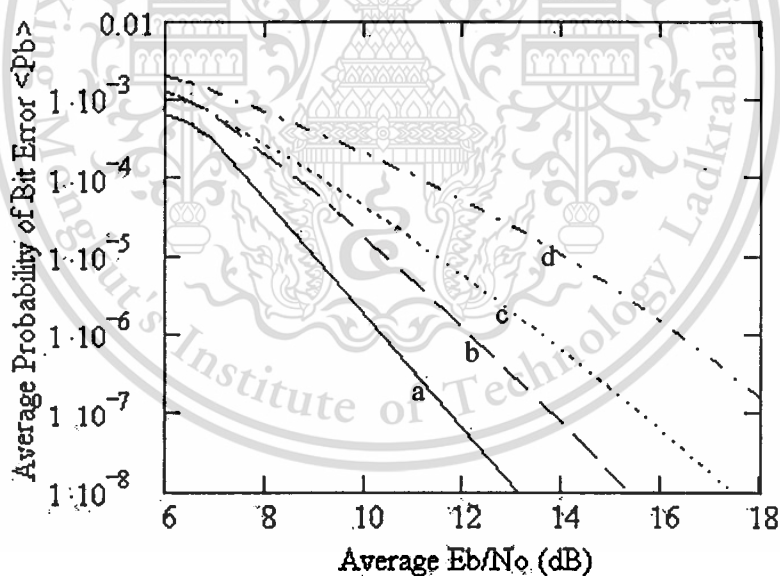


Fig. 6.9 Average BER for variable scintillation intensity for DS-SS technique with $\sigma_m = 0.5$ and (a) $\sigma_\sigma = 0$, (b) $\sigma_\sigma = 0.5$, (c) $\sigma_\sigma = 0.75$ and (d) $\sigma_\sigma = 1$

Furthermore, if consider the impact of scintillation on DS-SS channel with the variable number of active users, the average total interference parameter R_{av}^K is evaluated for different values of K user. Fig. 6.10 shows the performance achieved for the average user operating when, respectively, 1, 15, 30 and 50 users

simultaneously access the free fading channel (dash line) and the scintillating channel (solid line) with the parameters of scintillation model $P(\chi)$, $\sigma_\sigma = 0.697$ and $\sigma_m = 0.683$. The results have shown that as the active user increases, the degradation of the average $E_b/N_0, \langle \gamma \rangle$, decreases. As an example, the degradation of E_b/N_0 for the average BER of 10^{-6} is 0.8 dB for 50 active users, 1 dB for 30 active users, 1.2 dB for 15 users and 1.4 dB for the single user case.

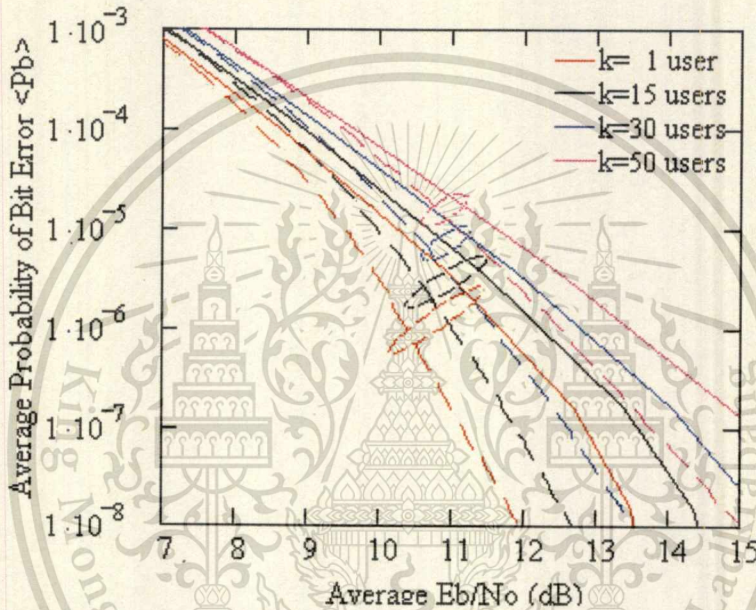


Fig. 6.10 Average BER for different numbers of active users
($\sigma_\sigma = 0.697$ and $\sigma_m = 0.683$)

6.4 Conclusion

This chapter presents the long-term probability density function of amplitude scintillation approximated by Moulslley-Vilar model and the analytical approximation using rms scintillation intensity parameters, σ_m and σ_σ . The very good fitting between these two models can be observed except at the fade site; the analytical fitting is a little bit higher than Moulslley-Vilar fitting. These long-term models fit well with the experimental amplitude distribution when comparing with the Gaussian distribution. σ_m and σ_σ are the important parameters of scintillation model; and used for the theoretical approximation of system performance. The long-term

This material is reserved for educational use only, not allowed for commercial use.

statistical model of the satellite channel capacity is also derived here for the examples of M-ary PSK modulation schemes. Although, the results show that there is no difference so much between scintillation and free-space cases of channel capacity; they can present a wider view of what the system can achieve, and the percentage of time that system can operate under scintillation with the suitable modulation techniques.

Moreover, using scintillation model can predict the system outage time due to scintillation. Theoretical estimation of the average probability of bit error for a digital satellite link subject to scintillation fading are presented for CPSK, NCFSK and DS-SS modulation techniques. The results show that the performance is expected to degrade as the scintillation intensity increases (increasing values of σ_m with the fixed value of σ_σ), and to be worse with the variability of scintillation intensity (variability of σ_σ with σ_m is fixed). For DS-SS modulation technique, additionally, the increasing of active users induces the decreasing of the degradation. This means that scintillation does not predominately effect this system when many numbers of asynchronous users are simultaneously accessing the communication channel. But the degradation is predominated by co-channel interference instead.

CHAPTER 7

CONCLUSION

7.1 Summary of the Preceding Chapters

This thesis is concerned with the characteristics of the ionospheric scintillation. The morphological results show the diurnal and seasonal variation of scintillation occurrences. The nighttime scintillation usually occurs around 18.00-02.00 LT. Some occurrences in daytime can be observed due to the daytime electrojet irregularities. The scintillation intensity varies seasonally corresponding to the average TEC and solar activity in vernal and autumnal equinox periods. When considering the ionospheric scintillation for different geomagnetic latitudinal location, the scintillation intensity occurred at CMU is more than KMITL. This might seem to be that the location of CMU is closer to the equatorial anomaly than KMITL location. Consequently, the higher scintillation intensity and more scintillation occurrences can be observed here. Therefore, particularly in the equatorial region, the location closer to the equatorial anomaly zones ($\pm 15^\circ$ geomagnetic latitude) has stronger scintillation than other locations farther from these zones, although the equatorial position.

The amplitude scintillation can inform the irregularities characteristics by its frequency and time structures. The PSD obtained by FFT has many important parameters such as spectral index, Fresnel frequency and etc. The linear increasing of the power spectral index as time increasing indicates the rapid dissipation of small scale irregularities for later scintillation events. Spectral index also relates to the S_4 index; it increases as the scintillation intensity increases. On the other hand, the decorrelation time, τ , obtained by the autocorrelation function has the inverse dependence on S_4 . Its rapid decreasing for strong scintillation can signify the fast decorrelation of the signal. τ gradually increases its value before midnight time corresponding to the irregularities movement in nighttime. The halt of the irregularities can be informed by the decreasing τ immediately around midnight. However the reversal movement is also observed when the value of τ increases itself again relates to the movement of the irregularities to westward direction. Comparing with PSD, the broadening of PSD becomes wider when τ is small. The best linear regression fit of data set has the linear relation given by $y = mx + b$; where y is the

main parameter such as spectral index, n , or τ ; x is the S_4 index or local time variation; finally, m is the slope and b is the intercept. This linear regression informs the characteristics of scintillation under normal condition (nighttime scintillation). The scintillation fade rate can be estimated by the 3-dB corner frequency, τ and the mean crossing technique. But the scintillation rates obtained from these do not agree well with each other. Moreover, the decorrelation time τ is also used to multiply with the velocity of the irregularities; then the ground decorrelation distance can be obtained and used for space-diversity antenna or the multipoint observations.

The instantaneous amplitude scintillation has the good fitting with the Gaussian and Nakagami- m distribution. The Gaussian distribution fits well with the enhancement side; while as the fade side is related to the Nakagami- m distribution. From the morphological results, the ionospheric scintillation characteristics of this site are weak-to-moderate scintillation with that the Gaussian distribution is suitable for fitting. The communications effected by ionospheric scintillation can be obtained such as the CDF of amplitude scintillation, receiver dynamic range and the fade analysis. The fade duration and the numbers of fade when signal exceeding the specific fade level can inform the effects of scintillation on communication well than inform by the scintillation intensity or the amplitude fluctuation. The percentage of the message perfectly received, estimated by the fade duration can present the possibility of the lost communication. For long-term scintillation, the scintillation channel modeling is estimated, based on the Gaussian distribution, by Mousley-Vilar model and the analytical approximation. These two models depend on the important parameters σ_m and σ_σ ; while as the Gaussian distribution depends on the mean value and the standard deviation. The long-term distribution of scintillation data fits well with these scintillation channel models when compare with the Gaussian distribution.

σ_χ in $p(\chi|\sigma_\chi)$ can be obtained over 5 minutes interval; but σ_m and σ_σ in $p(\chi)$ can be obtained by the whole data set. The parameter σ_m depends on the data sets of the intensity of scintillation intensity, σ_χ . And the condition of σ_σ for constant scintillation intensity, σ_χ , is equal zero; and others for various values of σ_χ . However, this variability parameter, σ_σ , for the earth-space path has been suggested practically in the range between 0.5 to 1.5. Furthermore, the theoretical

This material is reserved for educational use only, not allowed for commercial use.

Forbidden to modify the content, and cite the document when use.

approximation of system performance can be estimated; such as satellite channel capacity for M-PSK system, the average probability of bit error for CPSK, NCFSK and DS-SS systems. These performances depend on the parameters of σ_m and σ_σ . The performance degrades as the scintillation increases (increasing values of σ_m with the fixed value of σ_σ); and to be worse with the variability of scintillation intensity (variability of σ_σ with σ_m is fixed). For DS-SS system, many active users are able to improve the system from scintillation effects but the system degradation can be predominated by co-channel interference instead.

7.2 Remark for the Future Research

According to the preceding chapters, three points should be considered for the future research.

a) In view of the different geomagnetic latitude position, all scintillation characteristics should be analyzed for both stations. This research has the problem about raw data access for CMU station, therefore only 0.1 Hz scintillation data have been analyzed and compared the results with 0.1 Hz data of KMITL station. However for frequency-time structure analysis, only 5 Hz re-sampled scintillation data (KMITL) have been analyzed. In order to obtain the characteristics of scintillation for different location corresponding to the irregularities movement, more information about the decorrelation distances, the decorrelation time, the spectral index, etc. corresponding to the CMU station should be analyzed with 5 Hz re-sampled data.

b) This thesis presents the results of the receiver dynamic range for only some scintillation events. However, for good system design of scintillation characteristics at each station, the receiver dynamic range of every segment of all scintillation events should be determined and averaged to obtain the appropriate range for that station.

c) These scintillation characteristics can be mentioned that it is the weak-to-moderate scintillation; then the scintillation channel modeling is based on the Gaussian distribution. However, the strong scintillation can occur in sometimes. In this case, Mousley-Vilar model and the analytical approximation do not agree well with the experimental data especially at the fade side. Therefore, for strong fluctuation of scintillation, the scintillation channel modeling should be considered and proposed based on the Nakagami-m distribution instead.

This material is reserved for educational use only, not allowed for commercial use.

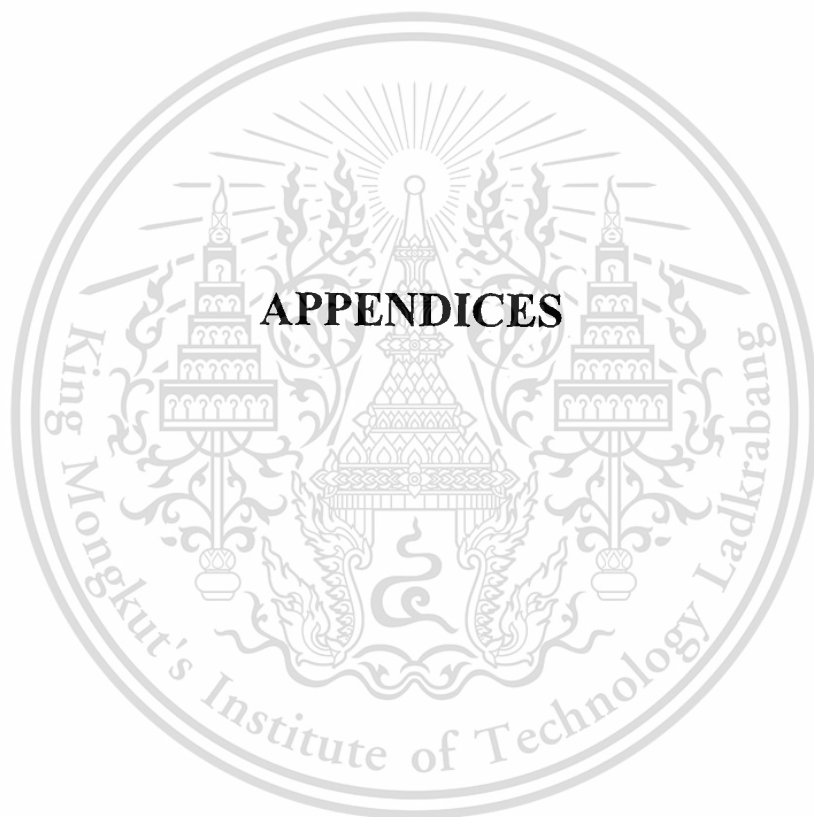
Forbidden to modify the content, and cite the document when use.

BIBLIOGRAPHY

- Aarons, J. 1982. "Global Morphology of Ionospheric Scintillations." **Proceedings of the IEEE.** 70(4) : 360-378.
- Allnutt, J.E. 1989. **Satellite -to-ground Radiowave Propagation Theory, Practice and System Impact at Frequencies Above 1 GHz.** London,U.K. : Peter Peregrinus Ltd.
- Anderson, D.N. and Klobuchar, J.A. 1983. "Modeling the Total Electron Content observations above Ascension Island." **J. Geophys. Res.** 88 : 8020-8024.
- Banerjee, P.K. et. al. 1992 "C and L band Transionospheric Scintillation Experiment : Some Results for Applications to Satellite Radio System." **Radio Science.** 27(6):955-969.
- Banjo, O.P. and Vilar, E. 1986. "Binary Error Probabilities on Earth-Space Paths Subject to Scintillation Fading." **Electron. Lett.** 21(7) : 296-297.
- Basu, S. and Basu, Su. 1981. "Equatorial Scintillations : A Review." **J.Atmos. Terr.Phys.** 43 : 473.
- Basu, S. et. al. 1988. "Ionospheric constraints on VHF/UHF Communication Links During Solar Maximum and Minimum periods." **Radio Science .** 23(3) : 363-378.
- Bhattacharyya, A. et. al 1992. "Deducing Turbulence Parameters from Transionospheric Scintillation Measurements ." **Space Science Reviews.** 61:335-386.
- Booker, H.G. 1975. "The Role of the Magnetosphere in Satellite and Radio-Star Scintillation." **J. Atmos. Terr.Phys.** 37 : 1089-1098.
- Briggs, B.H. and Parkins, I.A. 1963. "On the Variation of Radio Star and Satellite Scintillation with Zenith Angle." **J. Atmos. Terr. Phys.** 25 : 334-365.
- CRL 2000. **Lecture for Post-PARTNER Training.**
- Dabas, R. S. et. al. 1991. "Gigahertz Scintillation Observations at 22.0° N Magnetic Latitude in the Indian Zone." **Radio Science.** 26(3):759-771.
- Fang, D.J. and Liu, C.H. 1984. "Statistical Characterizations of Equatorial Scintillation in the Asian Region." **Radio Science.** 19(1) : 345-358.
- Feher, K. 1987. **Telecommunications Measurements, Analysis, and Instrumentation.** New Jersey: Prentice Hall.
- Filip, M. and Vilar, E. 1990. "Optimum Utilization of the Channel Capacity of a

- Satellite Link in the Presence of Amplitude Scintillations and Rain Attenuation." **IEEE Trans. on Commun.** 38(11).
- Flock, W.J. editor. 1983. Propagation Effects on Satellite Systems at Frequencies below 10GHz. A Handbook for Satellite System Design. Nasa Reference Publication 1108. December.
- Glisic, S. and Vucetic, B. 1997. **Spread Spectrum CDMA Systems for Wireless Communications.** Artech House, Inc.
- Hocutt, A.M. 1988. Predicting Ionospheric Scintillation for Satellite Communications. **IEEE AES Magazine in NAECON.** USA. 88: 11-13.
- Igarashi, K. et. al. 2000. "Pacific Region Equatorial Anomaly Studies in Asia." (PREASA): Part1 Introduction and Overview of the Program, **Adv. Space Res.** V26(8) : 1241-1250.
- Johnson, N.L. 1949. "Systems of Frequency Curves generated by Method of Translation." **Biometrika.** 36 : 149-176.
- Lawrence, R.S. et. al. 1964. "A Survey of Ionospheric Effects Upon Earth-Space Radio Propagation." **Proceedings of the IEEE.** : 4-27.
- Liu, C.H. and Franke, S. J. 1986. "Experimental and Theoretical Studies of Ionospheric Irregularities Using Scintillation Techniques." **Radio Science.** 21(3): 363-374.
- Livingston, R.C. et. al. 1980. "Multiscale Observations of Irregularities in an Isolated and Decaying Plasma Bubble." **Proc. VI ISEA.**
- Mangir, T.E. "The Future of Public Satellite Communications" : 395-410.
- Mikkelsen, I.S. et. al. 1978. "Geometrical considerations of 136 MHz Amplitude Scintillation in the Auroral Oval." **J. Atmos. Terr. Phys.** 40 : 479-483.
- Mollen, T.A. et.al. 1988. "A Study of C band Equatorial Scintillation in the Asian Sector." **Radio Science.** 23(3) : 337-345.
- Moulsley, T.J. and Vilar, E. 1982. "Experimental and Theoretical Statistics of Microwave Amplitude Scintillations on Satellite Down-Links." **IEEE Trans. Antennas Propagat.** Ap-30(6) : 1099-1106.
- Papoulis, A. 1991. **Probability Random Variables, and Stochastic Processes** 3rd Ed. Singapore: McGraw-Hill, Inc.
- Proakis, J. G. and Salchi, M. 1997. **Contemporary Communication System Using MATLAB.** USA. PWS Publishing Company.

- Proakis, J.G. 2001 **Digital Communications**. 4th Ed. Singapore : McGrawHill, Inc.
- Recommendation ITU-R P.531-4 1997. "Ionospheric Propagation Data and Prediction Methods Required for the Design of Satellite Services and Systems."
- Recommendations ITU-R PN. 1057 1994. "Probability Distributions Relevant to Radiowave Propagation Modeling."
- Rino, C.L. and Owen, J. 1981. "On the Temporal Coherence Loss of Strongly Scintillating Signal." **Radio Science**. 16 : 31-33.
- Singleton, D.G. 1974. "Power Spectra of Ionospheric scintillations." **J. Atmos. Terr. Phys.** 36 : 113-133.
- Sklar, B. 1988. **Digital Communications Fundamentals and Applications** . New York : Prentice. Hall, Inc.
- Vilar, E et. al. 1985. "Measurement and Modeling of Amplitude and Phase Scintillations in an earth-Space path" **Journal of the Institution of Electronic and Radio Engineers**. 55(3) : 87-96.
- Whitney, H. E. and Basu, S. 1977. "The Effect of Ionospheric Scintillation on VHF/UHF Satellite Communication." **Radio Science**. 12(1) : 123-133.
- Yeh, K.C. and Liu, C.H. 1982. "Radio Wave Scintillations in Ionosphere." **Proceeding of the IEEE**. 70(4) : 324-360.



This material is reserved for educational use only, not allowed for commercial use.

Forbidden to modify the content, and cite the document when use.

APPENDIX A

The equatorial electrodynamics contributes to the information of the unstable ionosphere that forms the ionized content to the irregularities covering a large range of scale sizes. These irregularities cause the signal deterioration to the Telecommunication system. For instances, the large-scale irregularities cause spread-F condition that decreases the HF signal level; and the small-scale irregularities cause signal scintillation. Two outstanding equatorial ionospheric regions that cause the irregularities are the equatorial F region and E region. The features of F region are (a) the equatorial anomaly in daytime and (b) the intense electron density distribution in the irregularities at nighttime. The E region irregularities play an active interchange role with the F region irregularities processes; such as sporadic E, auroral E and equatorial electrojet.

The interaction vector between the ionospheric charged particle movement and the geomagnetic field leads to the electric field described by

$$\vec{E} = \vec{v} \times \vec{B} \quad (\text{A.1})$$

where \vec{E} : the electric field intensity \vec{v} : the drift velocity of the charge particle
 \vec{B} : the geomagnetic field

The electric field in turn drives two current loops in daytime, the northern and southern hemisphere. The currents flow counterclockwise in the northern hemisphere; and clockwise in the southern one. Therefore the currents of both loops flow eastward near the geomagnetic equator (Flock. 1983). These strong and dense currents are known as the equatorial electrojet flowing at the height about 110 km. in the E region of the equatorial ionosphere. The current flows are described by Fig. A.1.

During the maximum solar cycle year, the F region experiences the abnormal increasing in height at the postsunset. This is mainly caused by the enhancement of the eastward electric field. The electric field is eastward during daytime; and reverse to westward after sunset. Since the electric field is perpendicular to the geomagnetic field, then the drift $\vec{E} \times \vec{B} / B^2$ moves the ionized particles upward vertically during the daytime; and downward at nighttime depending on the direction of electric field. This

This material is reserved for educational use only, not allowed for commercial use.

Forbidden to modify the content, and cite the document when use.

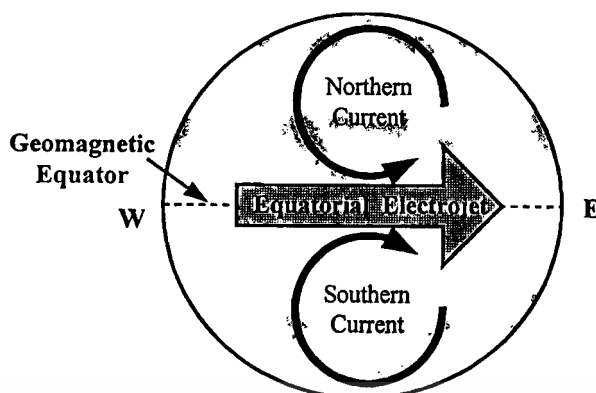


Fig. A.1 The pattern of electric currents movement

upward motion is termed as the equatorial fountain. The ionized particles rise above the geomagnetic equator until reaching the height that the lifting force and the gravity force are balanced. Then the charged particles tend to move along the magnetic field line; and are deposited at the higher tropical latitude, about $\pm 15^\circ$ latitude of geomagnetic equator. This is called the equatorial anomaly (Igarashi *et.al.* 2000) as presented by Fig. A.2 (Ondoh and Marubashi. 2000 : 92).

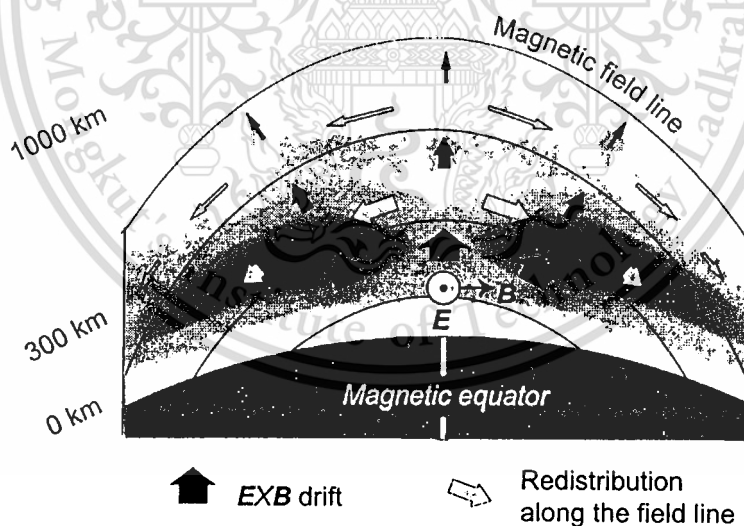


Fig. A.2 Ionized particles flow forming the equatorial anomaly in daytime

At the postsunset time, the electric field intensity increases before it reverses to the west. This prereversal enhancement of the eastward electric field raises the F layer at the geomagnetic equator to the high altitudes, where recombination effects are negligible; and the generation of the irregularities may be obtained. The increasing electric field causes an outflow of the ionization from the trough region and

This material is reserved for educational use only, not allowed for commercial use.

Forbidden to modify the content, and cite the document when use.

combining with the neutral wind at the higher altitudes. Consequently, the ionized particles counterbalance the normal decay of the ionization process; and then increase the ionization density. This results a secondary peak in the ionization in daytime (at postsunset time). Furthermore, the effect of the prereversal enhancement depends on the seasonal variation and solar activity (Anderson and Klobuchar. 1983). After that, the electric field reverses to westward causing the vertical charged particles drift turns downward. This downward $\vec{E} \times \vec{B}$ drift can also produce the nighttime enhancement of the electron density at the geomagnetic equator. Consequently, the enhancement of the electron density can occur according to both prereversal and postreversal processes.



APPENDIX B

The radius of the Fresnel zone can be obtained as shown in Fig. B.1. There are two propagation paths; direct path, TPR , and indirect path, TSR . TPR is from the transmitter T to the receiver R; and path TSR has the distance $TPR + \lambda/2$ if the wavelengths λ of both signals are the same. The region within the radius F_1 at the distance d_T and d_R is defined as the first Fresnel zone.

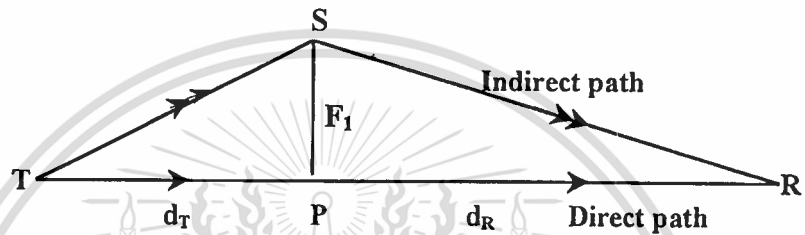


Fig. B.1 Geometry for consideration of Fresnel zone

If the first Fresnel radius $F_1 \ll d_T$ and also $F_1 \ll d_R$, Flock(1983) described that

$$TS = \sqrt{d_T^2 + F_1^2} = d_T \left[1 + \frac{F_1^2}{2d_T^2} \right] \quad (\text{B.1})$$

and

$$SR = \sqrt{d_R^2 + F_1^2} = d_R \left[1 + \frac{F_1^2}{2d_R^2} \right] \quad (\text{B.2})$$

from $TSR = TPR + \lambda/2$ then

$$d_T + d_R + \frac{F_1^2}{2d_T} + \frac{F_1^2}{2d_R} = d_T + d_R + \frac{\lambda}{2} \quad (\text{B.3})$$

$$\therefore F_1 = \sqrt{\frac{\lambda d_T d_R}{d}} \quad (\text{B.4})$$

where $d = d_T + d_R$ for the first Fresnel zone

For higher orders of the Fresnel zone ($n = 2, 3, 4, \text{etc}$), $TSR = TPR + n\lambda/2$, the radius F_n is given by

$$F_n = \sqrt{n} \cdot F_1 \quad (\text{B.5})$$

All the radiating components passing through the first Fresnel zone have the field intensity that add constructively. Radiation passing through the second Fresnel zone (between F_1 and F_2) interferes destructively with the radiating components that passing through the first zone. In contrast, the radiation passing through the third zone adds with the one passing through the first zone. This odd-even destructive and constructive interference continues alternately. The radiation from each zone (n) is 180° out of phase comparing with that from the adjacent zones ($n-1$ and $n+1$); however the amplitudes of the contribution decrease with increasing n .

APPENDIX C

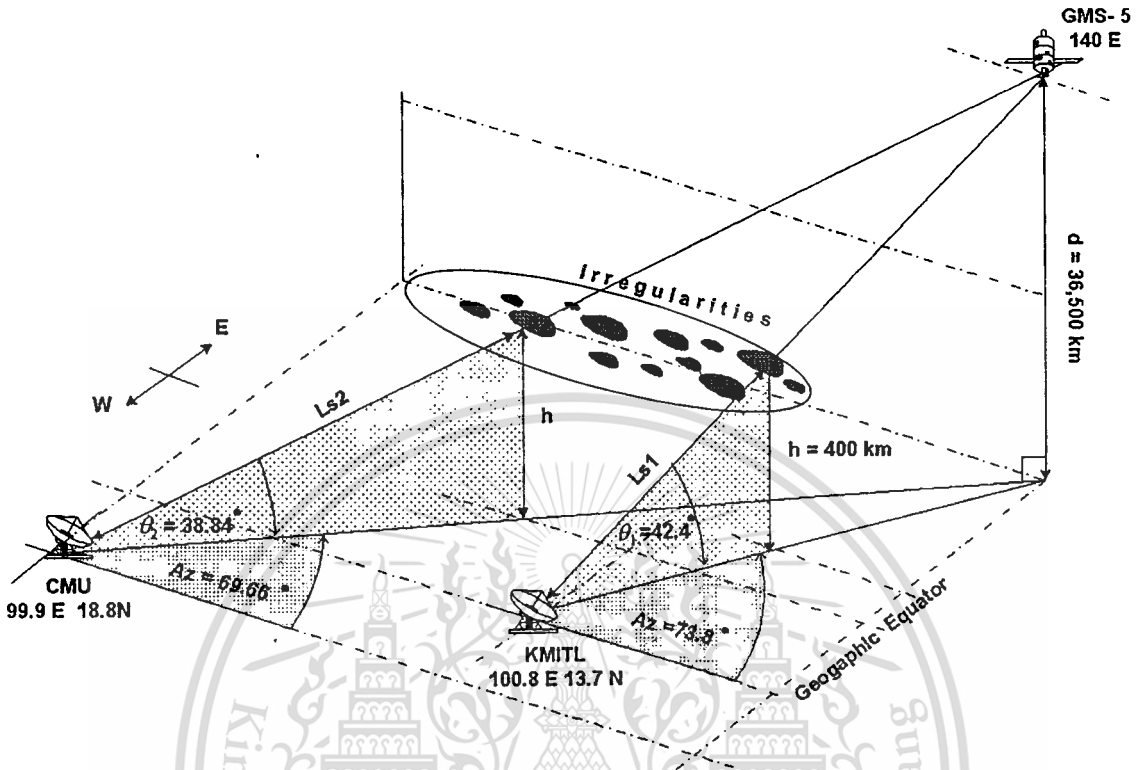


Fig. C.1 Schematic presentation of Earth-space paths between 2 stations (GMS-5 to KMITL and GMS-5 to CMU)

The slant-path length (L_S), below the irregularities mediums, can be computed for the elevation angle (θ) higher than 5° as:

$$L_S = \frac{(h_R - h_S)}{\sin \theta} \quad \text{C.1}$$

APPENDIX D

The correlation receiver of binary detection can be configured as a single matched filter or product integrator as shown in Fig. D.1 (a) with the reference signal being the difference between the binary prototype signals, $s_1(t) - s_2(t)$. The output of the correlator, $z(t)$, is fed directly to the decision stage. For binary detection, the correlation receiver can also be shown as in Fig. D.1 (b), as two matched filters or product integrators; each of which is matched to one of the prototype reference signals, $s_1(t)$ or $s_2(t)$. The correlator outputs, $z_i(T)$ ($i = 1, 2$) can be difference to form

$$z(T) = z_1(T) - z_2(T) \quad \text{D.1}$$

$z(T)$, called the *test statistics*, is fed to the decision stage, as in the case of the single correlator. In the absence of noise, an input waveform, $s_i(t)$, yields the output, $z(T) = a_i(T)$, a signal only component. The input noise, $n(t)$ is a Gaussian random process. Since the correlator is a linear device, the output noise is also a Gaussian random process. Thus the output of the correlator sampled at $t = T$, yields

$$z(T) = a_i(T) + n_o(T) \quad i = 1, 2 \quad \text{D.2}$$

where $n_o(T)$ is the noise component. To shorten the notation we sometimes express $z(T)$ as $a_i + n_o$. The noise component, n_o , is a zero-mean Gaussian random variable, and thus $z(T)$ is a Gaussian random variable with a mean of either a_1 or a_2 depending on whether a binary one or binary zero was sent. The probability density function of Gaussian random noise can be expressed as

$$p(n_o) = \frac{1}{\sigma_o \sqrt{2\pi}} \exp \left[-\frac{1}{2} \left(\frac{n_o}{\sigma_o} \right)^2 \right] \quad \text{D.3}$$

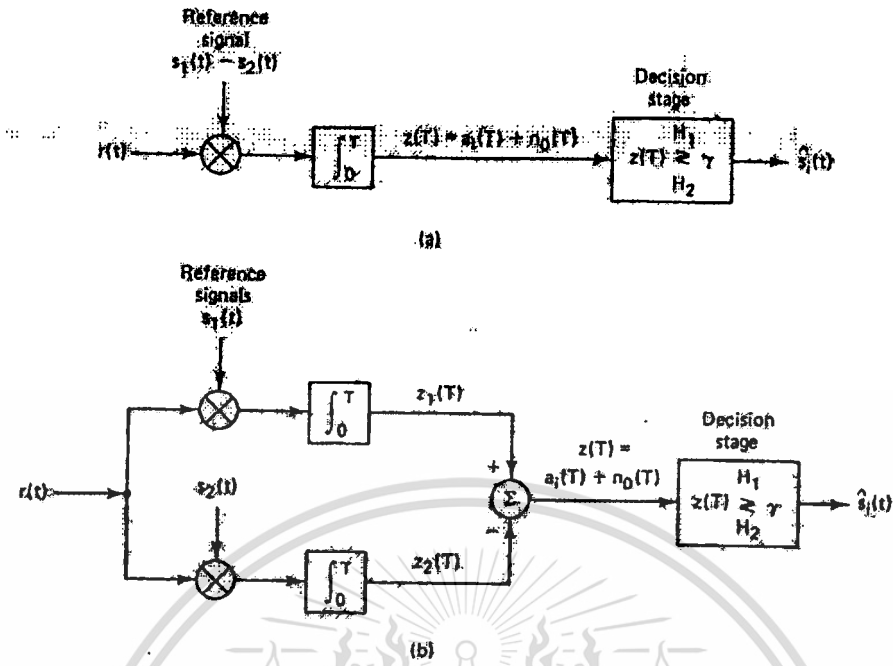


Fig. D.1 Binary correlator receiver (a) Using a single correlator (b) Using two correlators

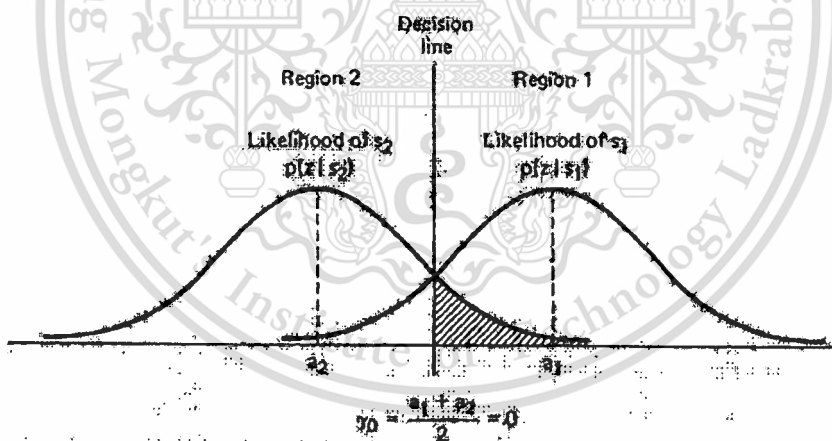


Fig. D.2 Conditional probability density functions: $p(z|s_1), p(z|s_2)$

where σ_o^2 is noise variance. Thus it follows from Equations (D.2) and (D.3) that the conditional probability density functions $p(z/s_1)$ and $p(z/s_2)$ can be expressed as

$$p(z/s_1) = \frac{1}{\sigma_o \sqrt{2\pi}} \exp \left[-\frac{1}{2} \left(\frac{z - a_1}{\sigma_o} \right)^2 \right] \tag{D.4}$$

$$p(z/s_2) = \frac{1}{\sigma_o \sqrt{2\pi}} \exp \left[-\frac{1}{2} \left(\frac{z - a_2}{\sigma_o} \right)^2 \right] \quad (D.5)$$

These conditional PDF are illustrated in Fig. D.2. The rightmost conditional PDF $p(z/s_1)$, illustrates the probability density of the detector output, $z(T)$, given that $s_1(t)$ was transmitted. Similarly, the leftmost conditional PDF, $p(z/s_2)$, illustrates the probability density of $z(T)$ given that $s_2(t)$ was transmitted. The abscissa, $z(T)$ represents the full range of possible sample output value.

The second step of the signal detection process consists of comparing the test statistic, $z(T)$ to the optimum threshold level, γ_0 , in order to estimate which signal, $s_1(t)$ or $s_2(t)$, has been transmitted. With regard to optimizing the binary decision threshold for deciding in which region a received signal is located, the minimum error criterion for equally likely binary signals corrupted by Gaussian noise can be stated as follows:

$$\begin{array}{cc} H_1 & H_2 \\ z(T) > \gamma_0, & z(T) < \gamma_0 \end{array} \quad (D.6)$$

where H_1 and H_2 are the two possible (binary) hypotheses. Choosing H_1 is equivalent to deciding that signal $s_1(t)$ was sent, and choosing H_2 is equivalent to deciding that signal $s_2(t)$ was sent. The inequality relationship indicates that hypothesis H_1 is chosen if $z(T) > \gamma_0$, and hypothesis H_2 is chosen if $z(T) < \gamma_0$. If $z(T) = \gamma_0$, the decision can be an arbitrary one. For equal-energy, equally likely antipodal signals, where $s_1(t) = -s_2(t)$ and $\gamma_0 = 0$. The optimum decision rule becomes

$$\begin{array}{cc} H_1 & H_2 \\ z(T) > \gamma_0 = 0, & z(T) < \gamma_0 = 0 \end{array} \quad (D.7)$$

or

$$\begin{array}{ll} \text{decide } s_1(t) & \text{if } z_1(T) > z_2(T) \\ \text{decide } s_2(t) & \text{otherwise} \end{array} \quad (D.8)$$

APPENDIX E

The important performance-measurement used for comparing digital modulation scheme is the probability of error, P_E . The calculation for obtaining P_E can be presented geometrically as show in Fig. E.1. From the figure, s_1 is the transmitted signal vector; and n is the noise vector. The probability of the detector making an incorrect decision is termed as the probability of symbol error (P_E). It is convenient to specify system performance by the probability of bit error (P_B).

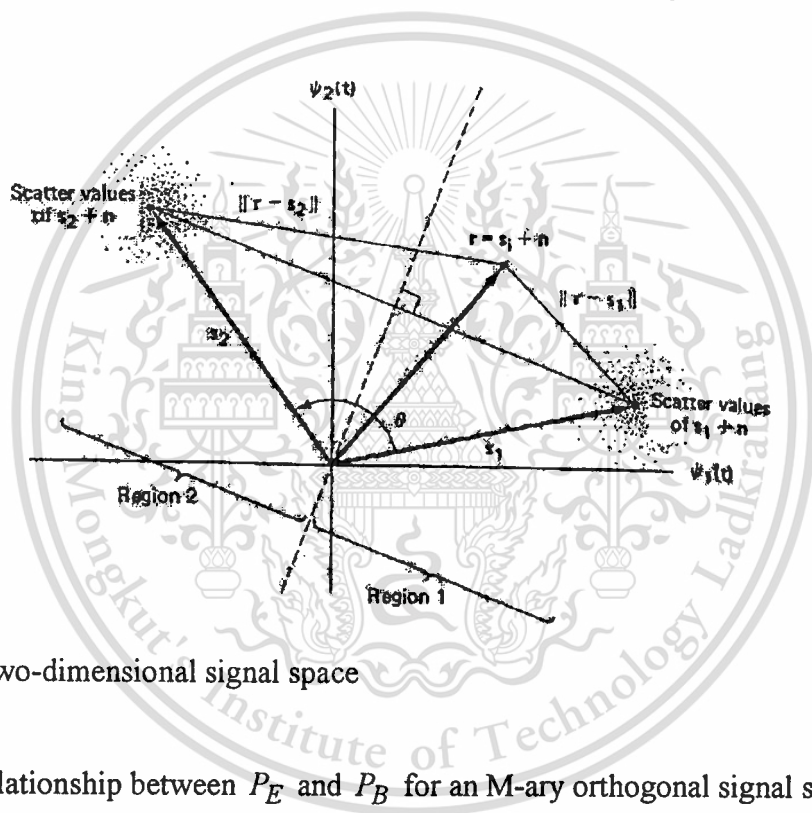


Fig. E.1 Two-dimensional signal space

The relationship between P_E and P_B for an M -ary orthogonal signal set is

$$\frac{P_B}{P_E} = \frac{2^{k-1}}{2^k - 1} = \frac{M/2}{M-1} \quad (\text{E.1})$$

and for multiple phase signaling (M-PSK) is

$$P_B \approx \frac{P_E}{\log_2 M} = \frac{P_E}{k} \quad (\text{for } P_E \ll 1) \quad (\text{E.2})$$

for coherent detection of BPSK modulation, $P_E = P_B$.

Assume that the signals are equally likely; also assume that when signal $s_i(t)$ ($i = 1, 2$) is transmitted, the receiver signal, $r(t)$, is equal to $s_i(t) + n(t)$, where $n(t)$ is an AWGN process. The antipodal signals, $s_1(t)$ and $s_2(t)$, can be characterized in a one-dimensional signal space as described in Fig. E.1. Where

$$\begin{aligned} s_1(t) &= \sqrt{E}\Psi_1(t) \\ &0 \leq t \leq T \\ s_2(t) &= -\sqrt{E}\Psi_1(t) \end{aligned} \quad (\text{E.3})$$

where E is the signal energy per symbol; and T is the symbol duration; and

$$\Psi_1(t) = \sqrt{\frac{2}{T}} \cos \omega_o(t) \quad (\text{E.4})$$

The decision stage of the detector will choose the $s_i(t)$ with the largest correlator output $Z_i(T)$ (Appendix D). Then the detector decides

$$\begin{aligned} &s_1(t) \quad \text{if } z(T) > \gamma_0 = 0 \\ &s_1(t) \quad \text{otherwise} \end{aligned} \quad (\text{E.5})$$

Two types of error can be made, as shown in Fig. D.2. The first type of error takes place if signal $s_1(t)$ is transmitted but the noise is such that the detector measures a negative value for $Z(T)$ and chooses hypothesis H_2 (the hypothesis that signal $s_2(t)$ was sent). The second type of error takes place if signal $s_2(t)$ is transmitted but the detector measures a positive value for $Z(T)$ and chooses hypothesis H_1 (the hypothesis that signal $s_1(t)$ was sent). To calculate the probability of bit error, P_B , for this binary minimum error detector, the following relationship can be obtained.

$$P_B = P(H_2 | s_1)P(s_1) + P(H_1 | s_2)P(s_2) \quad (\text{E.6})$$

if $P(s_1) = P(s_2) = \frac{1}{2}$, then

$$P_B = \frac{1}{2}P(H_2 | s_1) + \frac{1}{2}P(H_1 | s_2) \quad (\text{E.7})$$

Because of the symmetry of the PDF in Fig. D.2, Equation E.7 can be related as:

$$P_B = P(H_2 | s_1) = P(H_1 | s_2) \quad (\text{E.8})$$

The probability of bit error, P_B , is numerically equal to the area under the “tail” of either PDF, $p(z | s_1)$ or $p(z | s_2)$, that falls on the incorrect side of the threshold. Therefore P_B can be computed by integrating $p(z | s_1)$ between the limits $-\infty$ and γ_0 , or by integrating $p(z | s_2)$ between the limits γ_0 and ∞ .

$$P_B = \int_{\gamma_0=(a_1+a_2)/2}^{\infty} p(z | s_2) dz \quad (\text{E.9})$$

where the likelihoods, $p(z | s_i)$ ($i = 1, 2$), are Gaussian functions with mean value, a_i , and the optimum threshold, γ_0 is equal to $(a_1 + a_2)/2$. The area-related P_B is shown by the shaded area in Fig. D.2. Then P_B can be obtained as:

$$P_B = \int_{(a_1+a_2)/2}^{\infty} \frac{1}{\sigma_0 \sqrt{2\pi}} \exp \left[-\frac{1}{2} \left(\frac{z - a_2}{\sigma_0} \right)^2 \right] dz \quad (\text{E.10})$$

Let $u = \frac{z - a_2}{\sigma_0}$. Then $\sigma_0 du = dz$, and

$$P_B = \int_{u=(a_1-a_2)/2\sigma_0}^{u=\infty} \frac{1}{\sqrt{2\pi}} \exp \left[-\frac{u^2}{2} \right] du = Q \left(\frac{a_1 - a_2}{2\sigma_0} \right) \quad (\text{E.11})$$

where σ_0 is the standard deviation of the noise out of the correlator. $Q(x)$, called the *complementary error function* or *co-error function*, is defined as:

$$Q(X) = \frac{1}{\sqrt{2\pi}} \int_x^{\infty} \exp\left(-\frac{u^2}{2}\right) du \quad (\text{E.12})$$

For equal-energy antipodal signaling such as BPSK format, the receiver output signal components are $a_1 = \sqrt{E_b}$ when $s_1(t)$ is sent; and $a_2 = -\sqrt{E_b}$ when $s_2(t)$ is sent, where E_b is the signal energy per binary symbol. For AWGN process, the response of correlators to white noise is

$$\sigma_j^2 = \frac{N_0}{2} \quad j = 1, \dots, N \quad (\text{E.13})$$

where N_0 is the two-sided power spectral density of AWGN process. Therefore P_B for coherent detection of PSK can be rewritten as follows:

$$P_B = \int_{\sqrt{2E_b/N_0}}^{\infty} \frac{1}{\sqrt{2\pi}} \exp\left[-\frac{u^2}{2}\right] du = Q\left(\sqrt{\frac{2E_b}{N_0}}\right) \quad (\text{E.14})$$

APPENDIX F

When comparing the error performance of noncoherent FSK with coherent FSK, it can be seen that at the same P_B , noncoherent FSK requires E_b/N_0 about 1 dB more than that for coherent FSK (for $P_B \leq 10^{-4}$). The noncoherent receiver is easier to implement since coherent reference signal generating is unnecessary. Therefore almost all FSK receivers use noncoherent detection.

The analytical expression for binary FSK signal set, $\{s_1(t)\}$, can be defined as follows:

$$s_i(t) = \sqrt{\frac{2E}{T}} \cos(\omega_i t + \phi) \quad 0 \leq t \leq T, \quad i = 1, 2 \quad (\text{F.1})$$

The detector is characterized by $M = 2$ channels of bandpass filters and envelope detectors as shown in Fig. F.1. The input to the detector consists of the received signal, $r(t) = s_i(t) + n(t)$, where $n(t)$ is the AWGN process with two-sided PSD, $N_0/2$. The probability of error can be computed as:

$$\begin{aligned} P_B &= \frac{1}{2}P(H_2 | s_1) + \frac{1}{2}P(H_1 | s_2) \\ &= \frac{1}{2} \int_0^T p(z | s_1) dz + \frac{1}{2} \int_0^T p(z | s_2) dz \end{aligned} \quad (\text{F.2})$$

For the binary case, the *test statistic* $z(T)$ can be defined by $z_1(T) - z_2(T)$. Assume that the bandwidth of the filter, W_f , is $1/T$, so that the envelope of the FSK signal is approximately preserved at the filter output. If there was no noise at the receiver, the value of $z(T) = \sqrt{2E/T}$ when $s_1(t)$ is sent; and $z(T) = -\sqrt{2E/T}$ when $s_2(t)$ is sent. Because of the symmetry, the optimum threshold is $\gamma_0 = 0$. The PDF $p(z | s_1)$ is similar to $p(z | s_1)$; that is

$$p(z | s_1) = p(-z | s_2) \quad (\text{F.3})$$

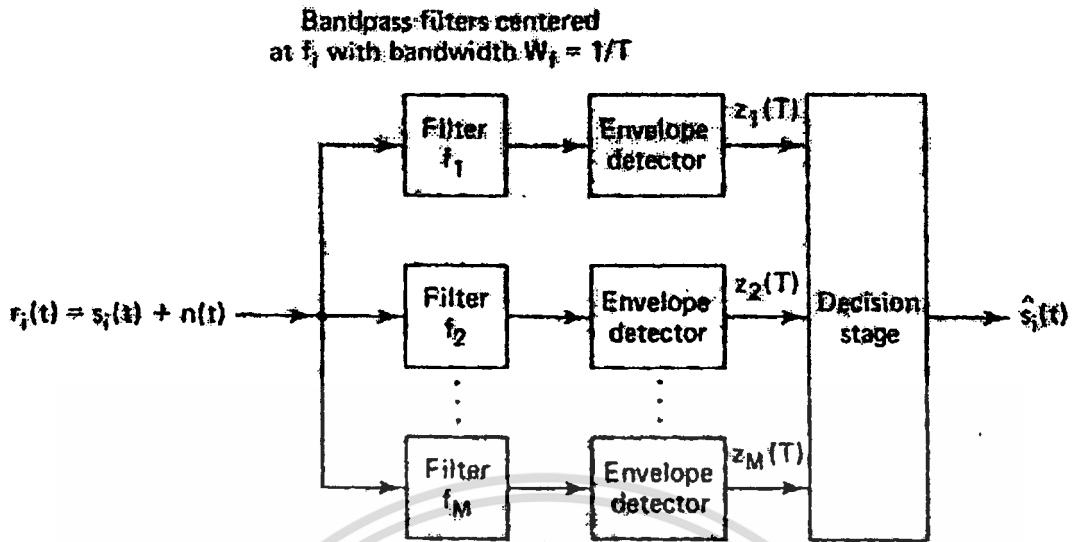


Fig F.1 Noncoherent detection of FSK using envelope detectors

therefore,

$$P_B = \int_0^T p(z | s_2) dz \quad (\text{F.4})$$

or

$$P_B = P(z_1 > z_2 | s_2) \quad (\text{F.5})$$

where z_1 and z_2 denote the outputs $z_1(T)$ and $z_2(T)$ from the envelope detectors as shown in Fig. D.2. For the case where the tone $s_2(t) = \cos \omega_2(t)$ is sent, such that $r(t) = s_2(t) + n(t)$. The output $z_1(T)$ is a Gaussian noise random variable only; it has no signal component. A Gaussian distribution into the nonlinear envelope detector yields a Rayleigh distribution at the output, so that

$$p(z_1 | s_2) = \begin{cases} \frac{z_1}{\sigma_0^2} \exp\left(-\frac{z_1^2}{2\sigma_0^2}\right) & z_1 \geq 0 \\ 0 & z_1 < 0 \end{cases} \quad (\text{F.6})$$

where σ_0^2 is the noise at the filter output. On the contrary, $z_2(T)$ has a Rician distribution, since the input to the lower envelope detector is a sinusoid plus noise. The PDF, $p(z_2 | s_2)$ can be written as:

$$p(z_2 | s_2) = \begin{cases} \frac{z_2}{\sigma_0^2} \exp\left(-\frac{(z_2^2 + A^2)}{2\sigma_0^2}\right) I_0\left(\frac{z_2 A}{\sigma_0^2}\right) & z_2 \geq 0 \\ 0 & z_2 < 0 \end{cases} \quad (\text{F.7})$$

where $A = \sqrt{2E/T}$; and the function $I_0(x)$ known as the modified zero-order Bessel function of the first kind can be defined as:

$$I_0(x) = \frac{1}{2\pi} \int_0^{2\pi} \exp(x \cos \theta) d\theta \quad (\text{F.8})$$

when $s_2(t)$ is transmitted, the receiver makes the error whenever the envelope sample $z_1(t)$ obtained from the upper channel due to noise alone exceeds the envelope sample $z_2(t)$ obtained from the lower channel due to signal plus noise. Thus the probability of this error can be obtained by integrating $p(z_1 | s_2)$ with respect to z_1 from z_2 to infinity; then averaging all possible values of z_2 . That is:

$$\begin{aligned} P_B &= P(z_1 > z_2 | s_2) \\ &= \int_0^\infty p(z_2 | s_2) \left[\int_{z_2}^\infty p(z_1 | s_2) dz_1 \right] dz_2 \\ &= \int_0^\infty \frac{z_2}{\sigma_0^2} \exp\left[-\frac{(z_2^2 + A^2)}{2\sigma_0^2}\right] I_0\left(\frac{z_2 A}{\sigma_0^2}\right) \left[\int_{z_2}^\infty \frac{z_1}{\sigma_0^2} \exp\left(-\frac{z_1^2}{\sigma_0^2}\right) dz_1 \right] dz_2 \end{aligned} \quad (\text{F.9})$$

The inner integral is the conditional probability of an error for a fixed value of z_2 , given that $s_2(t)$ was sent; and the outer integral averages this conditional probability over all possible values of z_2 . This integral can be evaluated to yield

$$P_B = \frac{1}{2} \exp\left(-\frac{A^2}{4\sigma_0^2}\right) \quad (\text{F.10})$$

and $\sigma_0^2 = 2(N_0/2)W_f \quad (\text{F.11})$

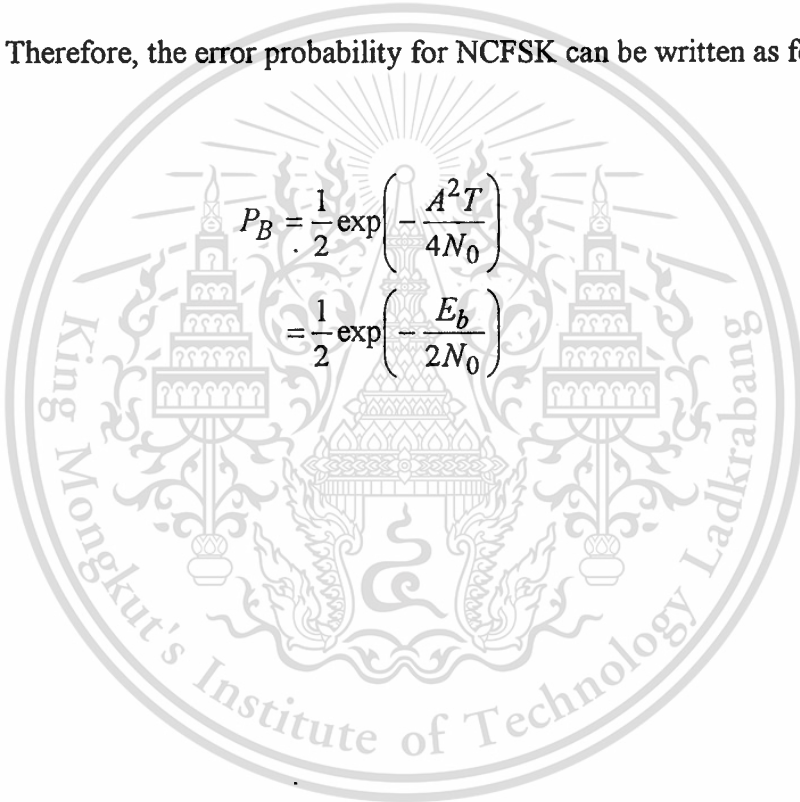
This material is reserved for educational use only, not allowed for commercial use.

Forbidden to modify the content, and cite the document when use.

Thus Equation (F.10) becomes

$$P_B = \frac{1}{2} \exp\left(-\frac{A^2}{4N_0W_f}\right) \quad (\text{F.12})$$

This equation indicates that the error performance depends on the bandpass filter bandwidth. P_B becomes smaller as W_f is decreased. This is valid only when the intersymbol interference (ISI) is negligible. For the minimum W_f allowed, $W_f = R$ bits/s = $\frac{1}{T}$. Therefore, the error probability for NCFSK can be written as follow:



The watermark is a circular emblem for King Mongkut's Institute of Technology Ladkrabang. It features a central sunburst with rays emanating from a central point. Below the sunburst are two traditional Thai stupas (chedis) on either side of a central, more ornate structure. The entire emblem is surrounded by a decorative border. The text 'King Mongkut's Institute of Technology Ladkrabang' is written in a circular path around the emblem.

$$P_B = \frac{1}{2} \exp\left(-\frac{A^2T}{4N_0}\right) \quad (\text{F.13})$$

$$= \frac{1}{2} \exp\left(-\frac{E_b}{2N_0}\right)$$

AUTHOR BIOGRAPHY

Author : Miss Khajitpan Makaratat

Date of Birth : July 22, 1977

Bachelor Degree : B.Eng. in Telecommunication Engineering

Institution : Department of Telecommunication Engineering

Faculty of Engineering

King Mongkut's Institute of Technology Ladkrabang

Year of Graduation : 1998

Interested Researches :

Radio wave propagation, Ionospheric scintillation

Irregularities characteristics

Related Publication:

1. K. Makaratat, , A. Decharat, N. Hemmakorn, K. Igarashi and H. Minakoshi,
 "Characteristics of S-band scintillation associated with maximum solar cycle,"
*Proceeding of the Third International Symposium on Wireless Personal
 Multimedia Communications*, Bangkok, Thailand, vol. 1, Nov. 2000, pp. 558-
 563.
2. K. Makaratat, A. Decharat, N. Hemmakorn, K. Igarashi and H. Minakoshi,
 "Statistical analysis of S-band ionospheric scintillation at Bangkok,"
*Proceedings of the 2000 Asia-Pacific Symposium on Broadcasting and
 Communications*, Bangkok, Thailand, Dec. 2000, pp.207-212.